

GEOSPATIAL ANALYSIS AND SEASONAL CHANGES IN WATER-EQUIVALENT  
HYDROGEN IN EASTERN EQUATORIAL MARS

A Dissertation

Presented in Partial Fulfillment of the Requirements for the

Degree of Doctor of Philosophy

with a

Major in Geology

in the

College of Graduate Studies

University of Idaho

by

June Renee Clevy

December 2014

Major Professor: Simon A. Kattenhorn, Ph.D.

### Authorization to Submit Dissertation

This dissertation of June Renee Clevy, submitted for the degree of Doctor of Philosophy with a major in Geology and titled “GEOSPATIAL ANALYSIS AND SEASONAL CHANGES IN WATER-EQUIVALENT HYDROGEN IN EASTERN EQUATORIAL MARS,” has been reviewed in final form. Permission, as indicated by the signatures and dates given below, is now granted to submit final copies to the College of Graduate Studies for approval.

Major Professor \_\_\_\_\_ Date \_\_\_\_\_  
Simon A. Kattenhorn, PhD.

Committee Members \_\_\_\_\_ Date \_\_\_\_\_  
Mickey E. Gunter, PhD.

\_\_\_\_\_ Date \_\_\_\_\_  
Jerry P. Fairley, PhD.

\_\_\_\_\_ Date \_\_\_\_\_  
Kenneth F. Sprenke , PhD.

\_\_\_\_\_ Date \_\_\_\_\_  
Karen S. Humes, PhD.

Department Administrator \_\_\_\_\_ Date \_\_\_\_\_  
Mickey E. Gunter, PhD.

Discipline’s College Dean \_\_\_\_\_ Date \_\_\_\_\_  
Paul Joyce, PhD.

Final Approval and Acceptance by the College of Graduate Studies

\_\_\_\_\_ Date \_\_\_\_\_  
Jie Chen, PhD.

## Abstract

This dissertation describes the relationship between hydrogen abundance, as measured through epithermal neutron counts, and the topographic, geologic, and surficial features in the equatorial region of eastern Mars. In Chapter 1, I present an alternative method for resampling the epithermal neutron count data collected by the neutron spectrometer from Mars Odyssey's Gamma Ray Spectrometer suite. Chapter 2 provides a seasonal break down of mean and median epithermal neutron count rates and examines areas of static, seasonal, and episodic hydrogen enrichment. Armed with new maps of mean epithermal neutron count rates and derivative maps of weight percent water equivalent hydrogen, I examine the spatial relationships between equatorial hydrogen concentrations and satellite-measured surface properties such as elevation, its derivatives slope and aspect, albedo, dust cover, geologic units, and valley networks in Chapter 3.

The chapters in this dissertation represent a workflow from the development of the Water Equivalent Hydrogen dataset used in this research (Chapter 1), to an analysis of seasonal changes in the hydrogen signal (Chapter 2), and the relationships between this data and measurements of elevation, crustal thickness, surface composition, and geomorphology (Chapter 3). These investigations were made possible by the application of terrestrial geographic information science to planetary geology through Geographic Information Systems (GIS). Neighborhood processing allowed me to refine the spatial resolution of the epithermal neutron count in the first chapter. Class frequency tables permitted the identification of changes over time in chapter two and facilitated the identification of high and low variability areas. Finally, a quantitative process known as the Location Quotient, which builds upon frequency tables, was applied to identify more frequent than expected combinations of hydrogen abundance and other martian data (e.g., elevation) for the purpose of identifying relationships and defining their spatial extent.

## Acknowledgements

For help above and beyond the call of duty, I would like to thank the following wonderful souls:

Simon Kattenhorn, whose wit and support has kept me sane and motivated all these years.

Bill Feldman, Rick Elphic, and Tom Prettyman, all originally on Los Alamos' Water on Mars team, for introducing me to the neutron spectrometer data and assisting me whenever I asked.

Steven Jaret, for having the moxie to introduce himself as a high school student and suggest we work on an abstract. Great friendships come from chance encounters.

Julie Groenleer, Christina Coulter, and Alex Patthoff – and 2 dozen other lab siblings – thank you for being there for me with laughter, encouragement, and solid advice.

Amanda Nahm, academic cousin and post-doc goddess, thank you for your support in matters on and off campus.

## **Dedication**

To my parents, Leona McDowell and Gordon Clevy; my great-aunt and uncle, Marie and Charlie Clevy; and all of those who helped by simply being themselves.

## Table of Contents

Authorization to Submit Dissertation.....	ii
Abstract.....	iii
Acknowledgements.....	iv
Dedication.....	v
Table of Contents.....	vi
List of Figures.....	x
List of Tables.....	xiii
Chapter 1: Resampling Mars Odyssey data to improve hydrogen concentration resolution: balancing spatial and statistical robustness.....	1
Abstract.....	1
1. Introduction.....	2
2. Neutron Spectroscopy.....	3
2.1 Planetary Applications.....	3
2.2 Strengths and Limitations.....	5
2.3 Previous Spatial Methods.....	6
3. Geospatial Analysis.....	7
3.1 Window Sizes.....	9
3.2 Statistics.....	11
4. Evaluation of the Moving Window Technique.....	12
4.1 Visual Inspection.....	12

4.2 Contours of Equal Concentration.....	13
5. Discussion .....	15
5.1 Spatial Extent.....	15
5.2 Corrected Statistics.....	17
5.3 Smoothing, kernel approximation, and spacing .....	18
6. Conclusions .....	20
Chapter 1 Figures .....	21
Chapter 1 Tables.....	30
Chapter 1 References.....	31
Chapter 2: Seasonal investigation of water-equivalent hydrogen variability in the eastern equatorial region of Mars .....	35
Abstract.....	35
1. Introduction .....	35
1.1 Martian Seasons.....	35
1.2 Mars Odyssey Neutron Spectrometer .....	36
1.3 Statistical Confidence.....	37
1.4 Eastern Equatorial Mars.....	38
1.5 Seasonal Investigation .....	39
2. Terminology .....	40
3. Methods.....	41
3.1 Epithermal Neutron Records .....	41

3.2 Time Series.....	42
3.3 Neighborhood Point Statistics .....	43
3.4 Change Detection .....	44
3.5 Statistical Analysis .....	47
4. Results .....	47
4.1 Sample size .....	47
4.2 Change detection .....	48
4.3 Statistical Analysis .....	51
5. Discussion .....	53
5.1 Static Signal.....	53
5.2 Mars Orbital Mechanics.....	53
5.3 Locations of Interest.....	54
5.4 Seasonal Changes and Their Potential Causes.....	56
6. Conclusions .....	57
Chapter 2 Figures .....	59
Chapter 2 References.....	71
Chapter 3: Spatial associations between martian equatorial hydrogen distribution, elevation, geologic units, valley networks, and surface materials.....	73
Abstract.....	73
1. Introduction .....	74
2. Methods & Data .....	76



2.1 Combinatorial Or.....	77
2.2 Location quotient .....	78
2.3 Water Equivalent Hydrogen .....	80
2.4 Classes for Remaining Datasets .....	82
3. Spatial Analysis Results.....	84
3.1 Mean and Median Epithermal Neutron Counts.....	84
3.2 MOLA with WEH.....	84
3.3 Geologic Units with WEH .....	89
3.4 Dust with WEH .....	90
3.5 Albedo with WEH .....	91
3.6 MOLA Derivatives with WEH .....	91
3.7 Valley Networks .....	93
4. Discussion .....	95
4.1 Geomorphic Control .....	96
4.2 Geologic Interpretation.....	101
4.3 Surface materials.....	103
5. Conclusions .....	105
Chapter 3 Figures .....	107
Chapter 3 Tables.....	128
Chapter 3 References.....	130

## List of Figures

Ch. 1, Figure 1. Map of region of interest.....	21
Ch. 1, Figure 2. Comparison of binning and moving window results.....	22
Ch. 1, Figure 3. Scale comparison of sampling windows. ....	23
Ch. 1, Figure 4. Window radius controls the degree of smoothing.. ....	24
Ch. 1, Figure 5. Relationship between epithermal neutrons and hydrogen abundance.....	24
Ch. 1, Figure 6. Artifacts produced by square or undersized sampling windows.....	25
Ch. 1, Figure 7. Superimposed WEH isocons (a) for various circular window sizes.....	26
Ch. 1, Figure 8. Areas of maximum wt.% WEH form a semi-circle around Schiaparelli Basin.....	27
Ch. 1, Figure 9. Lines of equal WEH concentration.....	28
Ch. 1, Figure 10. Regional map with WEH isocons and sampling areas (red circles)...	29
Ch. 1, Figure 11. Alternative methods for establishing WEH distributions.....	29
Ch. 2, Figure 1. Plot of WEH and mean epithermal neutron count rates.....	59
Ch. 2, Figure 2. Graphical representation of Ch. 1, Table A.....	59
Ch. 2, Figure 3. Regional epithermal neutron count rates.....	60
Ch. 2, Figure 4. Relationship between temporal slices and martian months.....	61
Ch. 2, Figure 5. Change (a) and magnitude matrices (b).....	61
Ch. 2, Figure 6. Certainty with respect to number of points per node. ....	62
Ch. 2, Figure 7. Minimum and maximum differences between adjacent temporal slices. ....	62
Ch. 2, Figure 8. Cell frequency. ....	63
Ch. 2, Figure 9. Cell/pixel frequency displayed as magnitude.....	63
Ch. 2, Figure 10. The change matrix for the equinoxes (0° and 180° Ls).....	64
Ch. 2, Figure 11. Change matrices for the transitions between solstices and equinoxes.....	65
Ch. 2, Figure 12. Percent change between temporal slices.....	65

Ch. 2, Figure 13. Slice minimum and maximum values.....	66
Ch. 2, Figure 14. Cell standard deviation based on the 12 slices.....	67
Ch. 2, Figure 15. Static regions of WEH.....	68
Ch. 2, Figure 16. WEH maps of the full data extent for the equinoxes and solstices .....	69
Ch. 2, Figure 17. A closer view of the most variable portion of the region of interest.....	70
Ch. 3, Figure 1. MOLA topography centered on Schiaparelli basin.....	107
Ch. 3, Figure 2. Geomorphology suggestive of active hydrology.....	108
Ch. 3, Figure 3. Location quotient (LQ) matrix from dust and albedo.....	109
Ch. 3, Figure 4. LQ values grouped into LQ classes. ....	109
Ch. 3, Figure 5. Confidence levels with respect to sample size. ....	110
Ch. 3, Figure 6. Comparison of WEH Class frequency .....	111
Ch. 3, Figure 7. LQ Matrix for WEH (x axis) and MOLA (y axis).....	112
Ch. 3, Figure 8. Cluster-based LQ classes.....	113
Ch. 3, Figure 9. LQ values for water equivalent hydrogen with elevation.....	114
Ch. 3, Figure 10. LQ classes from Fig. 8 spatially projected onto the regional map. ....	115
Ch. 3, Figure 11. Map of Ares Vallis region (A) with LQ class overlay (B). ....	116
Ch. 3, Figure 12a-d. Four localities with lower than expected LQ combinations .....	117
Ch. 3, Figure 13. The LQ matrix for WEH with geologic units.....	118
Ch. 3, Figure 14. Study area with selected geologic units.....	119
Ch. 3, Figure 15. Top seven most frequent geologic units in the mapping area.....	120
Ch. 3, Figure 16. LQ values converted to classes for Dust Cover Index with WEH LQ. ....	121
Ch. 3, Figure 17. Map of LQ classes from dust cover index and WEH combinations.....	122
Ch. 3, Figure 18. LQ matrix for albedo with WEH.....	123
Ch. 3, Figure 19. Map of LQ classes from albedo and WEH matrix.....	124

Ch. 3, Figure 20. Slope (a) and aspect (b) data ..... 125

Ch. 3, Figure 21. Basemap overlain by (a) valley network and (b) valley density..... 125

Ch. 3, Figure 22. WEH with valley density LQ matrix. .... 126

Ch. 3, Figure 23. Maps of WEH with valley density from LQ matrix ..... 126

Ch. 3, Figure 24. The MOLA with valley density LQ matrix ..... 127

## List of Tables

Ch. 1, Table A. Confidence with respect to sample size. ....	30
Ch. 3, Table A. Combinatorial Or output table for classes of albedo and dust. ....	128
Ch. 3, Table B. A frequency matrix organizes the counts by combination. ....	128
Ch. 3, Table C. LQ and LQ Classes appended to the original <i>Combinatorial Or</i> output table.....	129

## **Chapter 1: Resampling Mars Odyssey data to improve hydrogen concentration resolution: balancing spatial and statistical robustness**

### **Abstract**

Epithermal neutron counts, as calculated by the Mars Odyssey Neutron Spectrometer (MONS), excel as a proxy measurement of subsurface hydrogen. Previously, due to both the size of the instrument's footprint and the need to group counts to attain an average measurement, the spatial resolution for resultant maps has been limited to  $>1^\circ$  before smoothing (at the martian equator  $1^\circ$  is  $\sim 59.25$  km). In this paper I hypothesize that a focal statistical method, moving windows, can produce hydrogen abundance maps with spatial resolutions of 463 meters per pixel or less. I specifically consider methods to overcome the challenges of limited dataset size on statistical analyses of spatial distributions by only considering the first two years of MONS data in an attempt to detect spatial patterns in hydrogen distributions. Increasing the map resolution provides a higher return on mission investment by allowing further evaluation of data from remote exploration missions with respect to the associations between hydrogen abundance and localized geomorphic or structural features. This, in turn, supports the planning of future missions.

By varying the size and shape of a moving sampling window and coupling this with nodal spacing that matches the desired pixel resolution, I created detailed maps of mean epithermal neutron counts. These gridded maps (rasters) were then converted into water-equivalent hydrogen maps in keeping with previous researchers' work. The maps were visually inspected for empty pixels and artifacts, then lines of equal concentration were plotted to compare window size models.

While the process works best with circular sampling windows, I find window size and node spacing can be adjusted to fit the needs of an area to be mapped. However, while the pixels created using this

method do represent the mean of the larger sampling window centered on that pixel, the probability that the neutrons being counted originated within the ground at that location are far less than 0.01%. In light of this, features smaller than ~250 km should be regarded as artifacts. The moving average method does, however, produce pleasing maps of MONS data, especially useful for adjusting the scale of output for direct comparison with other martian data types as long as these comparisons are limited to regional features greater than 2-3° in areal extent.

## 1. Introduction

Considering that hydrogen is the most plentiful element in the solar system (Lodders, 2003), researchers always expected to find hydrogen on Mars, especially at the poles where CO<sub>2</sub> ice seasonally covers layers of frozen H<sub>2</sub>O. Unanticipated were the two broad equatorial regions of hydrogen abundance detected by the Mars Odyssey Neutron Spectrometer (Feldman 2002; Boynton et al., 2002; Mitrofanov et al., 2002; Basilevsky, 2006; Schorghofer and Forget, 2012). The larger, examined in this study (Fig. 1), overlaps the 0° meridian in Arabia Terra while the smaller deposit relates to the Medusae Fossae formation on the other side of the planet.

The hydrogen deposits raise questions about the reasons for such equatorial highs. Perhaps these two areas were once polar caps (Schultz, 1981) or equatorial glaciers due to orographic precipitation like those discovered on Tharsis (Fastook et al., 2008; Kadish and Head, 2007). Even if other processes produced the antipodal hydrogen deposits, these areas of hydrogen enrichment may serve as proxies for locations where water existed in the past, potentially delineating optimal sites for seeking signs of microbial life. Despite ample evidence (Chou and Seal, 2007; Vaniman et al., 2004; Feldman et al., 2004c; Milliken and Bish, 2010) that evaporitic deposits of sulfates (e.g., jarosite,  $\text{KFe}_3(\text{SO}_4)_2(\text{OH})_6$ ; kieserite,  $\text{MgSO}_4 \cdot \text{H}_2\text{O}$ ; hexahydrate,  $\text{MgSO}_4 \cdot 6\text{H}_2\text{O}$ ; alunite,  $\text{KAl}_3(\text{SO}_4)_2(\text{OH})_6$ ; gypsum,  $\text{CaSO}_4 \cdot 2\text{H}_2\text{O}$ ), OH-containing silicates (e.g., kaolinite,  $\text{Al}_2\text{Si}_2\text{O}_5(\text{OH})_4$ ) can account for a portion of the hydrogen

signal, this study follows the convention of quantifying hydrogen abundances as water-equivalent hydrogen (WEH) regardless of molecular association (Feldman et al., 2002; 2004a; 2004b; 2005; 2008).

In order to determine the nature and viability of these hydrogen-rich areas, the spatial extent and intensity of the hydrogen signature with respect to the martian terrain and known surface properties must be examined. Such comparisons require that the spatial resolution of the epithermal neutron flux measurements from which the hydrogen abundance is derived be similar to the spatial resolution of the other martian datasets.

In this study I examine the data used to generate hydrogen abundance maps and introduce a method for creating geographic information system (GIS) layers for the hydrogen signal at various spatial resolutions. Using these layers, created from the first two martian years of data to represent the limited data present in the early stages of a mission, I examine the spatial extent of the eastern equatorial hydrogen maximum and delineate its probable boundaries and potential controls.

## **2. Neutron Spectroscopy**

Planetary application of neutron spectroscopy follows decades of multi-disciplinary use of neutron emissions to locate hydrogen atoms (Bacon, 1987). Mineralogists use neutron diffraction to locate hydrogen atoms within crystal lattices (Wu et al., 2010). Petroleum engineers use downhole neutron sources and detectors to locate hydrocarbon reserves (Collett et al., 2011). Hydrologists and soil scientists use similar probes to measure soil moisture (Parate et al., 2011; Vienken et al., 2013).

### ***2.1 Planetary Applications***

For planetary applications, the neutron source is a natural by-product of cosmic ray bombardment.



Unlike Earth, Mars lacks a protective magnetic field to deflect charged particles. As these particles strike the planetary surface, they collide with atoms within the regolith. Cosmic rays impacting atomic nuclei in the upper 1-3 meters of the martian regolith generate neutrons and gamma rays (Feldman et al., 2002). Energy is transferred to the neutrons, causing them to scatter throughout the subsurface. As they travel, some strike other particles, changing momentum and direction.

Hydrogen atoms in the martian regolith also interact with the neutrons produced through cosmic ray bombardment. As the mass of a hydrogen atom closely resembles that of the neutron, the presence of hydrogen in the regolith strongly and rapidly slows down the neutrons (Elphic et al., 2005). The more interactions between neutrons and hydrogen in the subsurface, the less energy the neutrons retain. Neutrons in regions of scant hydrogen often retain enough energy to escape the subsurface. Due to the thin martian atmosphere, such energetic particles may also retain enough energy to reach escape velocity and continue traveling into space.

Orbital neutron spectrometers detect the escaping non-charged particles similar to the way a Geiger counter records interactions with charged particles. The Neutron Spectrometer on board Mars Odyssey (MONS; Feldman et al., 2002) counts the neutrons encountered and records their energy levels as they contact the detector. The spacecraft logs this information while orbiting the planet at about 2.95 km/s, recording in increments of 19.7 seconds with intervening pauses of 0.3 seconds between measurements.

The quantity of neutrons detected has an inverse relationship to the abundance of hydrogen within the instrument's footprint, or spatial resolution, based on the swath of surface covered by the satellite during the measurement. Areas with little to moderate neutron detection are relatively rich in hydrogen compared to those with the highest counts. The rate of neutron emission is not constant, nor the particles themselves long-lived. The average neutron lifespan is ~15 minutes (Prettyman, 2006). The

quantity of neutrons reaching the satellite can vary above the same target from one pass to the next. For this reason, repeated measurements over the same area must be averaged to provide a better prediction of hydrogen abundance at that locality. A repeated low neutron count implies hydrogen ions within the regolith. The mean epithermal neutron count rates can be used as an end product or further converted to water-equivalent hydrogen (WEH; Feldman et al., 2004). The use of this conversion is not a presumption that there is necessarily liquid water or ice at a given location nor does its use ignore the likelihood the hydrogen exists in hydroxyl groups or is otherwise mineral-bound; rather, it facilitates use of the epithermal neutron data for isolating potential H<sub>2</sub>O occurrences, as well as for use in global climate modeling by serving as a familiar quantity (as opposed to “the soil contained 16% hydrogen”).

## ***2.2 Strengths and Limitations***

Just as EM spectroscopy divides the electromagnetic spectrum by wavelength, neutron spectroscopy classifies neutrons by their energy level. Of the three classes (fast, epithermal, and thermal neutrons) epithermal neutrons, whose energy ranges from 0.4 eV-700 keV (Maurice et al., 2011), are ideal for detecting hydrogen within the upper meter or so of regolith. In comparison, the effective penetration depth of other satellite-based spectrometers remains restricted to the upper millimeters of the martian surface. Where dust accumulation exceeds this depth, mineral identification becomes difficult.

Despite the robust detection of hydrogen beneath the dusty surface of Mars by MONS, a limitation exists on the spatial resolution of the final map products due to the spatial resolution of the instrument. For the MONS instrument, the spatial resolution is about 1.5 times the orbital altitude of 400 km; roughly 600 km or 10° of arc length (Prettyman, 2006). This spatial resolution is a function of three variables: the aforementioned orbital altitude, angular response of the instrument (roughly isotropic to weakly dependent on incident direction), and the angular distribution of surface radiation (Prettyman, 2006). The radiation distribution term is large as escaped neutrons may follow any angle of trajectory

from the regolith to the orbiter's altitude. Statistically, the distribution is broad, but the majority of neutrons escape at angles roughly normal to the surface. Escape at the lowest angles is also less frequent as greater amounts of energy must be expended. A collimator could have been included in the instrument design to filter the stream of neutrons so that only those moving roughly parallel to the desired direction reach the instrument, but the improved resolution would have come at a cost. Filtering out the sub-parallel neutrons reduces the intensity of the radiation reaching the detector (Rekveldt, 2000), thereby reducing instrument precision (Prettyman, 2006).

In addition to considering the path of the footprint as it repeats diagonally across the surface, the interactions between neutrons and the spectrometer can be visualized as a cloud of neutrons escaping from the martian surface. Areas where the cloud is denser indicate lower levels of hydrogen in the regolith below. Mars Odyssey moves through this cloud at an elevation of roughly 400 km, counting neutrons for 19.7 seconds out of a 20 s cycle. Each neutron interaction with the detector is an independent and random event. The total counts for each 19.7 second measurement are recorded as point data at the center of the footprint. The projected data points are roughly 60 km apart, so while the neutrons may have originated from anywhere within that 10° arc of the surface, the ground distance the spacecraft travels while sampling the cloud of neutrons is only 60 km.

### ***2.3 Previous Spatial Methods***

The data processing method employed also has an effect on the final map product's spatial resolution. Previously, epithermal counts have been sorted into 2° (118 km) square bins (Feldman et al., 2002) or 2° by 30° strips (portrait orientation, Tokar et al., 2002) for averaging. These methods are satisfactory for examining distributions at the global scale, but limit the spatial resolution of epithermal neutron density and water-equivalent hydrogen maps created from this process. In essence, such maps have 2° pixels. Smoothing, usually by passing a Gaussian filter over the data, effectively changes the large but

statistically accurate bins into less accurate, but more visually pleasing, maps. Where regions of interest are substantially smaller than the instrument footprint, deconvolution of the MONS data has been used in an attempt to improve spatial resolution (Elphic, 2005). In that process, the counts are summed in very small (15 km) bins, then smoothed with a full width Gaussian filter at half maximum (FWHM filtering). The resulting map is then sharpened (high-pass filtering) using an iterative process that produces an estimated pixel value.

Rather than using one of those techniques to estimate the pixel value, the intent of this study is to extract as much spatial information as possible from the epithermal neutron count data without depending on processes that might mask patterns in the hydrogen distribution that were undetectable by previous methods. To accomplish this, I turn to a neighborhood focal method common in geographic information systems (GIS). While similar algorithms are widely accepted and have been used to smooth MONS data in post-processing (Feldman et al., 2004a, 2004b) this study introduces these routines in the spatial pre-processing of epithermal neutron data, before the conversion to WEH.

### **3. Geospatial Analysis**

Overlapping moving windows (found in the neighborhood tools in ArcGIS) sample spatial point data and store the output as cells in a raster grid. Both the area sampled (also known as the neighborhood or window) and the resulting cell size (or node spacing) are flexible parameters. Contrast this with binning, for which the areas sampled are contiguous without overlapping and whose sampling window (the bin) node spacing are identical in shape and size. As there is no overlap in the sampled area, each data point falls into one and only one bin and is sampled only once (referred to as sampling without replacement). Producing the previously mentioned 2° square bins with the neighborhood tool becomes a simple matter of setting both the neighborhood size and the node spacing equal to 2°. Every data point is used only one time and incorporated into just one binned average. However, with a 2° node spacing, the

resulting 2° pixel resolution results in highly pixelated maps at all but global scales unless post-production smoothing is performed.

To increase spatial resolution, the node spacing (pixel size) must be reduced. When the sample area matches the output, as in binning, this is only feasible to a certain point, because as the number of contiguous windows dividing a study area increases, the number of data points available per bin decreases. The fewer data points per bin, the lower the certainty that the mean of those points reflects the true mean at that location. This introduces larger uncertainty into the calculation. As long as there is no resampling of data (i.e., as long as each data point is included in one, and only one, bin), there will always be a trade-off between spatial and statistical robustness.

Sampling with substitution (allowing a given data point to be sampled at multiple nodes, through the use of larger, overlapping windows) addresses the trade-off between statistical vigor and spatial robustness by providing increased flexibility with respect to node sizes while allowing sampling in the neighborhood beyond the limit of the resulting pixel. This permits processed data to be displayed at spatial resolutions that match existing datasets. For example, should I wish to compare hydrogen abundance with elevation data, a WEH map with 463 m/pixel resolution would be convenient; however, there are not enough data measurements in the first two years of martian data to allow statistically meaningful results using 463 m bins.

The principal purpose of this study is to discern the reasonable limits of the node spacing and sampling area. A common assumption in spatial analysis is that nearer things are more related than distant ones (Tobler, 1970). The implication being that sampling areas should be large enough to contain a statistically vigorous sample, without becoming so large as to compromise geographic relevance.

A text file containing point values for epithermal counts within the eastern equatorial study region (Fig. 1) provided the foundation for this study. Several window sizes were used in conjunction with a 463 m

node spacing to match the pixel size of elevation data from the Mars Orbiter Laser Altimeter (MOLA; Smith et al., 2001; Zuber et al., 1992). After performing these neighborhood analyses, the averaged counts were converted to mean epithermal neutron count rates (MENCR) and ultimately plotted as Water-Equivalent Hydrogen (WEH) weight percentage values. Figure 2 illustrates the size of the original 2° bins (Fig. 2a) relative to regional topography (Fig. 2d) and the output from the neighborhood analysis using a 2° square moving window (Fig. 2b) and that of the smallest circular window (Fig. 2c), as described below.

### **3.1 Window Sizes**

Two square and six circular moving sampling windows were used in this study (Fig. 3). For each window/node-size pairing, raster grids covering the entire region were created specifying the number of measurements ( $n$ ) at each node, the mean of the total epithermal neutron counts per measurement at each node, and the standard deviation of those counts. These three rasters ( $n$ , mean, and standard deviation) are sufficient to calculate the approximate mean WEH at each node throughout the region of interest.

The initial square sampling window (118 km wide) coupled with an identically sized node spacing resulted in contiguous square 2° bins matching those used in previous studies (Feldman, 2002) and providing a baseline comparison for the remainder of the sets (Fig. 2a). The second square window retained the 118 km width, but was paired with a 463 m node spacing (i.e., sampling with replacement every 463 m). This produced a sampling area per pixel comparable to the original map, while allowing for much smaller pixels (Fig. 2b).

Circular windows are defined by their radial distance from the nodal center. For this study, radius values of 15 (Fig. 2c), 25, 50 (Fig. 4a), 66.6, 75, and 100 km (Fig. 4b) were selected. These corresponded to 707; 1,963; 7,854; 13,935; 17,671; and 31,416 km<sup>2</sup> sampling areas.

The 50 km radius window, while approximating the width of the square window, covers less area. The 66.6 km radius window best approximates the area of the initial 118 km square window (and therefore the initial 2° bins). The largest and smallest windows were included to examine the effect of the variations in area sampled and number of measurements at each node.

Nodes (pixels) around the perimeter of the output raster are less reliable as they are calculated on partial windows that encompass areas beyond the perimeter of the region. All rasters were clipped to the same extent to remove these edge effects before further processing. Using the raster calculator tool of ArcGIS, I divided the mean total count at each node by 19.7 seconds to produce grids of mean epithermal neutron count rates (MENCN). In turn, the MENCN rasters were used to calculate WEH value rasters. The non-linear, inverse relationship between MENCN and the mean hydrogen abundance in the footprint of the instrument can be described by the equation (Elphic, Rick. "Relating epi count rate to H2O abundance." Message to the author. Aug. 2005. Email.; Prettyman, Thomas. "Power law relationship between WEH and neutron counts for a homogenous, single layer." Message to the author. Sept. 30, 2014. Email.):

$$Wt\%WEH = 100 * \left( \frac{[29.306 / (MENCN - 1)]}{29.099} \right)^{1.3275} \quad (1)$$

Figure 5 depicts the relationship between epithermal neutron flux rates and weight percent water-equivalent hydrogen (WEH) in the footprint of the instrument. Below a MENCN value of 5, the corresponding WEH increases asymptotically from 40 wt.% to 100%. In this range, uncertainty increases rapidly. Similarly, the exponential decrease in WEH as MENCN increases suggests values below 3 wt.% could be spurious. Therefore the focus of the analysis is on the range 3 to 16 mean epithermal neutron counts per second.

### **3.2 Statistics**

Maurice et al. (2011) have shown that at low latitudes, such as this equatorial-based study, there is a 99% probability that the measurements per pixel are that of a random population. This is important as it allows us to represent each window by its mean value and a statistical error bar. According to the Weak Law of Large Numbers, it is possible to know with 99% certainty that the sample mean of a near infinite population will fall within half of a standard deviation of the true population mean if there are 400 samples (Bernoulli, 1713; Seneta, 2013). As sample size decreases, so does certainty. Table A illustrates the certainty as correlated to the number of measurements sampled. For example, if the number of data points falling within the window is between 100 and 133, then there is a 96% certainty that the mean value of those sampled points would fall within half a standard deviation of the true population mean for that location, even if the population were nearly infinite. This convergence in probability provides the means to evaluate the statistical robustness for each window size based solely on the number of epithermal records sampled at each node. Preparation entailed creating raster grids for the entire region containing the number of epithermal records sampled at each node for each window configuration. To convert these count rasters to certainty values for statistical analysis, a classification system was derived from Table A. A reclassification algorithm replaced the counts with the appropriate certainty percentage.

In addition to the certainty raster, two additional rasters were created for each window size. These rasters show the results of calculating the sample mean  $\pm$  half the standard deviation at each node to produce the bounds within which the population mean should fall. Due to the inverse relationship between WEH and epithermal neutron flux, the upper WEH bound is determined by subtracting, and the lower WEH bound by adding, half of the standard deviation to the nodal mean.

By layering the certainty raster with the mean, upper, and lower WEH bound rasters within ArcGIS, it is



possible to select a point on the map and read the values for all four rasters at once for each window configuration.

#### **4. Evaluation of the Moving Window Technique**

Two methods, visual inspection for artifacts and isocon comparisons, were used to gauge the effect of window size on the resulting map layers using the moving window technique. The node spacing/pixel size is 463 m throughout.

##### ***4.1 Visual Inspection***

While the square moving window function successfully produced an output map with higher spatial resolution (more pixels per meter) than the original bins, it produces horizontal and vertical artifacts (as shown in a small portion of the full study region in Fig. 6a). In addition to generating a misleading image of the nature of the epithermal counts, these artifacts could potentially mask genuine linear hydrogen features created by north- or east-trending linear features (e.g., faults), defeating the purpose of generating high-resolution rasters. Because of these artifacts, no further square window analyses were used. However, as the size and shape of the square window function closely resembles the original 2° bins, I will continue to refer to the values produced by this method as a benchmark for conventional sample size (n), mean total counts, and standard deviation.

When circular windows are selected (Fig. 6b), the resulting raster maps lack the linear features generated by the square window function. However, a curious pattern emerges when using circular windows smaller than 50 km radius. Arcuate artifacts appear, equal in diameter to the moving window (e.g., 15 km radius, Fig. 6b), where clusters of nodes with no data have convex boundaries and those containing values appear as rows of overlapping windows.

Rasters made from the 25 km radius window show fewer artifacts (Fig. 6c) and those produced by the 50 km radius window only display this pattern in areas where the WEH values increase to 16 wt.% or

higher. Nodes in these areas contain more than 80 measurements, so the development of this arcuate artifact appears unrelated to a lack of data. These areas do contain widely varying WEH values, however, which may be partially responsible for the effect.

The raster produced by the smallest window (15 km radius) contained dozens of No Value (empty) cells where zero data points fell within the respective node's window (red areas, Fig. 6b). These nodes cluster between integer lines of latitude and are due to the grouping of spectrometer data points (gray dots). This pattern persists even after including additional years of MONS data and should be seen as an artifact of the derived neutron data set. As none of the nodes from this diminutive window contained more than 26 measurements, this size window was not considered further. The minimal data points ( $n$ ) represent a reduced certainty and compromise the statistical vigor of the output raster. The remaining five windows (100 km, 75 km, 66.6 km, 50 km, and 25 km) generated no null cells except those few pixels existing as edge effects. These areas of lower sample size were removed by clipping all the raster maps to the same map extent (Fig. 1).

#### ***4.2 Contours of Equal Concentration***

Creating isocons, lines of equal WEH concentration, from the WEH rasters, allows us to compare the remaining circular moving window methods. These lines are largely congruent when the results from multiple window sizes are superimposed (Fig. 7a), the main distinction being that smaller windows produce more detail, resulting in undulating bands of equal concentration, occasionally to the point of nearly filling in the area between the isocons of the larger windows. The isocons produced by the 25 km radius window produce a nearly solid coverage of the map area with localized areas of increased variability creating islands of higher or lower concentration. The larger windows smooth out the signal and for the most part produce less recursive, more widely spaced isocons. There is a notable exception to this generalization where the isocons cross the albedo boundary between Schiaparelli and Dawes

craters (Fig. 7b). Lines representing 14 and 15 wt.% WEH are equally sinuous north and south of the boundary, but become recursive, creating a band (between the dashed lines) along the edge of the albedo boundary within which isocons are offset to the northwest. Even the eastern end of this band, where the two isocons nearest Dawes are match up on either side of the boundary, isolated dips in hydrogen abundance form closed, recursive isocon loops between the dashed lines. West of Pollack crater, the isocons are misaligned across the albedo boundary, but still show a westward shift in the band.

Areas of maximum weight percent water-equivalent hydrogen form a semi-circle about the eastern side of Schiaparelli Basin (Fig. 8). A map of the isocons formed by the 100 km radius window shows six areas that exceed 16 wt.% WEH. Using a clock analogy, these are arranged in an arc from 12 (north of Schiaparelli Basin), clockwise to 6 (directly to its south) (Fig. 8a). When viewing the undulating isocons created from the 50 km radius window, the zone of maximum concentration extends from 11 to 7 clockwise (Fig. 8b). The six disconnected areas in Fig. 8a have expanded, causing some areas within the high albedo area to become continuous. There are also areas where the WEH increases beyond 18 wt.% (red isocons in Fig. 8b). The band (Fig. 7b) along the border between high and low albedo is a relative minimum separating the maxima at Pollack Crater, located within the dark albedo area, from Tuscaloosa Crater, 500 km north-northeast in the bright albedo.

Isocon spacing highlights abrupt slopes in the data where the concentration changes rapidly over relatively short distances. In the 100 km radius window data, the most rapid change in WEH is where the signal fades westward from Vernal Crater toward Ares Vallis (Fig. 9). Here the WEH values decrease from concentrations of 12 to 9 wt. % WEH over less than 300 km. The same transition is spread over 400 to 1300 km elsewhere on the map. The smallest change in hydrogen concentration occurs on the western edge of Schiaparelli Basin, where it takes 900 km for WEH to decrease from 13 to 12 wt.%. These rapid changes in elevation, more noticeable when the data is

displayed as isocons, provide visual clues to the apparent edges of the hydrogen enrichment's extent. Even if creating isocons from the 2° bins were desirable, the level of detail would not be equivalent (Fig. 2a, compare the isocons to the bin edges).

## **5. Discussion**

While the methods used in this study have proved useful in delineating the extent of the equatorial hydrogen anomaly, the statistics used do not fully capture the probability that the WEH value assigned to each pixel faithfully represents the mean epithermal neutrons detected within the sampling window. In addition to a more complete statistical estimate, this section contains three alternative calculations based on moving windows that can retain the small node spacing while reducing artifacts generated by the <2-3° sampling windows.

### ***5.1 Spatial Extent***

A comparison of the two methods reveals variations in the hydrogen signal that can be used to determine the extent of the deposit. Both methods indicate a rapid change in water-equivalent hydrogen along the western edge of the map (Fig. 9a) from 8 wt.% WEH at Ares Vallis extending eastward past Crommelin Crater (10 wt.%) to 13 wt.% at Vernal Crater. From that crater eastward, parallel to 5° latitude, hydrogen abundances rise and fall but do not reach 12 wt. % again until ~50° E. The 12 wt.% contour (Fig. 10, medium gray) encloses an area over 3000 km in diameter, bounded by Focas Crater to the north, Bakhuisen in the south, Crommelin to the west, and the eastern edge of the map. Inside this area the elevation varies from over 4 km 250 km west of Dawes Crater to -4.45 km in the center of Curie Crater. WEH abundances exceed 16 wt.% at the center (Fig. 10, dark blue) of the hydrogen signal. The southeast portion of the map contains heavily cratered highland terrain while the northwest portion dips toward the NW and has smoother features that show some indications of past surface hydrology including fretted terrain, pedestal craters, and relic drainages. The slope from the

lowlands to the highest point of the cratered terrain is unique as it is the lowest, broadest transition from these two terrains. This type of gradient, when combined with a prevailing wind, forces parcels of air upslope allowing them to expand and cool beyond their dew point. The resulting clouds could be the source of the original hydrogen in the area.

Two other spatial features, the Big D and the Western Gap (Fig. 10, dark gray isocon and labeled feature), define visual boundaries in the regional hydrogen "deposit" in Arabia Terra. The Big D is defined by the 10 wt.% isocon. In addition to the overall shape, rounded to the east and flattened on the west, like a capital D, the southwest corner protrudes much like a typographic serif. This protuberance contains a circular indentation (Fig. 10, crater) that excludes most of a weathered crater (between Peta and Newcomb craters, Fig. 9a) from the elevated WEH surrounding it. If, instead of the 10 wt.% isocon, the 9.5% line is used, a minimum appears not only over the unnamed crater but over Peta as well. Not all craters display locally lower hydrogen abundance, but the older, larger (>300 km) craters (Schiaparelli, Cassini) often do. This may suggest the hydrogen was bound in a stratigraphic layer before the heavy bombardment and was disrupted by larger impactors; that orographic processes producing the hydrogen signature preferentially passed over the flat, plain-like bottoms of the large basins in favor of their rims and surrounding terrain; or that the hydrogen enrichment is there, but mantled by more recent processes that have occluded the signal. The Western Gap (Fig. 9a, b; Fig. 10) is another such region of depleted hydrogen. The 13 wt.% isocon exposes this >900 km long feature extending from the center of Schiaparelli to Airy Crater. Its largest breadth exceeds 400 km. This hydrogen-depleted region is associated with elevations in the 50 to -1000 m range and is aligned with the division between cratered Noachian highlands and the transitional terrains where Arabia dips toward the dichotomy boundary. The 14 wt.% isocon further defines the gap and illuminates a washboard effect north of the gap (Fig. 10). In this area, from Henry west to Endeavour, the strength of the hydrogen signal pulses and wanes. These irregularities in the WEH signal imply that whatever

controls the occurrence of hydrogen has been disrupted here. A similar washboard effect may be produced where undulating layers are eroded, leaving repeating swaths of the top unit exposed in the synforms.

Using the moving window methods, at least two spatial constraints on the eastern equatorial hydrogen can be predicted. The outer edge appears to fall between the 8 wt.% and 10 wt.% isocons. By 10 wt.%, a rapid increase in WEH begins at Crommelin and other locations. A possible interior boundary, the 14 wt.% WEH isocon, suggests a linear feature control on WEH just north of Henry (Fig. 10, above WH). Relationships between hydrogen abundance and other parameters such as elevation, the slope and aspect of hillsides, and surface features and material are explored in Chapter 3.

## ***5.2 Corrected Statistics***

Unfortunately, the statistical certainty of the results depends on a set of probabilities, and not solely on the number of measurements in the sampling window. This number is, however, the only portion of the probability equation that can be adjusted after the measurements are recorded. This probability, P1, depends on the quantity of epithermal neutron count measurements at each node as noted in Section 3.2 and Table A. As was shown, it is possible to increase the probability that the average of the sampled data points approaches the true population mean by increasing the size of the sampling window to include a minimum of 400 measurements (Table A).

To calculate probability P2, Maurice et al., 2011 have shown the distribution of neutron counts within the two degree window follow a Gaussian (normal) distribution (i.e., the histogram of data points exhibits a bell shape). In a normal distribution there is a 38% probability that the actual count rate at the node is within one half of the standard deviation of the mean. Thus probability P2 is 0.38.

Probability P3 is related to the conversion of count rates to WEH and depends on the instrument footprint. The footprint of MONS is a Gaussian distribution with an FWHM of 550 km. For a Gaussian

distribution, FWHM is equal to 2.35 times the standard deviation. So the standard deviation of the distribution of the counts is about 234 km. For large numbers, the Gaussian distribution is close to a normal distribution, so consider a normal distribution with a standard deviation of 234 km. centered on a 463 m pixel. The points within this tiny pixel lie within about 0.001 standard deviations of the footprint. The probability that a neutron counted above that pixel was actually emitted from the ground below that pixel is about 0.08%. There is about a 38% probability that they were emitted in the surrounding two degree sampling window and about a 68% probability that they were emitted from elsewhere in the footprint. Thus probability P3 is a minuscule 0.0008.

The net probability that the MENCR calculated for any node within a two degree sampling window is within half a standard deviation of the sample mean is given by  $P1 \times P2$ , about 0.38. at best, depending on the number of points in the sampling window. Furthermore, the chance that the WEH value falls within the range estimated by the confidence limits computed for the MENCR is P3 or 0.0008. Finally the overall probability that the WEH calculated at any node by the proposed process ( $P1 \times P2 \times P3$ ) is virtually nil.

### ***5.3 Smoothing, kernel approximation, and spacing***

In light of the artifacts created using the single-window moving averages I offer three alternate methods for refining the moving window technique to reduce these artifacts. The first imitates a Gaussian smoothing function; the subsequent two increase spatial robustness. Although these methods were not used in the analyses of Section 4, their general effect on the regional map was evaluated (Fig. 11).

*Smoothing.* A statistical approach for properly approximating a Gaussian (smoothed) average would be to take one of the MENCR maps and, node by node, average the pixels that fall within the sampling window, then taking the resulting raster and repeating the process on its pixels. Repeating the process

of resampling each newly created raster for 3 or more iterations produces a 4<sup>th</sup> iteration (or more) smoothed data product. This cannot be done with the binned map, as the initial node spacing is exactly the window size. While any of the other window-node combinations would work, I first chose to resample one of the smaller circular windows. The 50 km radius window was passed over the original unclipped 463 m node raster created by the 50 km moving window. This procedure created a second iteration of the 50 km radius window. In this instance, the  $n$  represents the number of nodes (pixels) per window sampled at each node rather than number of MONS datapoints. This process was repeated a third and fourth time, and the fourth iteration converted to WEH values (Fig. 11a). This smoothing minimizes noise and might be applied if the number of data points per original window varied greatly across the raster. The resulting 4<sup>th</sup> iteration WEH map differs from a map produced by binning (Fig. 2a) in its spatial robustness. Statistical robustness would still depend on the number of nodes within each sampling window.

*Kernel approximation.* Kernel weighting functions can be adapted to either enhance or smooth localized highs and lows in plotted data. Layers created from various window sizes can be averaged, giving more weight to values close to the central node and including distant values with lower weighting. By averaging the 25, 66.6, and 100 km radius window rasters, it is possible to approximate a kernel function that does not over-smooth local variations, but still takes into account measurements 100 km from the center of the node. The values at each node of the output raster were obtained by counting the measurements within the inner 25 km radius 3 times, those in the torus between 25-66.6 km radius twice, and data points within the outer 66.6-100 km radius torus once (Fig. 11b). While a Gaussian kernel has the shape of a normal distribution, the three-layer average approximates a stepped kernel with a flattened top. As the largest window exceeds the minimum 2° threshold, it cuts down on the sort wavelength artifacts.

*Spacing.* The moving window technique can also be refined by reducing the node spacing. The increase



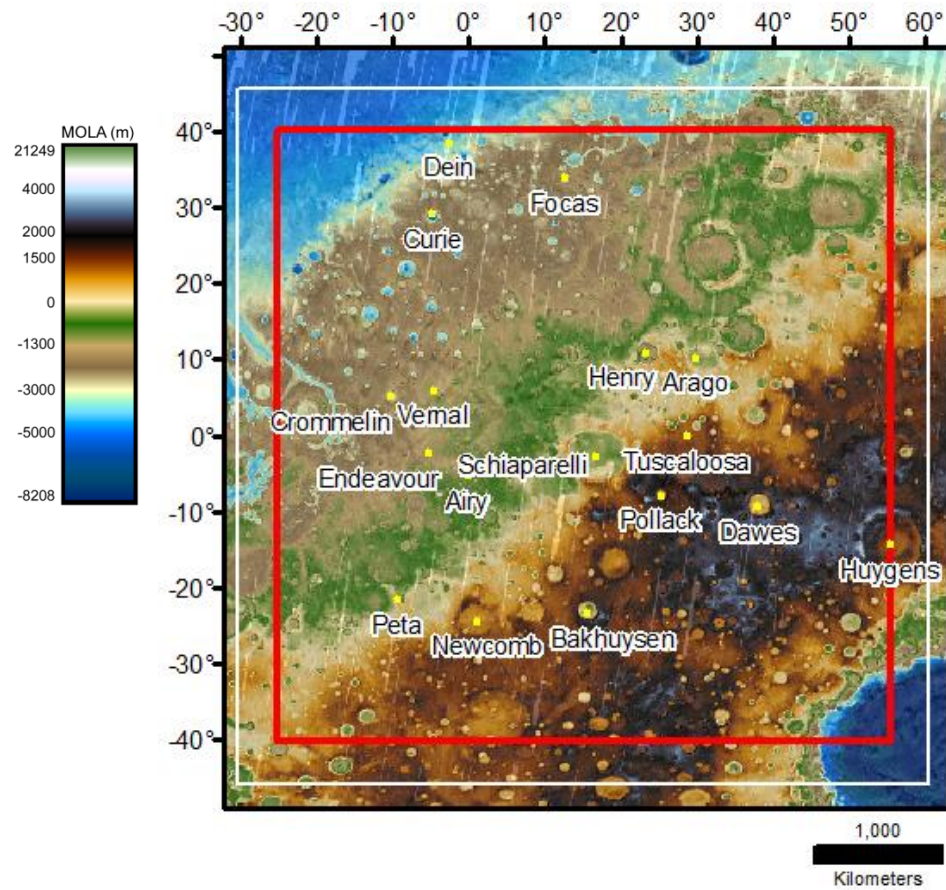
in spatial resolution must be weighed against the increased file size and the reduction in data points per window/node pairing. The node spacing was reduced to match the spatial resolution of the daytime infrared images from THEMIS (~231 m) and paired with the 50 km radius window (Fig. 11c). As with the other resampling techniques in the study, the window size can still be adjusted to include as many data points as necessary to provide statistical confidence. As with the previous example, a 100 km radius window would work to minimize the short-wavelength artifacts. This method simply increases the resampling over the study area for any window size.

## 6. Conclusions

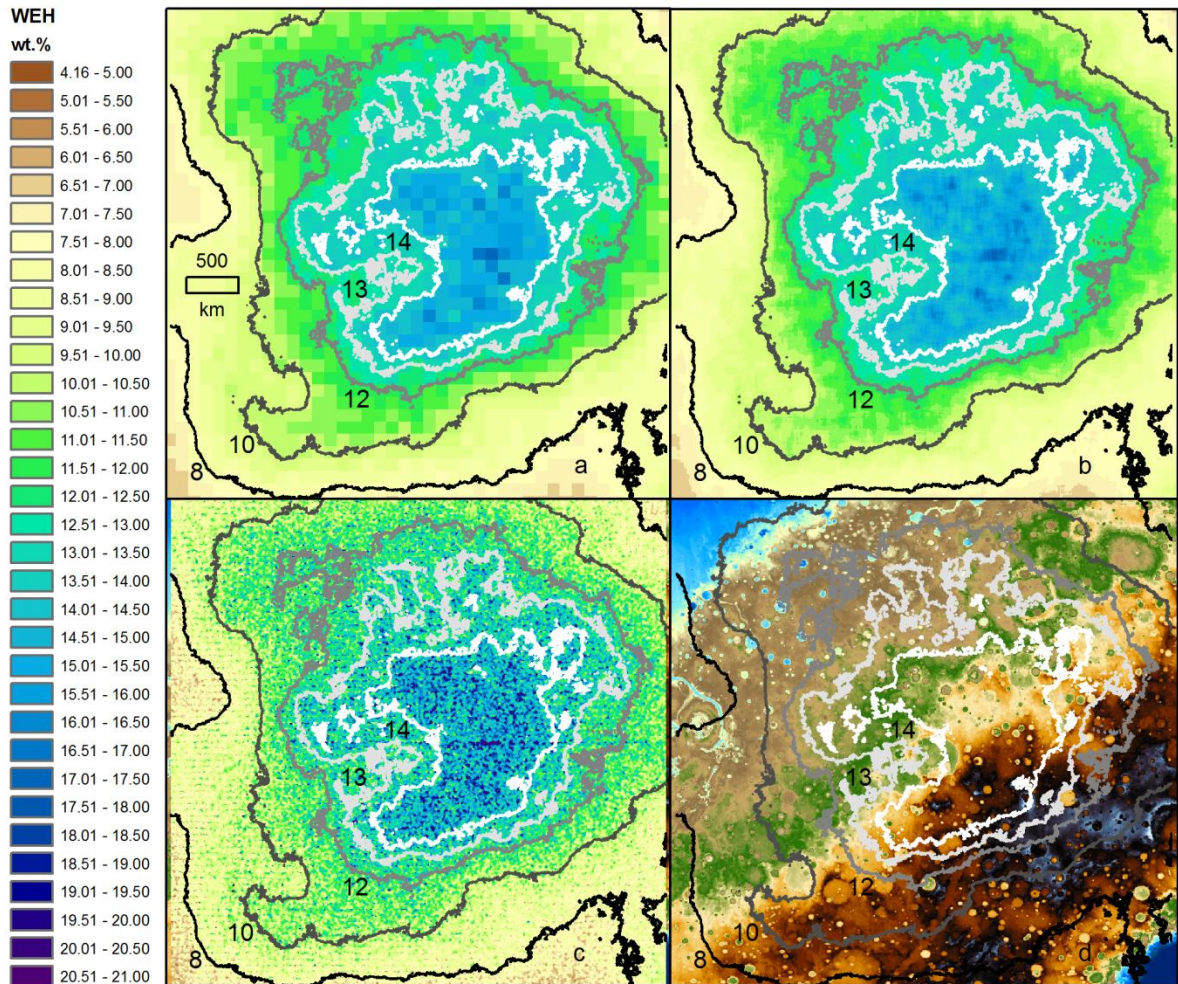
While the initial hypothesis was shown to be false, in that moving windows and sampling with replacement could not produce sub-kilometer pixels without introducing artifacts, the method does create maps of MONS data useful for comparison with other martian data in their native resolutions. Users must be aware that the results of such comparisons should focus on regional features greater than 2-3° in areal extent. The short spatial wavelength artifacts can be responsible for variations in the MONS data that are spurious at smaller scales.

Also, the Gaussian distribution of data points noted in Maurice et al. (2011) moderates the probability that the mean from the sampling window approaches the population mean for the area above the pixel to 38%, no matter how many measurements were included in the sampling window. Most tellingly, the useful spatial resolution, in terms of WEH, is limited by the inherent resolution of the MONS instrument footprint. Sampling windows would need to be at least 2-3° in size to have even a 50% probability of resolving the WEH in the ground beneath the window. Even if the neutron count rate above a sub-kilometer pixel were perfectly known, the chance that the neutrons in the sampling window were actually emitted from the ground beneath that pixel are miniscule ( $\ll 0.01\%$ ).

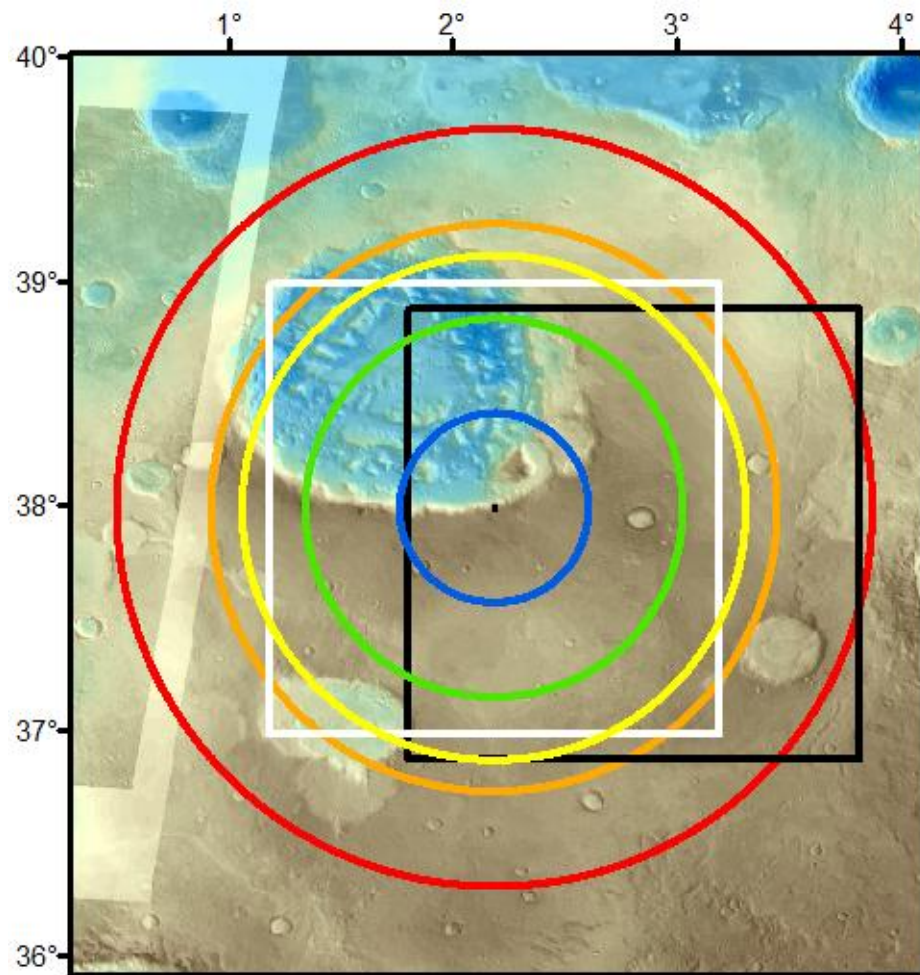
## Chapter 1 Figures



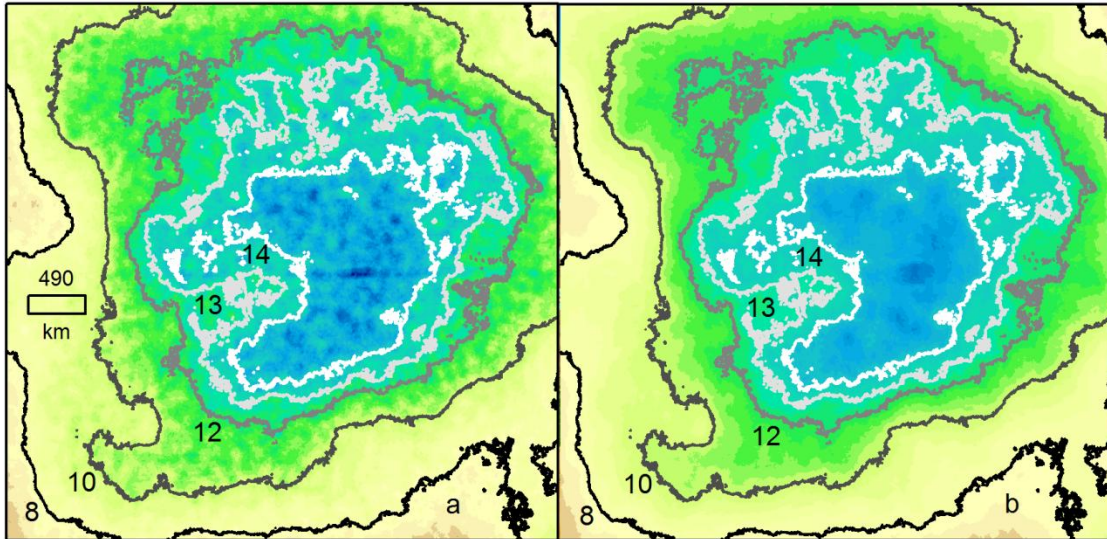
Ch. 1, Figure 1. Map of region of interest. White box marks the full extent of the neutron spectrometer measurements used in this study. Red box defines the clipped extent of the water-equivalent hydrogen maps. Elevation ranges from ~4 km along the rim of Huygens crater to less than -7 km in the southeast corner. This color ramp will be used for all elevation maps in the study. Labels identify pertinent craters



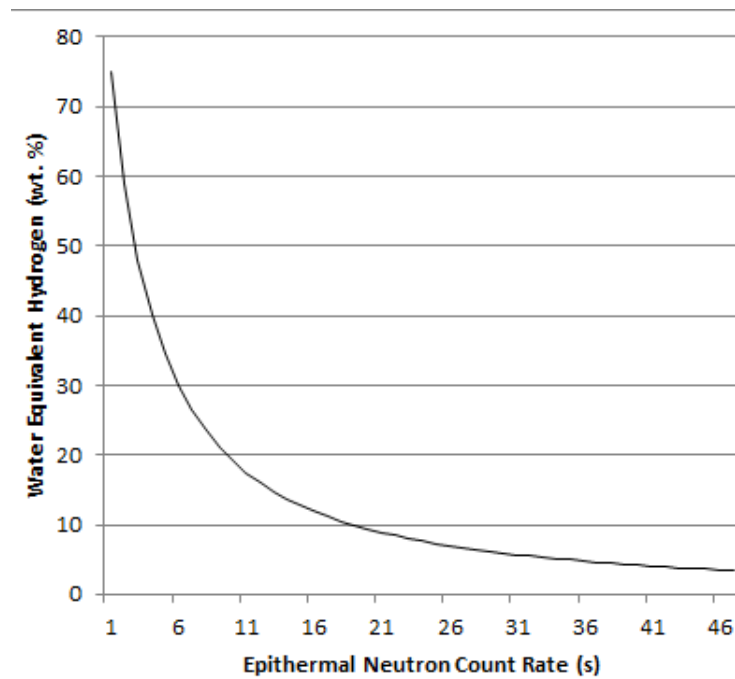
Ch. 1, Figure 2. Comparison of binning and moving window results for maps of water-equivalent hydrogen. (a) Original  $2^\circ$  binning produces large pixels and little spatial detail. (b) A square moving window the same size as the  $2^\circ$  bins provides greater resolution, but produces linear artifacts (cf., Fig. 5). (c) Circular moving windows do not display linear artifacts; however, a too-small window radius, here 15 km, can produce cells with no values or arcuate artifacts (cf., Fig. 6), especially in areas with few data points or where data values change rapidly over a small spatial extent. (d) Reference map of MOLA elevation overlain by isocons, lines of equal concentration of WEH, produced from the 100 km radius windows. See Fig. 1 for elevation legend.



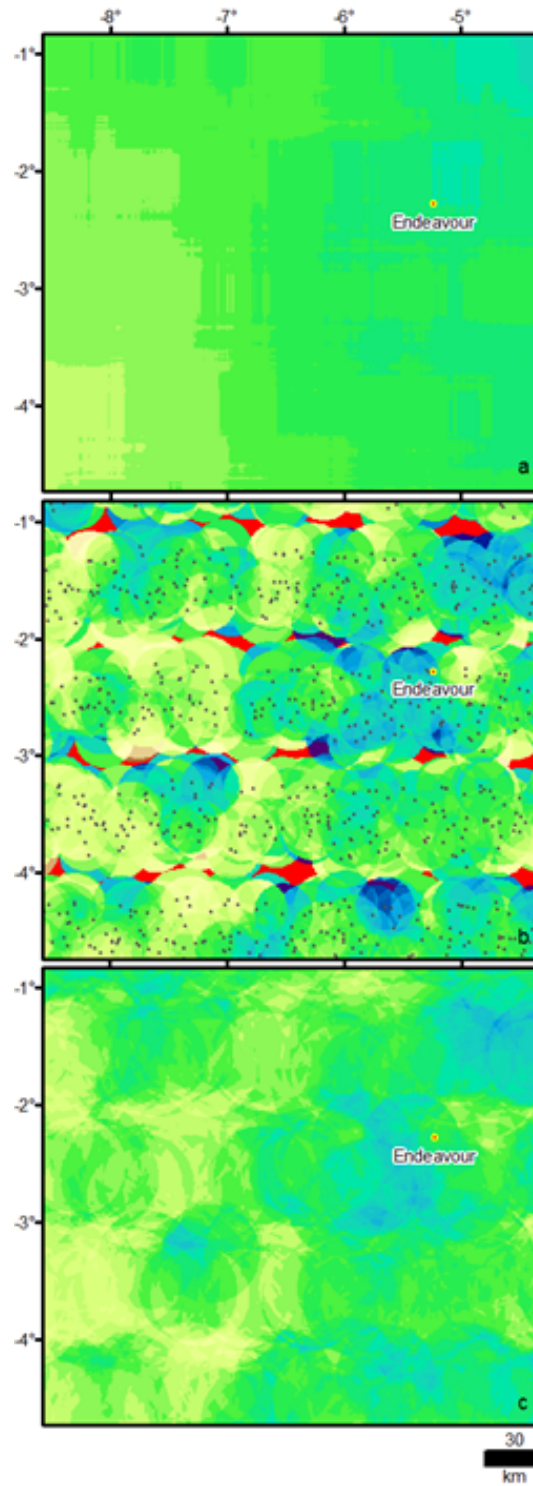
*Ch. 1, Figure 3. Scale comparison of sampling windows. The 2° bin (black square) and resampling windows as positioned at the central node (black dot) of the Northern Edge site. Moving window sizes are 2° (white square), and circle radii of 100 km (red), 75 km (orange), 66.6 km (yellow), 50 km (green), and 25 km (blue). Note that while the moving windows are centered on the node, a bin's position has no node. See Fig. 1 for elevation legend.*



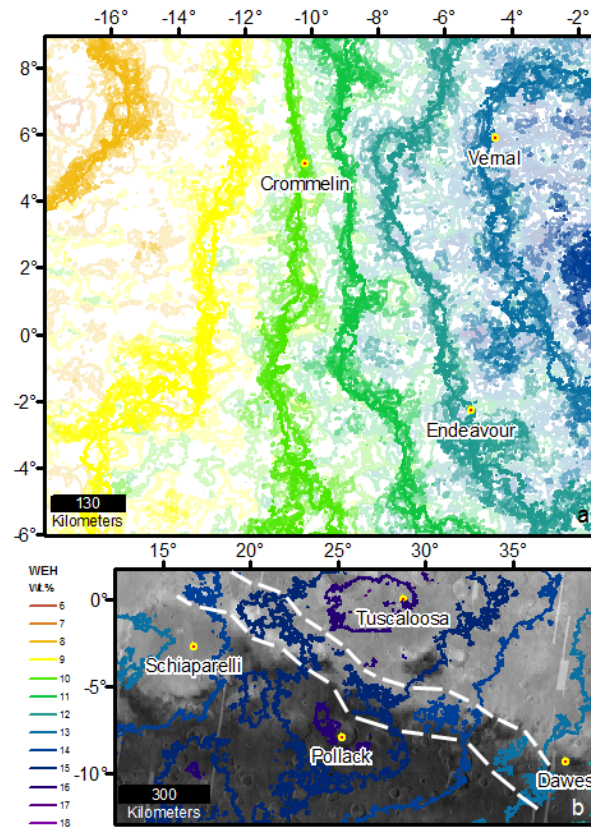
Ch. 1, Figure 4. Window radius controls the degree of smoothing. By incorporating and averaging data at greater distances from the central node a smoothing effect is achieved without reducing statistical vigor. (a) A radius of 50 km retains localized highs and lows. (b) Increasing the window radius to 100 km may mask local hydrogen signals. See Fig. 2 for legend.



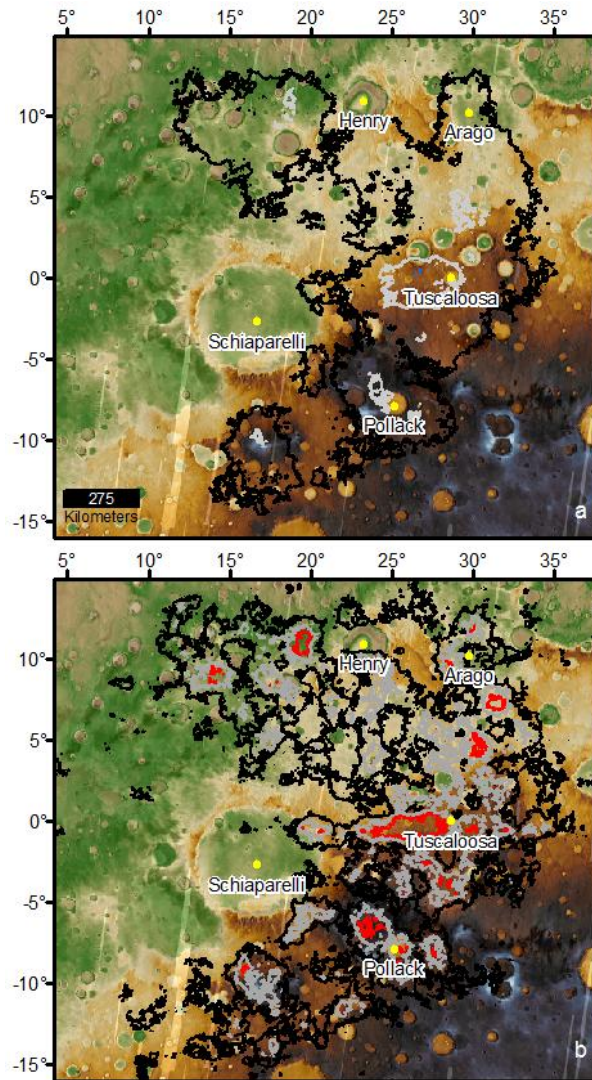
Ch. 1, Figure 5. Relationship between epithermal neutrons and hydrogen abundance. As neutron count rates increase the weight percent of hydrogen, and therefore Water Equivalent Hydrogen, decreases.



Ch. 1, Figure 6. Artifacts produced by square or undersized sampling windows. Results displayed: (a) 118 km square, (b) 15 km radius circular, and (c) 25 km radius circular moving windows. Gray points in (b) show the location of spectrometer data center points. Red areas highlight nodes where no data fell within the window. Even with additional years of martian data, the data points cluster between the lines of latitude. See Fig. 2 for legend.

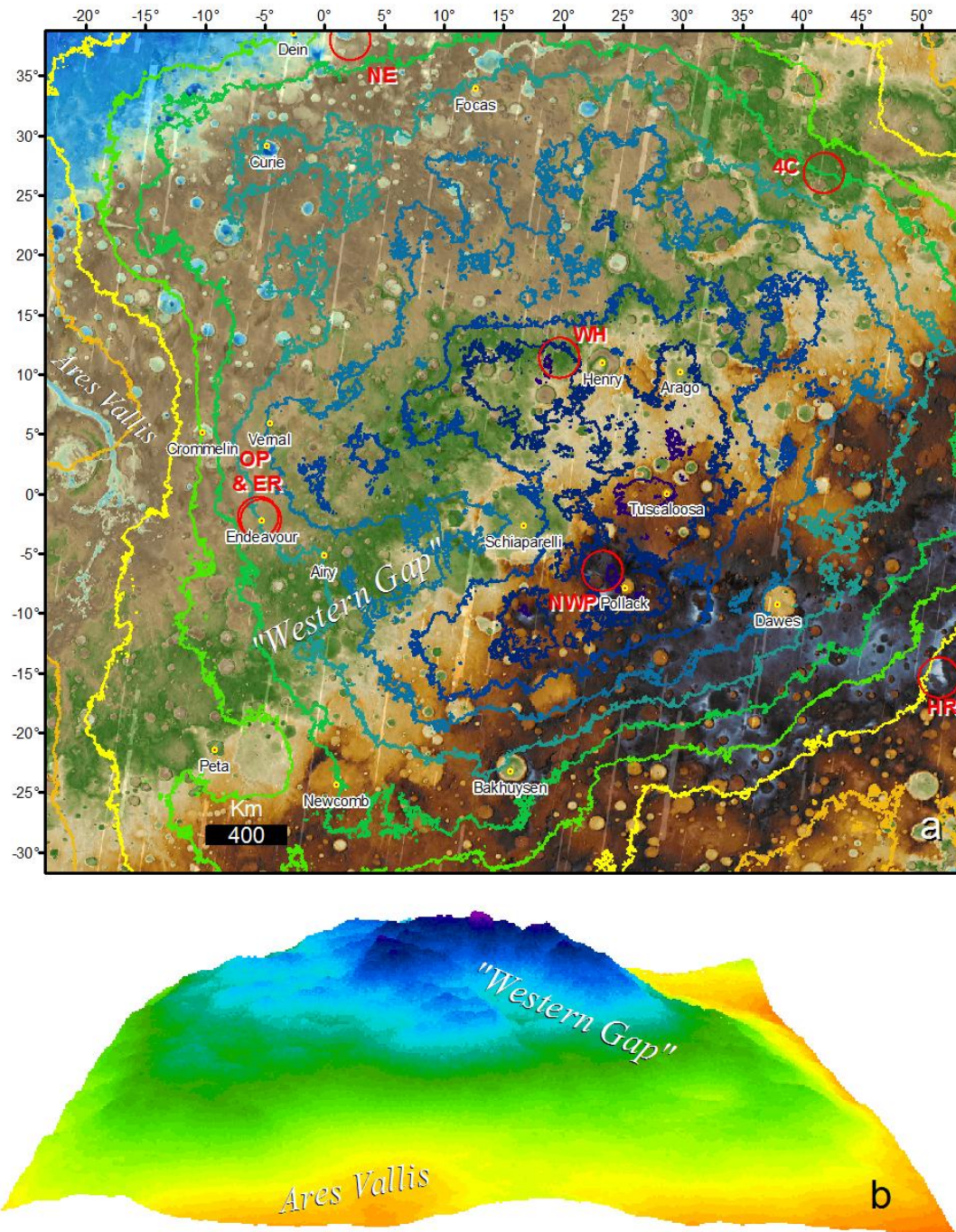


Ch. 1, Figure 7. Superimposed WEH isocons (a) for various circular window sizes with the largest displayed as opaque and subsequent sizes increasingly transparent. The isocons from the smallest window (25 km radius) are so recursive they nearly cover the region. Isocons become less undulating as window size increases. As the isocons cross the boundary between high and low albedo (b) they offset to the northwest in a band (between dashed lines) ~110 km wide. North and south of this band, the lines are congruent.

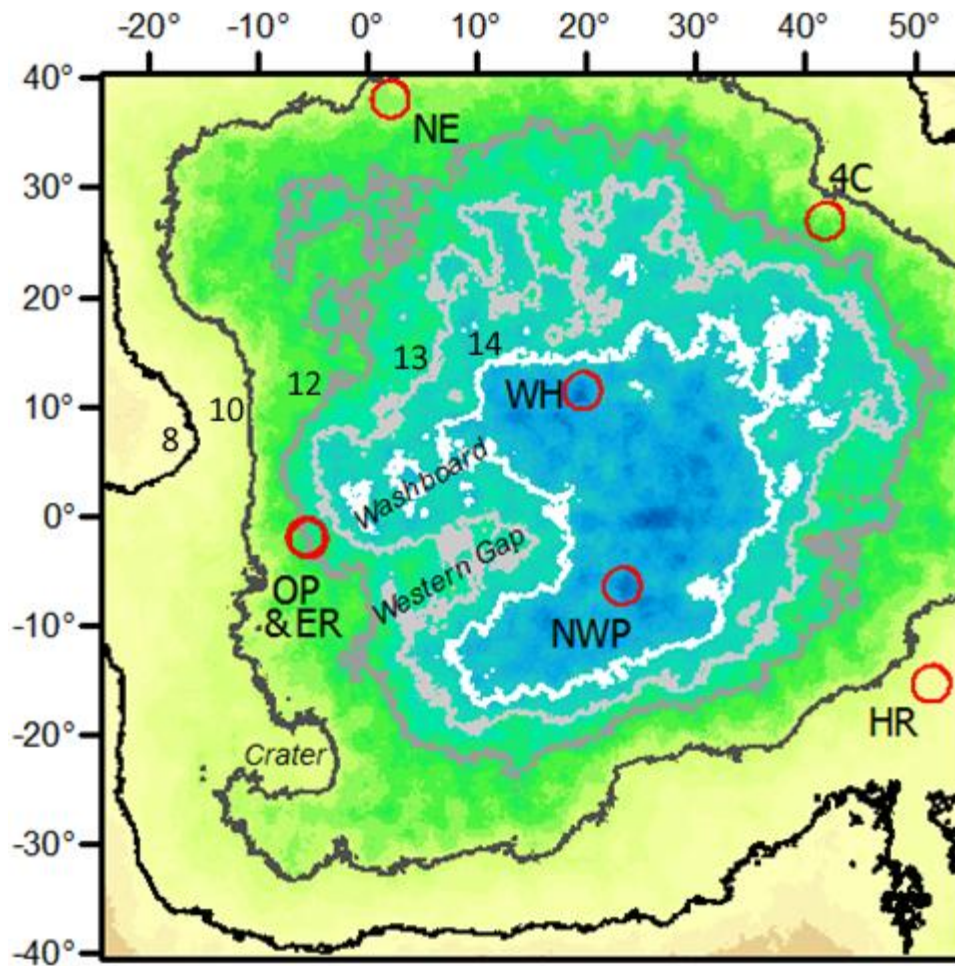


Ch. 1, Figure 8. Areas of maximum wt.% WEH form a semi-circle around Schiaparelli Basin. (a) Large window (100 km radius) regions of >16 wt.% WEH extend clockwise from 12 to 6 o'clock, with six discrete 50 to 325 km wide areas of at least 17 wt.% WEH. (b) Smaller window (50 km radius) isocons show both higher overall values and a greater extent (11 to 7 o'clock). More than a dozen areas exceed 18 wt.%. Isocon values are 16 wt.%, black; 17 wt.%, gray; and 18 wt.%, red. See Fig. 1 for elevation legend.

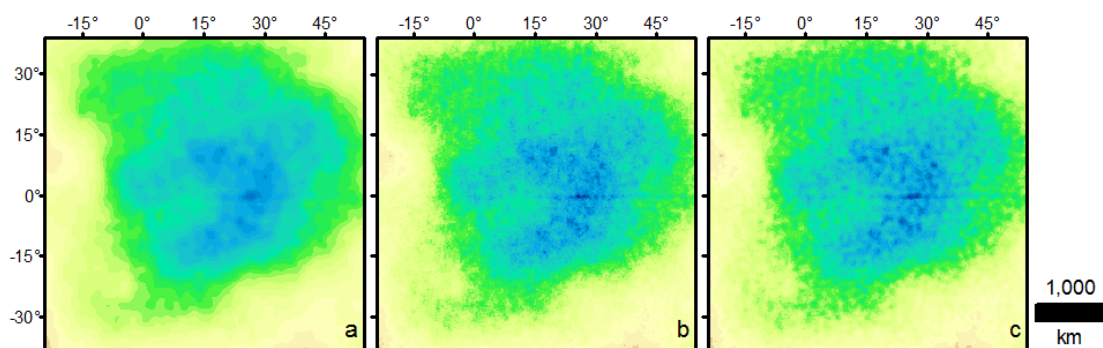




Ch. 1, Figure 9. Lines of equal WEH concentration. (a) Isocons are spaced very closely from Vernal Crater west toward Ares Vallis, but broadly spaced between Schiaparelli Basin and Airy Crater (see Fig. 7 for WEH legend). Node study locations (centers of red circles) were chosen either for proximity to locations to the Opportunity rover's travels (OP and ER), because of bin-to-node congruence (4C, Four Corners), or by stratified sampling to randomly select a location that met WEH criteria. Each circle measures 100 km in radius, the extent of the largest resampling window from the central node. (b) A 3D model of the WEH values (looking eastward across the entire study area) depicts the changes in concentration. See Fig. 1 for elevation legend.



Ch. 1, Figure 10. Regional map with WEH isocons and sampling areas (red circles). Contours are labeled in wt.% WEH. The 8 and 10 wt.% WEH isocons (black discontinuous line and dark grey "Big D"), define the outer edge of the regional hydrogen deposit. The interior minimum value (12 wt.%) and the two inner lines outline internal variations that create the Western Gap.



Ch. 1, Figure 11. Alternative methods for establishing WEH distributions. Techniques include (a) a 4th iteration approximation of Gaussian smoothing, (b) a weighted mean calculation comparable to a kernel function, and (c) a node spacing variation (~231 m rather than the 463 m used throughout the study). See Fig. 2 for legend.

## Chapter 1 Tables

*Ch. 1, Table A. Confidence with respect to sample size. Certainty that the sample mean is within half a standard deviation of the population mean with respect to window sample size  $n$  for  $P1$ .*

	Range of $n$	%Certainty
$\infty$	400	99
399	200	98
199	134	97
133	100	96
99	80	95
79	67	94
66	58	93
57	50	92
49	45	91
44	40	90
39	37	89
36	34	88
33	31	87
30	29	86
28	27	85
26	25	84
24		83
23		82
22		81
21	20	80

## Chapter 1 References

- Allen, C.C., Oehler, D.Z., 2008. A case for ancient springs in Arabia Terra, Mars. *Astrobiology*, Vol. 8, no. 6, doi:10.1089/ast.2008.0239
- Bacon, G. E., 1986. Fifty years of neutron diffraction: The advent of neutron scattering. Bristol: Hilger, International Union of Crystallography.
- Basilevsky, A. T., Rodin, A. V., Raitala, J., Neukum, G., Werner, S., and six others, 2006. Search for causes of the low epithermal neutron flux anomaly in the Arabia Terra region (Mars). *Solar System Research*, 40.5, 355-374.
- Bernoulli, J., 1713. *Wahrscheinlichkeitsrechnung. Ars conjectandi*. Ostwalds Klassiker der exakten Wissenschaften, W. Engelmann, Leipzig, 1899.
- Boynton, W. V., Feldman, W. C., Squyres, S.W., Prettyman, T. H., Brückner, J., and twenty others, 2002. Distribution of hydrogen in the near surface of Mars: evidence for subsurface ice deposits. *Science*, 297, 81-5.
- Chou, I., Seal, R. R., 2007. Magnesium and calcium sulfate stabilities and the water budget of Mars. *Journal of Geophysical Research: Planets*, (1991–2012), 112(E11).
- Clevy, J.R., Elphic, R.C., Feldman, W. C., Kattenhorn, S.A., 2005 Relationship between topography and the eastern equatorial hydrogen signal on Mars. *Eos, Transactions of the American Geophysical Union* 86, Fall Meeting Supplement, P31C-0220.
- Clevy, J.R., Kattenhorn, S. A., 2009. Localized seasonal variations in Water Equivalent Hydrogen on Mars and possible relationship to recent impacts. *Lunar and Planetary Science Conference 40*, 2265.
- Collett, T. S., Lewis, R. E., Winters, W. J., Lee, M. W., Rose, K. K., Boswell, R. M., 2011. Downhole well log and core montages from the Mount Elbert Gas Hydrate Stratigraphic Test Well, Alaska North Slope. *Marine and Petroleum Geology*, 28, 561-577.
- Elphic, R.C., Feldman, W. C., Prettyman, T. H., Tokar, R. L., Lawrence, D. J., Head, III, J. W., Maurice, S., 2005. Mars Odyssey Neutron Spectrometer Water-Equivalent Hydrogen: Comparison with Glacial Landforms on Tharsis. *Lunar and Planetary Science Conference 36*, 1805.

- Fastook, J. L., Head, J. W., Marchant, D. R., Forget, F., 2008. Tropical mountain glaciers on Mars: Altitude-dependence of ice accumulation, accumulation conditions, formation times, glacier dynamic, and implication for planetary spin-axis/orbital history. *Icarus*, 198, 305-317.
- Feldman, W. C., Boynton, W.V., Tokar, R. L., Prettyman, T. H., Gasnault, O., and eight others, 2002. Global distribution of neutrons from Mars: Results from Mars Odyssey. *Science*, 297.5578, 75-78. doi: 10.1126/science.1073541
- Feldman, W. C., Prettyman, T. H., Maurice, S., Plaut, J. J., Bish, D. L., and ten others, 2004a. Global distribution of near-surface hydrogen on Mars. *Journal of Geophysical Research*, 109.E9, E09006. doi: 10.1029/2003JE002160.
- Feldman, W. C., Head, J. W., Maurice, S., Prettyman, T. H., Elphic, R. C., and four others, 2004b. Recharge mechanism of near-equatorial hydrogen on Mars: Atmospheric redistribution or sub-surface aquifer. *Geophysical Research Letters*, 31(18).
- Feldman, W. C., Mellon, M. T., Maurice, S., Prettyman, T. H., Cary, J. W., and nine others, 2004c. Hydrated states of MgSO<sub>4</sub> at equatorial latitudes on Mars. *Geophysical Research Letters*, 31(16).
- Feldman, W. C., Prettyman, T. H., Maurice, S., Nelli, S., Elphic, R., and six others, 2005. Topographic control of hydrogen deposits at low latitudes to midlatitudes of Mars. *Journal of Geophysical Research: Planets*, 110, E11009, doi:10.1029/2005JE002452.
- Feldman, W. C., Bandfield, J. L., Diez, B., Elphic, R. C., Maurice, S., Nelli, S. M., 2008. North to south asymmetries in the water-equivalent hydrogen distribution at high latitudes on Mars. *Journal of Geophysical Research: Planets*, (1991–2012), 113(E8).
- Kadish, S. J., Head, J. W., 2007. Microclimates on the Tharsis Rise and volcanoes: Orographic effects and geological processes. *Lunar and Planetary Science Conference* 38, 1120.
- Lodders, K., 2003. Solar system abundances and condensation temperatures of the elements. *The Astrophysical Journal*, 591(2), 1220.
- Maurice, S., Feldman, W., Diez, B., Gasnault, O., Lawrence, D. J., Pathare, A., Prettyman, T., 2011. Mars Odyssey neutron data: 1. Data processing and models of water-equivalent-hydrogen distribution. *Journal of Geophysical Research*, 116, E11008, doi:10.1029/2011JE003810.

- Milliken, R. E., Bish, D. L., 2010. Sources and sinks of clay minerals on Mars. *Philosophical Magazine*, 90(17-18), 2293-2308.
- Mitrofanov, I., Anfimov, D., Kozyrev, A., Litvak, M., Sanin, A., and seven others, 2002. Maps of subsurface hydrogen from the high energy neutron detector, Mars Odyssey. *Science*, 297, 78-81.
- Parate, H. R., Mohan Kumar, M. S., Descloitres, M., Barbiero, L., Ruiz, L., and three others, 2011. Comparison of electrical resistivity by geophysical method and neutron probe logging for soil moisture monitoring in a forested watershed. *Current Science*, (00113891) 100, 1405-1412.
- Prettyman, T. H., 2006. Remote Chemical Sensing Using Nuclear Spectroscopy. *Encyclopedia of the Solar System*, ed. T. Spohn, et al. San Diego: Academic Press, 775-86
- Rekvelde, M. T., 2000. Novel instrumentation concepts using polarised neutrons. *Physica B: Condensed Matter*, 276, 55-58.
- Schorghofer, N., Forget, F., 2012. History and anatomy of subsurface ice on Mars. *Icarus*, 220, 1112-1120.
- Schultz, P. H., Lutz-Garihan, A. B., 1981. Equatorial paleo-poles on Mars, *Lunar Planetary Science Conference 12*, 946-948.
- Seneta, E., 2013. A Tricentenary history of the Law of Large Numbers. *Bernoulli* 19, no. 4, 1088--1121. doi:10.3150/12-BEJSP12. <http://projecteuclid.org/euclid.bj/1377612845>.
- Smith, D. E., Zuber, M.T., Frey, H.V., Garvin, J.B., Head, J.W., and nineteen others, 2001. Mars Orbiter Laser Altimeter: Experiment summary after the first year of global mapping of Mars. *Journal of Geophysical Research*, 106, 23,689-23,722, doi:10.1029/2000JE001364.
- Squyres, S.W., Knoll, A. H., Arvidson, R. E., Clark, B. C., Grotzinger, J. P., and thirteen others, 2006. Two years at Meridiani Planum: Results from the Opportunity Rover. *Science*, Vol 313, no. 5792, 1403-1407. doi: 10.1126/science.1130890
- Tobler W., 1970. A computer movie simulating urban growth in the Detroit region. *Economic Geography*, 46(2): 234-240.

- Vaniman, D. T., Bish, D. L., Chipera, S. J., Fialips, C. I., Carey, J. W., Feldman, W. C., 2004. Magnesium sulphate salts and the history of water on Mars. *Nature*, 431(7009), 663-665.
- Vienken, T., Reboulet, E., Leven, C., Kreck, M., Zschomack, L., Dietrich, P., 2013. Field comparison of selected methods for vertical soil water content profiling. *Journal of Hydrology*, 501, 205-212.
- Wu, H., Skripov, A. V., Udovic, T. J., Rush, J. J., Derakhshan, S., Kleinke, H., 2010. Hydrogen in Ti<sub>3</sub>Sb and Ti<sub>2</sub>Sb: Neutron vibrational spectroscopy and neutron diffraction studies. *Journal of Alloys and Compounds*, 496, 1-6.
- Zuber, M.T., Smith, D. E., Solomon, S. C., Muhleman, D. O., Head, J. W., and three others, 1992. The Mars Observer Laser Altimeter investigation. *Journal of Geophysical Research*, 97, 7781-7798.

## **Chapter 2: Seasonal investigation of water-equivalent hydrogen variability in the eastern equatorial region of Mars**

### **Abstract**

Data from the Mars Odyssey Neutron Spectrometer excels at detecting hydrogen within the upper meter of the martian regolith. Due to the size of the instrument's footprint and the stochastic nature of the epithermal neutrons, MONS counts multiple passes over a location must be combined to calculate a statistically significant measure of central tendency. By 2006, sufficient measurements had been collected to create maps with pixels smaller than 1 km with high confidence, although probabilities associated with the instrument footprint and the normal distribution of the count data preclude analyzing features smaller than ~250 km. Seasonal investigations, however, required dividing the data, lowering the number of records per season such that any calculations were statistically questionable. Four more martian years have passed and MONS has remained viable throughout. This study examines MONS data from 2002 -2012 to assess whether the quantity of records is adequate to begin exploring seasonal changes in the spatial distribution of hydrogen, to understand what seasonal processes unrelated to changes in hydrogen may interfere with the analysis, and to survey the analytical tools available to tease out any true changes from artifacts of Mars' orbital eccentricities.

### **1. Introduction**

#### ***1.1 Martian Seasons***

Due to its increased axial tilt compared to the Earth and the highly elliptical orbit, Mars experiences more extreme seasons than those on our own planet. Unlike Earth, Mars' months and seasons vary



greatly in length. The northern hemisphere experiences longer months in the spring and early summer when the planet is farthest from the sun. Southern summers are shorter and hotter, with the planet at perihelion. These differences create seasonal changes that can be observed from Earth with a 100-150 mm telescope. Differential heating of the southern hemisphere during its summer generates dust storms that can vary from several localized disruptions to a single globe-obscuring haboob. Seasonal changes in the polar caps have been documented since William Herschel's work in the 18<sup>th</sup> century. Astronomers today continue to record the appearance of seasonal clouds, hazes, fogs, and frost.

### ***1.2 Mars Odyssey Neutron Spectrometer***

Planetary missions have extended our ability to detect seasonal processes on Mars. Atmospheric pressure at the Viking 1 lander site fluctuated from 6.9 mb during early northern summer to 8.9 mb just after perihelion (Sharman & Ryan, 1980). More recently, the Phoenix lander observed snow falling from cirrus clouds (Whiteway, et al., 2009). Orbiting satellites contribute to our understanding of seasonal changes on Mars at both the global and local scale, but not all instruments are designed to detect seasonality.

The Mars Odyssey Neutron Spectrometer (MONS; Feldman et al., 2002) has been operating aboard Mars Odyssey since 2002. Designed for cumulative aggregation of detected neutron collisions, the mean of the count rates observed over a sampled area is used as a proxy for hydrogen abundance, and hence a potential signature for H<sub>2</sub>O. The neutron counts in a single record are the total number of neutrons colliding with the detector in a 19.7 second interval. The count rate is the calculated average collisions per second with the neutron spectrometer. Epithermal neutrons, those with an energy level between 0.3 eV to 700 keV (Maurice et al., 2011), have an affinity for hydrogen atoms such that a lowered rate of neutron collisions with the MONS detector correlates with hydrogen

enrichment in the upper meter of martian regolith. When these neutrally charged particles encounter hydrogen, they lose energy, slowing or stopping completely within the ground. Where hydrogen is less abundant in the regolith, a larger percentage of epithermal neutrons exit the subsurface and escape the thin atmosphere, beyond which they can be detected by the orbiting MONS instrument. The mean hydrogen abundance within the footprint of the MONS, calculated here as Water Equivalent Hydrogen (in units of weight percent), is therefore inversely (and exponentially) related to the neutron count rate (Fig. 1).

In this study I hypothesize that seasonal changes may be apparent in the MONS data and that, by tracking the changes over the course of a martian year, these changes can be traced to variations in insolation with respect to large-scale, regional geomorphic features.

### ***1.3 Statistical Confidence***

As a result of the stochastic nature of neutron detection, a single count interval is not a reliable predictor of the neutron count rate at a location. Additionally, the footprint of the instrument, the area on the ground from which a detected neutron could have originated, can be well modeled by a two-dimensional (2-D) Gaussian function. The resolution of the instrument has been determined to approximate 550 km at the surface (Teodoro et al., 2010). Other methods have been used to increase the confidence in counts over a given area (Feldman et al., 2008; Teodoro et al., 2011), but the underlying principle hinges on collecting the greatest number of count records possible for the area in question. This does not change the probabilities associated with the huge instrument footprint or the normal distribution of the neutron measurements, but it does affect the only probability component that can be modified after the measurements have been taken. Drawing upon the Weak Law of Large Numbers (Bernoulli, 1713), an increase in confidence is obtained as the number of samples pulled from a population increases, reflecting an increased likelihood that

the average value of the samples is approaching the average value of the population (Fig. 2). Calculations based on sample sizes  $> 80$  result in a 95% certainty that the sample mean is within half a standard deviation of the population mean. This confidence rises asymptotically with increased sample size such that a sample with 400 records imparts a confidence level of 99%, but the rate at which the confidence level increases per sample is reduced above this. For this reason, a goal of 400 samples an appropriate threshold for statistical vigor. There is no method that will allow us to detect every neutron that escapes the martian surface, but the longevity of the Mars Odyssey mission has allowed MONS to accumulate an impressive number of measurements.

#### ***1.4 Eastern Equatorial Mars***

The study area is centered on Schiaparelli Basin, around which the blues and purples in the WEH map (Fig. 3) indicate hydrogen enrichment in the surrounding terrain (Feldman et al., 2002). This area of Mars is unusual for a number of reasons. The cratered highlands of Noachis Terra and Terra Sabaea form a regional NE-SW trending topographic rise between Hellas Basin and Arabia Terra. Although north of the dichotomy boundary and therefore officially part of the cratered highlands, the geomorphology of Arabia Terra is subdued and includes the remarkably smooth Meridiani Planum. The northern boundary of the study area is the reworked northern lowland regions of Chryse and Acidalia Planitia. On the western edge, the chaos and outflow channels of Margaritifer Terra divide the study area from the Tharsis volcanic provinces and Valles Marineris. The area is bounded by the 60° E line of longitude and Hellas form the eastern limit.

The region straddles the equator and the aeroid (martian sea level), imparting both a band of relatively warm temperatures and a seasonal range of atmospheric pressure. Albedo characteristics and changes in dust affect the way surfaces and the atmosphere above them absorb and release heat.

Signs of past water flow include dendritic valley channels that form in the highlands and terminate within Arabia Terra. Straighter valleys with shorter tributaries once drained the northern extent of Arabia Terra into the northern plains. Huge outflow channels once moved water into Chryse from as far south as Argyre Planitia, over 3600 km away. Under a more temperate climate regime, this region on Mars would have been seasonally active with varying precipitation, seasonal flooding, and desiccation as playas and impounded lakes dried up.

### ***1.5 Seasonal Investigation***

Seasonal investigations on Mars frequently focus on changes in the atmosphere (Jakosky and Farmer, 1982; Novak et al., 2002) or climate modeling of seasonal changes in the water cycle (Richardson and Wilson, 2002; Jakosky, 1983; Montmessin et al., 2004). Few seasonal neutron surveys have been completed. When studies are undertaken, the limited number of neutron records and the large size of the instrument footprint have required the data be averaged into 10° bands of latitude (Kuzmin et al., 2007) or to undergo smoothing after averaging the records into 0.5° bins to fill in regions with missing data (Prettyman et al., 2009).

In this study I explore the epithermal neutron records for seasonal variation by employing resampling of data over an area with a moving boxcar function. Similarly, limitations will be placed on the decrease in the number of records available for each season through the use of a moving average for the time series. With both spatial and temporal resampling, each of the 12 monthly records should contain sufficient data to produce a statistically robust map. Frequency tables and change detection charts (Weng, 2002) are then created, as well as statistical and algebraic approaches, in an attempt to detect seasonality in the neutron count signal. This combination of spatial and temporal resampling is novel with respect to planetary applications. Likewise, seasonal

assessment of changes in neutron count rates has not yet been performed with such spatial resolution on Mars.

## 2. Terminology

Foremost, seasonality needs to be defined with respect to MONS data. Unlike the terrestrial sense of a hemispheric progression from coldest to warmest relative temperatures, our study aims to determine whether there is a progressive change from relative low levels of water equivalent hydrogen to higher abundances within the footprint of the instrument in response to seasonal changes in insolation or other atmospheric factors. Research focusing on diurnal changes, fog, and adsorption may slowly change the way we think of the martian water cycle, but for this study, the focus is on the detection of changes in abundance using epithermal neutron counts as a proxy for changes in near-surface regolith H<sub>2</sub>O abundance, and the characterization of broad locations where such changes occur. Terminology used in this study is as follows:

**Count record** – a single point of epithermal neutron data, which stores the count (the number of) collisions detected during the 19.7 second recording phase of each 20 second cycle of MONS. Spatially, this corresponds to a point on the map centered on the instrument's footprint at the halfway point of the recording phase.

**Point data** – A collective term for the body of epithermal neutron count records or a subset of these.

**Window** – The area encompassing the data to be processed, also called a neighborhood.

**Nodes, Cells, and Pixels** – conceptually these are similar. Nodes are the centers of the calculations the windows are based on. The spacing between the nodes defines the size of the cell in the resulting map raster and the cell becomes the pixel.

**Ls** – Also referred to as  $L_s$  or  $L_{sub s}$ , Ls is the measurement of the angle between Mars' position with respect to the sun at  $0^\circ$  Ls (spring equinox in the northern hemisphere) and the current position in orbit around the sun. As on Earth,  $90^\circ$  and  $270^\circ$  Ls correspond to the solstices and  $180^\circ$  Ls to the northern fall equinox.

**Month** – one of 12 groups of  $30^\circ$  Ls. Unlike terrestrial months, months on Mars range from 46 to almost 67 sols long. Martian years are 668.6 sols long, roughly two terrestrial years.

**Temporal slice** – (or slice) point data from the two martian months to either side of an Ls of interest. This term will also refer to the resulting raster map of neutron count rates in units of water-equivalent hydrogen calculated from this data.

**Time series** – a collection of well-defined measurements taken at repeated, regular intervals. This investigation uses the flow series type, which is a series measuring an activity (the counts on each record) over a given time (the temporal slice). The data is then averaged to obtain a value for a shorter time span within the interval. The point data in each slice are summed, divided by the number of records, then divided by 19.7 seconds to acquire the count rate.

### **3. Methods**

Here I identify the algorithms used to process the point data and to attempt to identify seasonality in the resulting neutron count rate maps.

#### ***3.1 Epithermal Neutron Records***

The point data from MONS reflect the number of epithermal neutrons that collided with the detector over the 19.7 second recording period. The initial dataset used in this study contains 1,330,350 epithermal neutron count records accumulated over the course of about 5 martian years (from 2002 to 2012). Rather than dividing the data into intervals of  $30^\circ$  Ls across multiple years, the

creation of aggregate months provided seasonal data while maintaining a larger number of records within each interval. Aggregation can integrate anomalous events that may be related to seasonality, but not to the hydrogen signal. For example, consider a common southern hemisphere summer event, dust storms. Note that epithermal neutron data could be contaminated by data from orbits containing measurements taken during dust storms. Such events could prevent epithermal neutrons from reaching the detector on the satellite, creating an unusually high hydrogen signal overprint in a footprint area that normally exhibits moderate to low abundances. This caveat aside, a seasonal aggregate increases the statistical likelihood that the sample's measure of central tendency approaches the true measure for that location at that time of the year.

### ***3.2 Time Series***

Time series created from stochastic (randomly occurring, unpredictable) events (e.g., traffic patterns, rainfall, neutron collisions) normally contain considerable noise due to the chaotic nature of the recorded data. To minimize this noise, it is customary to take a moving average centered on the time period of interest that includes records from before and after the period of interest. For example, when creating a time series for an event that happens daily over several weeks, it would be appropriate to incorporate the 3 days preceding and following the day of interest. Rather than 12 months of interest, the study focuses on the 12 Ls dividing them. I have selected both equinoxes, both solstices, and the eight other increments of  $30^\circ$  Ls. For each Ls position selected, the two months to either side are included in the temporal slice (Fig. 4). Four total flanking months were selected using the justification that only two months might not contain enough records for statistical confidence, whereas six would incorporate data too far (temporally) from the chosen Ls that could significantly mask seasonal effects on the neutron count rates.

### ***3.3 Neighborhood Point Statistics***

For each temporal slice, the point data from the 2 months on either side of the  $L_s$  value of interest were plotted in ArcMap. A neighborhood (focal) point statistics function, which summarizes the values of points within a defined area (neighborhood), starts at a node, calculates a statistic for all the point data in the window area, stores that value in the cell that becomes the pixel on the map, then moves to the adjacent node and repeats the process. Here the neighborhood is the sampling window and the cell is the node. Two rasters were created for each temporal slice: one totaled the number of records in each window and the other calculated the mean of the counts in those records. This resampling of points in overlapping windows allows the sample size to remain robust at each node. If binning had been used instead of a moving window, each point/record could only be incorporated into the statistic for a single node/cell/pixel because the size of the cell would match the (square) bin/neighborhood/sampling window. For this investigation, the node spacing (and hence cell/pixel size in the raster) is set to 463 m, specifically to correspond to the cell size of the Mars Orbital Laser Altimeter (MOLA) elevation data, with a 100 km radius sampling window/neighborhood. This size is larger than strictly necessary, as a 66.6 km radius window best matches the sampling area size in the commonly-used square (Feldman et al., 2002) and occasional rectangular (Tokar et al., 2002) bins. However, as I have divided up the full set of point data, the slightly larger size incorporates more points than the smaller-radius window. As noted, an increased sample size improves the statistical confidence in the resulting mean, with the trade-off that the larger window causes some smoothing of the data associated with each node by incorporating more distant data into the calculation. Again, due to the footprint, the concentration is on regional features.



The total mean epithermal neutron count rasters are converted first to mean epithermal count rates (MENCR) by dividing by 19.7 s, then to WEH using the equation (Elphic, Rick. "Relating epi count rate to H<sub>2</sub>O abundance." Message to the author. Aug. 2005. Email.; Prettyman, Thomas. "Power law relationship between WEH and neutron counts for a homogenous, single layer." Message to the author. Sept. 30, 2014. Email.):

$$Wt\%WEH = 100 * \left( \frac{[29.306 / \langle MENCR - 1 \rangle]}{29.099} \right)^{1.3275} \quad (1)$$

### **3.4 Change Detection**

Change detection calculations can be as simple as subtracting the cell values of one raster from the corresponding cells on another to more elaborate analyses. Many require converting continuous data (e.g., rainfall, epithermal neutron count rates, WEH) into discrete classes (e.g., defining ranges, or rounding to integers) before performing calculations.

#### **3.4.1 Differences**

Simple subtraction, where the more recent raster is subtracted from a preceding one, provides both a quick spatial visualization of change from the old to the new and a quantitative record of the direction of change. Negative values indicate neutron count rates are decreasing with the passage of time. If a cell contained 12 wt.% WEH one season and the following season the same cell recorded a WEH value of 13 wt.%, the output record would contain -1 for that cell. Positive values indicate the following season has a higher neutron count rate (i.e., the WEH value of the initial season was higher than the season afterward). Differences between temporal slices can be evaluated visually, by histogram spread, and by the mean of raster values. Visually examining the

difference raster can be valuable where there is a clear predominance of positive or negative values.

The spread of values on the output raster's histogram helps clarify the difference between sets where visual clues are not straightforward. The histogram indicates more than the distribution of raster cell values and the count of negative and positive cells. The shape of the histogram; whether the data is bimodal, skewed, dispersed, or has a tight or flat peak, reveals more about the data than can be observed looking at the raster itself. The mean of the entire raster can be used as a broad indicator of whether the overall map area is moving into a higher or lower hydrogen abundance state.

### **3.4.2 Class Frequency**

Changes in hydrogen concentration from one temporal slice raster to the next can be quantified where continuous data is converted to discrete values through reclassification. Values in the temporal slice raster are stored as continuous units of weight percent of water-equivalent hydrogen. A threshold of 1 wt. % WEH was selected for the class width and the WEH continuous data values were reclassified to integer values. A simple count was then taken of the number of cells in each raster for each of the 14 WEH classes (5 to 18 wt.%). Displaying this frequency information in a table (WEH classes along the x-axis and the 12 temporal slices listed chronologically along the Y axis) creates a visual and quantitative record of change in WEH values over time.

### **3.4.3 Algebraic Change Matrix**

Similarly, a change matrix, based on those used for terrestrial land cover and land use studies (Weng, 2002), can be created from two rasters (where the data has been grouped into discrete classes) using a *Combinatorial Or* logic algorithm. *Combinatorial Or*, a function within ArcMap's

Spatial Analyst toolbox, spatially compares two rasters on a cell by cell basis, counting the frequency with which each combination of classes occurs. By arranging the class headings into a matrix, with the preceding season (or initial state) along the y-axis and those of the following season along the x-axis, a grid is created to store the *Combinatorial Or* output (Fig. 5).

This change matrix calculates change between two WEH rasters by showing how individual locations on the map (pixels) change in neutron count rates from one point in time to another. If the local neutron count rate (the range of wt.% WEH the pixel falls in) does not change (or does not vary enough to change WEH classes), then the pixel will be counted as being in the same class in both rasters (Fig. 5, diagonal row of gray cells). When a location's neutron count rate changes, the pixel is recorded in the cell where the old and new classes intersect.

In this manner the matrix tracks the movement of pixels from one class in the first data raster (Fig. 5, class 6, green) to different classes in the second raster (Fig. 5, classes 5-7, blue). The cells within the row show the distribution of raster 1, class 6 pixels across the classes (as labeled in the column headings) of the second raster. The row total for class 6 is the total count (frequency) of class six pixels in the first raster. The column total for class 6 is the number of class six pixels in the second raster. By subtracting the row total for a class in the first raster from the column total for that same class in the second raster the change in frequency can be found. The 20814 more class 6 pixels in the second raster indicates a 0.23% increase in class 6 pixels from the first raster to the second. These calculations may be displayed with the matrix or the results from several related change matrices may be combined into a table for reference.

A magnitude table (Fig. 5b) simplifies the results by condensing the frequency value in each cell with the number of digits in the value (e.g., 47265 becomes 5, 652 becomes 3). This matrix is based

on the same data and is analyzed within the matrix in the same way, but the magnitude of change is more readily apparent.

### ***3.5 Statistical Analysis***

Examining all 12 Ls rasters as a set allows us to create a new raster for any statistic of interest (e.g., minimum, maximum) where the value in a given cell represents that statistic as calculated using the values of all twelve rasters at that cell location. Localities where the neutron count rate varies between the seasons can be observed by examining cells where the range and standard deviation are the greatest. Similarly, areas with the smallest range or standard deviation represent areas with little change over the seasons. Variations that might indicate seasonally cyclical changes can then be examined in relationship to regional geomorphology to search for indications of potential surface processes that could be driving the changes. For example, hydrogen levels changing within a large crater basin might point to a seasonal hydrogen sink, either from atmospheric deposition, such as fog or frost, or from mobilized brines when temperature and pressure permitted a liquid phase.

## **4. Results**

### ***4.1 Sample size***

Window size matters when the sample size is reduced to a fraction of the full set of point data for seasonal investigations. This study combined 120° of Ls for each temporal slice, reducing the data by a third (approximately, see section 5.1).

The number of records included at a node is also adversely impacted by proximity to the map border. The count rasters displaying the number (n) of point data records included in each cell indicate that for the 100 km radius sampling window on these temporal slices, any neutron count

values within 100 km of the edge are less statistically robust due to the nodes having less than a full window to gather data points. Depending on the number of points gathered, the confidence in the sample may be unacceptably low. For the four main temporal slices (Fig. 6), the interior confidence is 98% or higher, with all but the 270° Ls slice having more than 400 counts for every cell in the interior. This result means that for all areas except within 100 km of the borders, we can be at least 98% certain that the mean epithermal count rate calculated for those cells is within half a standard deviation of the true value for that cell's location at that time of year.

## **4.2 Change detection**

The four slices with the most extreme changes can be seen in the difference rasters for each pair of adjacent temporal slices ( $A-B = \Delta_{WEH}$ ) and in the 12 slice frequency table. These four, the equinoxes (0° and 270° Ls) and solstices (90° and 180° Ls), became the targets for the algebraic change detection.

### **4.2.1 Differences**

By subtracting the WEH raster of the later of each pair of adjacent temporal slices from the previous raster, 12 new rasters highlighted changes between each pair. Plotting the highest and lowest values from each of the 12 difference rasters onto a radar chart reveals a progressive trend toward higher values at each hemisphere's summer (Fig. 7). For the southern summer, 300° Ls (a month after the solstice) shows the greatest positive change. Northern summer's largest positive difference is at summer solstice (90°), but the next two Ls periods on the radar chart (120° and 150° Ls) are nearly as high, giving the aphelion (71° Ls) side of the chart a flattened appearance.

### **4.2.2 Class Frequency**

The frequency chart (Fig. 8) shows the total number of cells (pixels) in each WEH class (column 1, class 5 = 5 wt.% water-equivalent hydrogen; column 2, class 6 = 6 wt. % WEH, etc.) for each of the

12 temporal slices. The WEH class values for temporal slices for 240° and 270° Ls shift to the right (meaning that high WEH classes exist during these portions of the martian year that are non-existent during other parts of the year), as do 60° and 90° to a lesser extent (Fig. 8, green). Conversely, 0°, 30° and 330° Ls (and 150° and 180° Ls, to a lesser extent) class values shift to the left (Fig. 8, blue). The class values for the intervening rasters smoothly bridge the values, with 120°, 210°, and 300° falling somewhere between the extremes to either side of them. These shifts in location indicate there is a seasonal ebb and flow of neutron count rates as the year progresses. The two pairs of right-shifted slices correspond to the solstices, with the weaker pair coinciding with aphelion (71° Ls, directly between 60° and 90° Ls, summer in the northern hemisphere). Likewise, perihelion (251° Ls) falls between the pair of slices with the strongest shift to the right. The slice pair that is shifted the most to the left (0° and 30° Ls), corresponds to early spring in the northern hemisphere. The remaining pair, 150° and 180°, correspond to late winter in the southern hemisphere, indicating that any processes at work during northern early spring tend to become active earlier in the southern hemisphere.

#### 4.2.3 Algebraic Change Matrices

Based on data from the count chart, the solstice- and equinox-based temporal slices (0°, 90°, 180°, and 270° Ls) were selected for analysis using change matrices. The simplified charts (e.g., Fig. 9) display the cell frequency magnitude; that is, the cell count has been reduced to an integer value representing the number of digits in the change matrix cell (refer to section 3.4.3).

The first change matrix of the set (Fig. 9) compares the temporal slices closest to aphelion and perihelion (solstice slices 90° and 270°, respectively) and shows a distinct modification in processes above 10 wt. % WEH. There is a tendency for some of the cells/pixels in low WEH classes at

aphelion (slice  $90^\circ$  Ls) to move into higher WEH classes at perihelion ( $270^\circ$  Ls), but a few cells (hundreds to tens of thousands) end up in lower classes. Above 10 wt.% that pattern changes to a regime where aphelion cells rarely end up in lower WEH classes during perihelion. Additionally, rather than increasing by a single WEH class or possibly two, millions of cells move, some migrating as many as four classes higher.

The differences between the equinoxes are less dramatic (Fig. 10). With respect to the northern hemisphere, going from the spring ( $0^\circ$  Ls) to the autumnal equinox ( $180^\circ$  Ls), cells/pixels in WEH classes below 10 wt. % are almost as likely to shift to lower WEH classes as higher ones. Above 10 wt.%, there is a very slight preference for cells to move to higher classes, but millions of cells still move to lower values. This changes (again, slightly) at 15 wt. % with fewer than a hundred cells moving up into the 16 wt.% class but more than a hundred thousand dropping a class.

Four additional change matrices were created to see how cells moved from each of the 4 slices (solstices and equinoxes) chronologically (read in a clockwise sense in Fig. 11). Starting with northern spring ( $0^\circ$ ) moving into northern summer ( $90^\circ$ ), the lack of any cells/pixels in the highest WEH indicates that neither of these times have particularly low count rates (Fig. 11a), although cells from WEH classes 14 and 15 in spring do move into summer's 16 wt.% class. Below 10 wt.%, pixels are almost as likely to move to a lower class whereas above this class, there is a stronger tendency for pixels to migrate to higher WEH classes.

During the change from northern summer to northern autumn or southern spring (Fig. 11b,  $90^\circ$  to  $180^\circ$  Ls), a similar pattern occurs for the low WEH classes, but there is a marked migration of Ls  $90^\circ$  pixels from higher values to lower ones in Ls  $180^\circ$ . The transition from southern spring to southern summer (Fig. 11c) provides visual agreement that the  $270^\circ$  Ls temporal slice contains the highest number of cells/pixel within the highest WEH classes. Whereas the transition from northern spring

to northern summer (Fig. 11a) contained pixels moving into WEH classes two higher, southern summer shows that cells in slice 180° classes 10 and higher may stay in the same class, never move to lower classes, and commonly move 3 classes higher.

The move from southern summer (270°) into southern autumn or northern spring (0°) shows a similarly dramatic change as pixels that had belonged to WEH classes 16, 17, and 18 fall into classes 12-14. Except for the 5 wt.% class, cells moving from 270° to 0° only stay in the original class or drop a class.

Overall, in both hemispheres, as Mars moves along its orbit from spring into summer, cells move into higher WEH classes (Fig. 11). The hemispheres differ in that southern summers display an across the board increase in hydrogen abundance while northern summers always have cells in each class that came from higher classes in the 0° slice or move into higher classes in the 90° Ls slice.

The percent change from one season to the next is highest in the highest WEH classes (Fig. 12). The high percentage relates directly to the shifts in cell counts noted in Fig. 11c. While there are changes >50% in the 9 to 14 wt. % class, they are related to perihelion (251° Ls) alone. Areas in the chart with ND indicate classes in which the initial temporal slice had no cells. Most notable in this chart is the shifting of cells out of the 9 wt. % WEH class as the season changes from southern spring to southern summer (180° to 270° Ls). No other season undergoes such a significant decrease in the central band of classes (6-13 wt.%).

#### ***4.3 Statistical Analysis***

A cursory examination of the 12 temporal slices shows that the changes from one to the next are regular and rhythmic (Fig. 13), having two points of increase and two of decrease per year. A steady increase in either hemisphere from spring equinox to the summer solstice creates a flattened oval



on the radar chart. Southern summer coincides with perihelion and is reflected by higher WEH values than at aphelion in the northern summer. The study area straddles the equator, extending for 45° of latitude in either direction, so both summers influence the center of the region of interest.

While the plot of maximum and minimum values on the radar chart appears to suggest there is a strong seasonality with hydrogen abundance peaking at perihelion, it must be remembered that this is also the height of dust storm season. As noted previously, an extensive dust storm could block epithermal neutrons from reaching the orbiter's detector, which would create a falsely low count rate. Due to the inverse relationship between count rate and hydrogen, a suppressed count would manifest as an elevated hydrogen signature. Seasonal storms could possibly create a false seasonal signal, but if seasonal storms were responsible, we might expect increases in WEH to be concentrated in the areas known to be frequently involved in dust storm and dust devil activity. To constrain this possibility, I examined the 12 slices as a set to determine the annual standard deviation between slices on a cell-by-cell basis (Fig. 14). The resulting map depicts very little change (<0.4 wt.% WEH) around the edges of the study area, including Hellas Basin and Ares Vallis. The largest variability (0.8– 1.33 wt.%) occurs in the center of the mapping area, with the localities between 0 and 1500 m in elevation (Fig. 3b, tan to gold) showing the most continuous pixels in that range. This would indicate that the bulk of the change occurring in the radar charts is located along the edges for the minimum values, while the variation in the maxima are due to changes around Schiaparelli.

Dust storms can occur at any time during the year, they are most common and most widespread from 180° to 0° Ls; hence, fewer of them in the remaining portion of the year would be expected to appear as variability in the regions where storms were most prevalent. If seasonal changes were

due to dust storms interfering with epithermal neutrons reaching the detector, we might expect higher variation and WEH values in the southeast corner, as Hellas Basin is a common generation point for dust storms. This corner of the map is particularly stable, as mentioned previously. It is unlikely that any of the variability seen in Figure 14 is due to dust storms.

## **5. Discussion**

### ***5.1 Static Signal***

There are regions where some cells remained in the same WEH classes throughout the martian year, but there are caveats (Fig. 15). The red areas indicate which cells/pixels on the map were static with respect to WEH class. They are located along the periphery of the map and arranged in concentric bands. Although these locations show the least variability in the region, they only manifest as bands because they have been grouped into classes (they are no longer continuous data). The bands represent pixels that remain in the same class throughout the year, but it is highly doubtful that a given pixel would retain precisely the same WEH value over the course of a year. In general, the areas between the bands also shifted very little, but the changes in those cells were just enough to push them out of one class and into another for at least a portion of the year.

### ***5.2 Mars Orbital Mechanics***

Another consideration in the interpretation of the epithermal neutron record is the nature of the martian year itself. As noted, the number of sols per month increases as the planet approaches aphelion. Dividing the year into twelve equal slices of  $30^\circ$  Ls, therefore, does not produce 12 months with an equal number of sols. For the 4 months used in the temporal slice for  $270^\circ$  Ls, southern summer solstice, there are 191 sols. The slice for  $90^\circ$  Ls has 256 sols. The difference of 65 sols is longer than all but two of the martian months. If the unequal number of days per slice had a strong influence on the WEH measurements, one might expect to see the decreases in neutron

counts relatively equally across the mapping area; however, the outer border changes very little over the course of the year (Fig. 15). Additionally, the decreases in neutron count rates would be expected to influence all of the WEH classes, but section 4.2.3 shows a distinct difference between the classes below 10 wt.% WEH and those above 10 wt. % WEH for all temporal slices. I conclude that the 12 temporal slices used in this analysis provide a realistic characterization of seasonal variability. Designing a time series to serve as a check against artifacts created by extra sols in the longer months would require dividing the 668.6 sol martian year by ten or twenty and have 66.86 or 33.45 sol divisions, respectively. Another method would be to make the divisions 66 or 33 sols and center the extra 8.5 sols in between two preceding and two following divisions for a moving average.

### ***5.3 Locations of Interest***

By far the most seasonally active localities are those at the center of the mapping area and locations where the topography changes from northern lowlands or smoother areas of northern Arabia to the higher elevations and rougher topography of the southern highlands (Figs. 16, 17). Most of these areas display evidence of valley networks (Fig. 3) that were likely active drainages for a significant period of time during a wetter past. Craters in the high variability areas frequently have central features resembling pingos or spring mounds, both of which imply subsurface liquids. Some craters in the vicinity have ejecta aprons, which may indicate the impactor struck where the regolith had subsurface ice or water.

Figures 16 and 17 show the solstice and equinox slices at the full data extent (Fig. 16) and zoomed in on the seasonally most active regions (Fig. 17). The wider view shows a smaller cluster of >17 wt.% pixels in the center of the image at 0° and 180° Ls (northern spring and autumn equinoxes, respectively), although both show abundances above 14 wt.% as far east as Tikhonravov. Between

the two, northern spring ( $0^\circ$  Ls) has the smallest aerial extent of  $>12$  wt.% WEH. The northern hemisphere is just coming out of its coldest period. South of the equator, summer has ended; but due to topography, summer insolation warms the southern hemisphere unequally. As the top of the regional topographic high (Fig. 3b, white, running from Le Verrier to Huygens) splits the study area into north- and south-facing slopes, the southern hemisphere's summer sun has a higher angle of incidence on the southern slope. This means the north-facing slope, including the southern lobe of the hydrogen signal, experiences less summer insolation. By southern autumn equinox ( $0^\circ$  Ls), little of the thermal energy received from this diffuse solar radiation remains.

Compare this to the northern autumn equinox ( $180^\circ$  Ls) where the topography north of the equator slopes to the north. Because the angle of incidence is closer to  $90^\circ$  than it would be on a flat or south-facing slope, insolation is more direct. Even though southern summer has ended, the southern lobe of the hydrogen signal is still receiving insolation and patches of  $>12$  wt.% WEH extend into the lower elevations.

The solstices themselves, northern summer and winter ( $90^\circ$  and  $270^\circ$  Ls), display the widest extents and greatest percentages of WEH. Northern summer ( $90^\circ$  Ls) extends for the greater number of sols, so insolation occurs both over a longer amount of time and, due to the southern slope, a larger area. This has multiple effects: warmer daytime temperatures increase the likelihood of diurnal precipitation from fogs, dew, and frost; liquid flow of waters and brines are briefly possible on frost-free days; and true evaporation (rather than sublimation) becomes possible as well. During  $90^\circ$  Ls areas south of the equator, although technically in winter, benefit from increased insolation on the south-facing slope resulting in WEH values  $>17$  wt.% in the highlands south and east of Schiaparelli. North of the equator, the summer insolation causes increases in  $>12$  wt.% WEH far to the north and east compared to the equinoxes.

Southern summer's (270° Ls) pattern is unlike any of the others. While south of the equator experiences a brief summer, it is mainly the top of the topographic rise, where the south- and north-facing slopes meet, that receives the most direct insolation. Warming of the ground at the top of the slope would create a void that pulls cold air from the northern hemisphere up the slope. North of the equator, the short, relatively mild (by martian standards) winter provides parcels of air from the low northern plains and north polar cap that, although thin with a low carrying capacity for moisture, are frequently close to saturation. The orographic lifting created by the movement of these parcels up the slope as the atmosphere seeks equilibrium, allows the parcels to cool to the dew point, creating clouds – often in the form of ground hugging fogs. As seen in the closer views, the peaks and adjacent plains are where the signal is the strongest (Fig. 17).

Note that 270° Ls displays some artifacts related to the smaller sample size (shorter months) in the form of horizontal lineations (Fig. 17). The lines in the image are from the spacing inherent in the data points, which are clustered halfway between the integer longitude values. This spacing creates bands of lower sample sizes, which in turn create bands of higher variability in the data (as discussed in 1.3). Were the density of data at the integer longitude values to match the areas between them, the thick lines would vanish and the overall WEH for the season would be slightly lower. The extent would not change however. It is important to point out that the same spacing pattern exists in the other seasons, but the greater number of days per season increases the number of sampling points, enough of which fall close to the integer lines.

#### ***5.4 Seasonal Changes and Their Potential Causes***

If there had been no indication of seasonal changes within the neutron count rates, it would likely reflect that hydrogen in the upper meter of the martian regolith is locked in minerals; a static quantity changing only over geologic timescales and undetectable with current instruments or

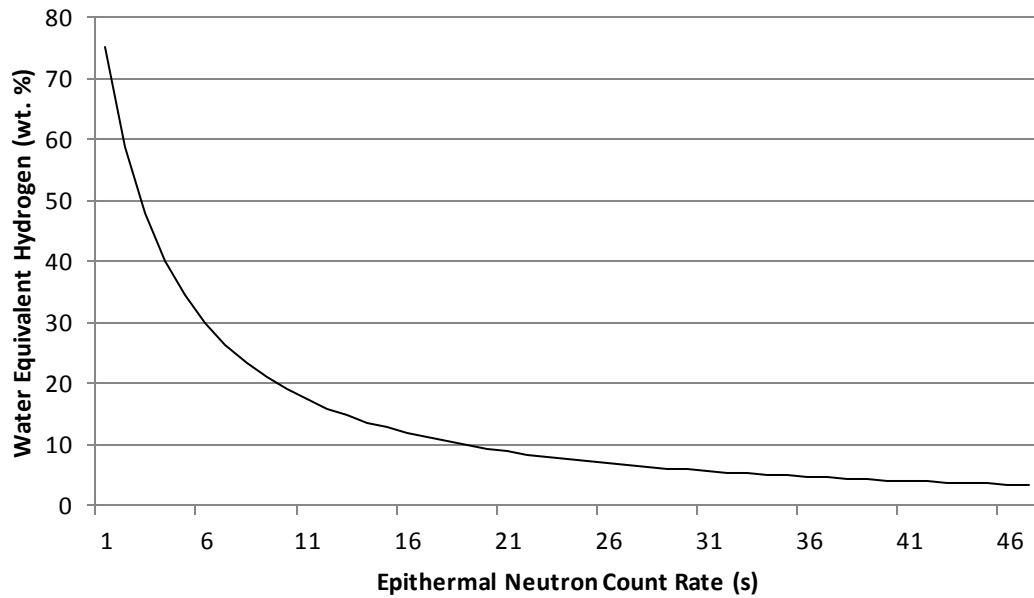
within our short lifespans. Moreover, if the entire map area of Arabia Terra had shown identical variability rather than the periphery being closer to static and the interior more dynamic, it would have provided a strong case for perceived seasonality due to orbital mechanics or seasonal dust activity. However, bimodal changes in the variability of mean hydrogen in the map area suggest there is an active agent forcing seasonal changes in the hydrogen signal that is spatially and temporally variable. The static edges change very little, while the interior of the map appears to ebb and flow rhythmically toward and away from the center point over time. This points to processes occurring in the map's middle, away from the edges. This central region is remarkable for its positioning as a boundary between light and dark albedo, dusty and dust-free surfaces, and between craggy and smoother geomorphology. It also creates the broad regional topographic high that separates the southern highlands and Hellas Basin from the lower plains of Arabia that transition to the smooth, resurfaced northern lowlands more gradually than any other location along the dichotomy boundary. Adiabatic cooling processes may be responsible for depositing fogs, frost, and rare precipitation on the northwest-facing slope of this rise. Changes in barometric pressure throughout the year may also allow subsurface brines to seep from layered deposits and creep downslope, depositing minerals and moisture cyclically. Brief respites in the frigid temperatures may allow springs with heads above the aeroid to add mass to the structures resembling spring mounds and pingos that dot the centers of craters in the region a kilometer lower in elevation.

## **6. Conclusions**

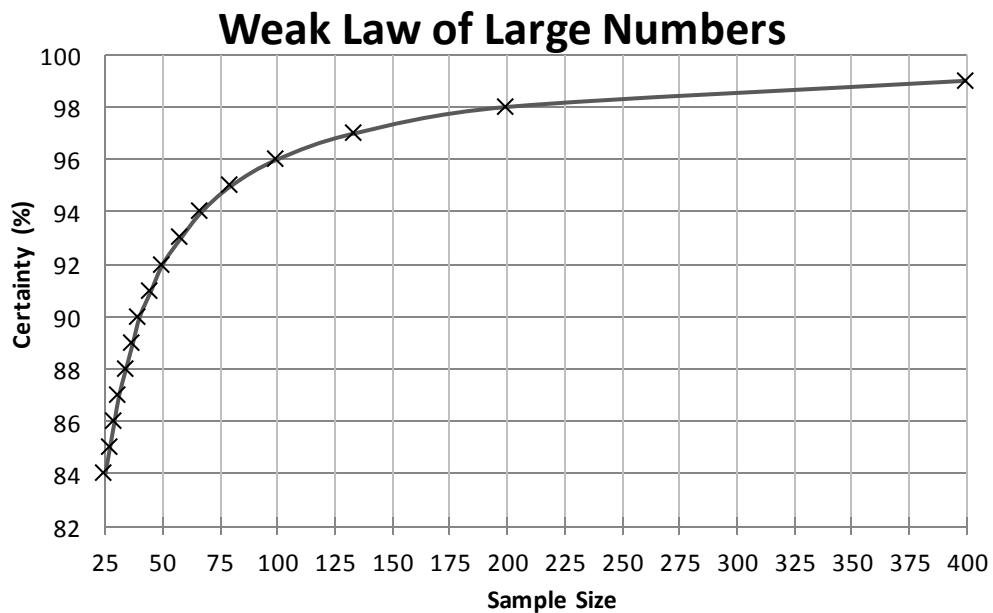
Previously the ability to pick out seasonal changes in neutron count rates has been unexplored at such a fine spatial resolution. The collection of MONS point data has grown enough that statistically vigorous data can be extracted with the techniques used here. Beyond this milestone, the study demonstrates that there does appear to be seasonal variability in the flux of neutrons (and

therefore the hydrogen abundances) that reflects dynamic properties currently occurring on the martian surface. One can, without reservation, state that MONS has approached a data threshold and can provide a sufficient quantity of records to confidently assess seasonal subdivisions. Also, the study finds existing geospatial methods of change detection such as land use change matrices appropriate for the detection and quantification of seasonal changes in the epithermal rate. The results of these geospatial tools add to the body of recent research that suggests Mars' climate is more dynamic and complex than previously believed.

## Chapter 2 Figures

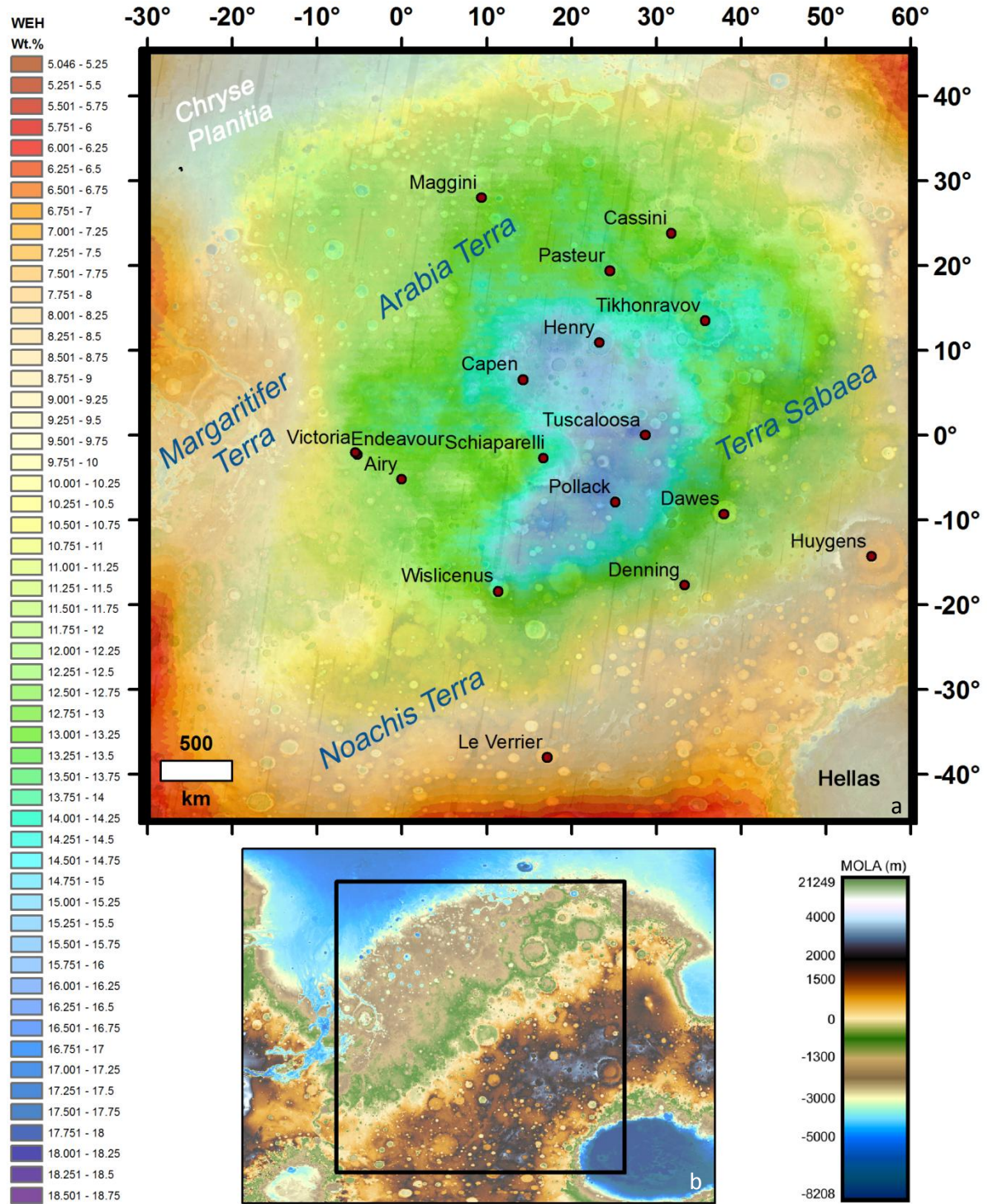


Ch. 2, Figure 1. Plot of WEH and mean epithermal neutron count rates. The relationship between epithermal neutron count rates and Water Equivalent Hydrogen is both inverse and exponential.

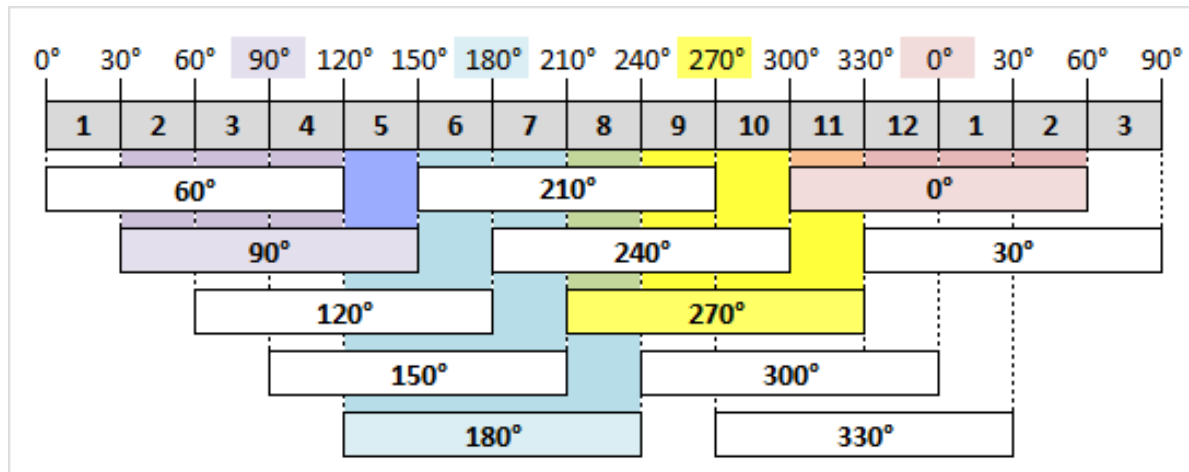


Ch. 2, Figure 2. Graphical representation of Ch. 1, Table A. As the sample size increases, the certainty that the sample mean approximates the population mean also increases. The population size in this case approaches infinity, as neutrons are constantly being generated and escaping.





Ch. 2, Figure 3. Regional epithermal neutron count rates in units of wt.% WEH and elevation. Water Equivalent Hydrogen map of Arabia, Noachis, and Sabaea regions created from a decade of MONS epithermal count records (a). The same WEH scale is used throughout. Elevation map (b), created from MOLA data, shows the location of the WEH map (black square) in relation to the surrounding topography. MOLA elevation scale used throughout. Note the width of the light brown area in the northwest corner in relation to that same elevation at other locations.



Ch. 2, Figure 4. Relationship between temporal slices and martian months. Each temporal slice (long boxes) incorporates the epithermal point data from the two martian months (gray boxes) preceding and following the Ls of interest (labeled above the months). The solstices (90°, 270°) and equinoxes (0°, 180°) have been highlighted to show the overlapping nature of the slices. Data overlap reduces noise in the time series and increases the resampling, compensating for any statistical vigor lost as a consequence of dividing the full dataset into seasons.

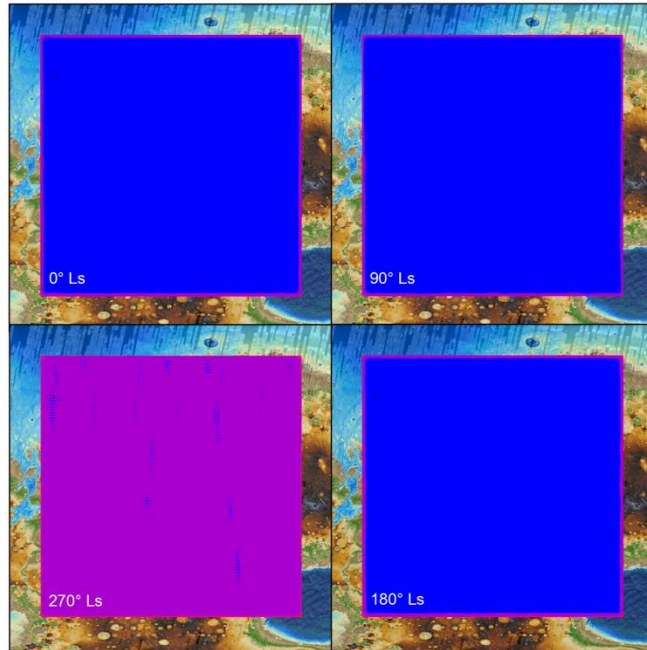
**a**

		Classes from second raster				
wt % WEH		5	6	7	8	Row Totals
Classes from first raster	5	494374	34441			528815
	6	532049	8095458	492354		9119861
	7		1010776	13161753		14172529
	8			1454201		1454201
Column Totals		1026423	9140675	15108308		
Row Totals		528815	9119861	14172529	1454201	
Change (cells)		497608	20814	935779	-1454201	
Change (%)		94.10%	0.23%	6.60%	-100.00%	

**b**

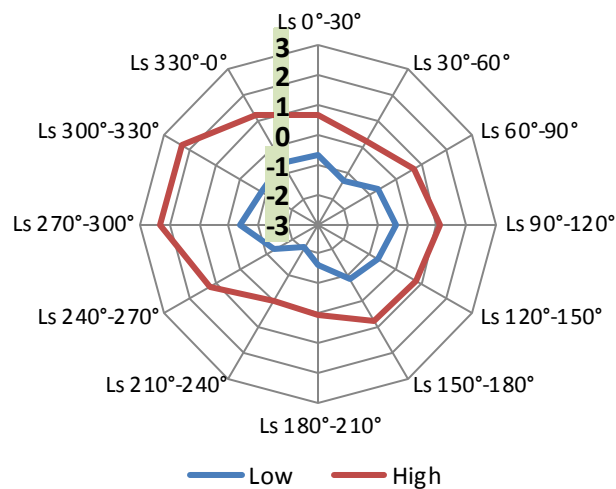
		Classes from second raster			
wt % WEH		5	6	7	8
Classes from first raster	5	6	5		
	6	6	7	6	
	7		7	8	
	8			7	

Ch. 2, Figure 5. Change (a) and magnitude matrices (b). Modeled after matrices for tracking changes in land use categories, the change matrix calculates how cells from one class in a data raster (6, green) are redistributed in the second raster (5-7, blue). Here two WEH rasters are being compared and the numbers 5-8 are the classes. The row total for class 6 is the frequency of class six pixels in the first raster. These pixels are spread out through classes 5-7 in the second raster. The change in frequency can be found by subtracting the number of cells from a class of the first raster (rows) from that of the second (columns). Here there are 20814 more class 6 pixels in the second raster. The change can then be converted to percentages. There is a 0.23% increase in class 6 pixels from the first raster to the second. The magnitude matrix (b) simplifies the frequency information in (a) by displaying the number of digits (the magnitude of the frequency), rather than the count, to show how large a change has occurred.



Ch. 2, Figure 6. Certainty with respect to number of points per node. Confidence in the calculated mean epithermal neutron rate as determined by the count of records included in the calculation of each cell for 4 of the temporal slices (equinoxes 0° and 270° Ls and solstices 90° and 180° Ls). Blue indicates 99% confidence that the sample mean is within half a standard deviation of the population mean. Purple indicates 98% confidence. Note the periphery of each map is edged in lower confidence cells due to the truncation of the sampling window.

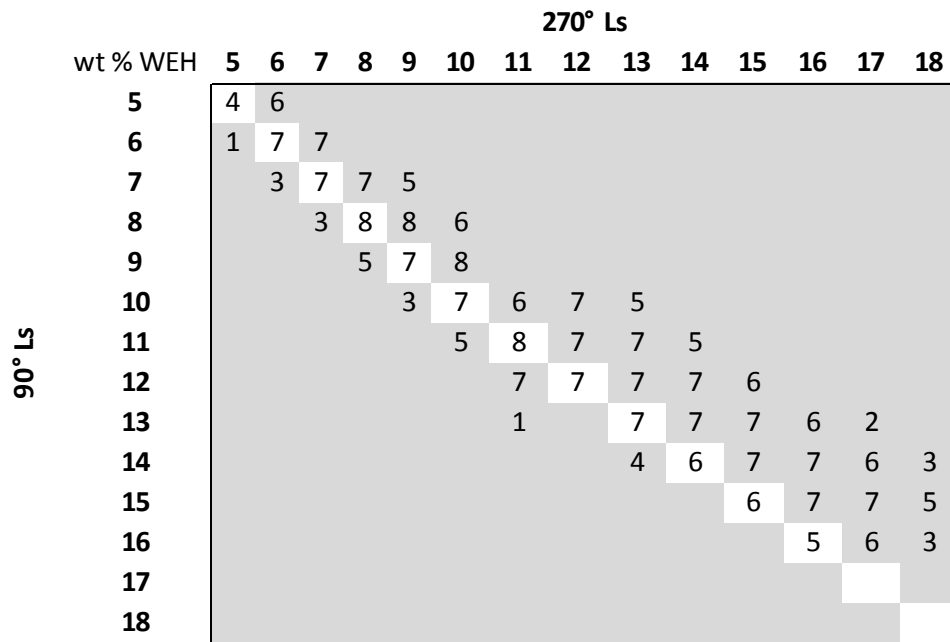
Slices (A – B)	Low	High
Ls 0°-30°	-0.7	0.7
Ls 30°-60°	-1.3	0.2
Ls 60°-90°	-0.7	0.7
Ls 90°-120°	-0.4	1.1
Ls 120°-150°	-0.7	0.8
Ls 150°-180°	-0.9	0.8
Ls 180°-210°	-1.6	0.03
Ls 210°-240°	-2.1	-0.02
Ls 240°-270°	-1.3	1.2
Ls 270°-300°	-0.4	2.3
Ls 300°-330°	-0.8	2.3
Ls 330°-0°	-0.6	1.2



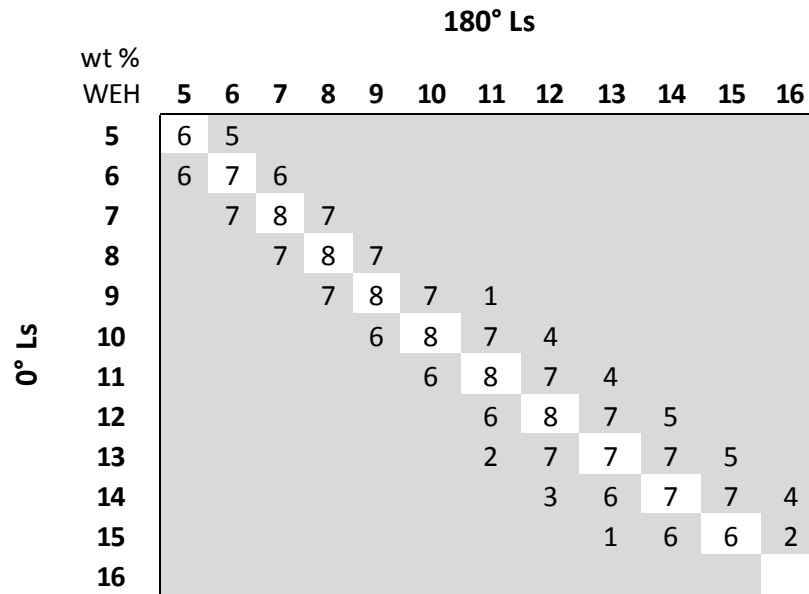
Ch. 2, Figure 7. Minimum and maximum differences between adjacent temporal slices. Radar chart and table of the highest and lowest cells on each raster created of the difference between two adjacent slices. The high values are the most stable after 180°Ls (southern spring).

Ls	WEH																	
	5	6	7	8	9	10	11	12	13	14	15	16	17	18				
0°	52.9	912.0	1642.7	2341.1	2010.5	1536.8	1676.0	1678.0	1101.0	639.5	117.4							
30°	34.8	866.7	1542.4	2374.1	2008.3	1592.7	1632.7	1655.8	1190.1	668.7	141.4							
60°	8.8	730.2	1298.7	2320.8	1951.0	1624.0	1464.6	1514.4	1536.5	745.8	492.8	20.0						
90°	25.1	772.1	1344.3	2312.2	1903.8	1606.0	1482.6	1577.0	1440.6	760.8	461.0	22.3						
120°	93.4	909.8	1660.3	2305.6	1849.7	1585.3	1589.0	1566.8	1253.1	654.2	239.6	0.8						
150°	108.3	927.2	1611.4	2344.0	1829.5	1543.2	1551.9	1611.3	1277.9	658.8	244.0	0.2						
180°	102.6	914.1	1510.8	2375.2	1795.1	1604.9	1453.1	1698.1	1304.9	696.7	252.0	0.2						
210°	25.0	689.8	1188.0	2187.2	1699.6	1782.3	1252.3	1519.5	1595.3	938.1	644.8	185.7						
240°	3.9	452.9	950.4	1841.0	1803.6	1662.0	1345.8	1155.6	1477.3	1461.9	794.7	573.0	180.7	5.0				
270°	0.7	443.1	947.7	1816.9	1801.8	1673.3	1327.4	1151.5	1463.8	1462.5	834.4	492.0	286.5	6.0				
300°	10.6	708.5	1214.3	2201.4	1795.8	1659.9	1322.1	1551.2	1509.2	968.9	554.9	196.3	14.6					
330°	61.9	916.3	1618.6	2309.8	2026.9	1494.8	1612.3	1698.9	1157.1	640.2	170.6	0.4						

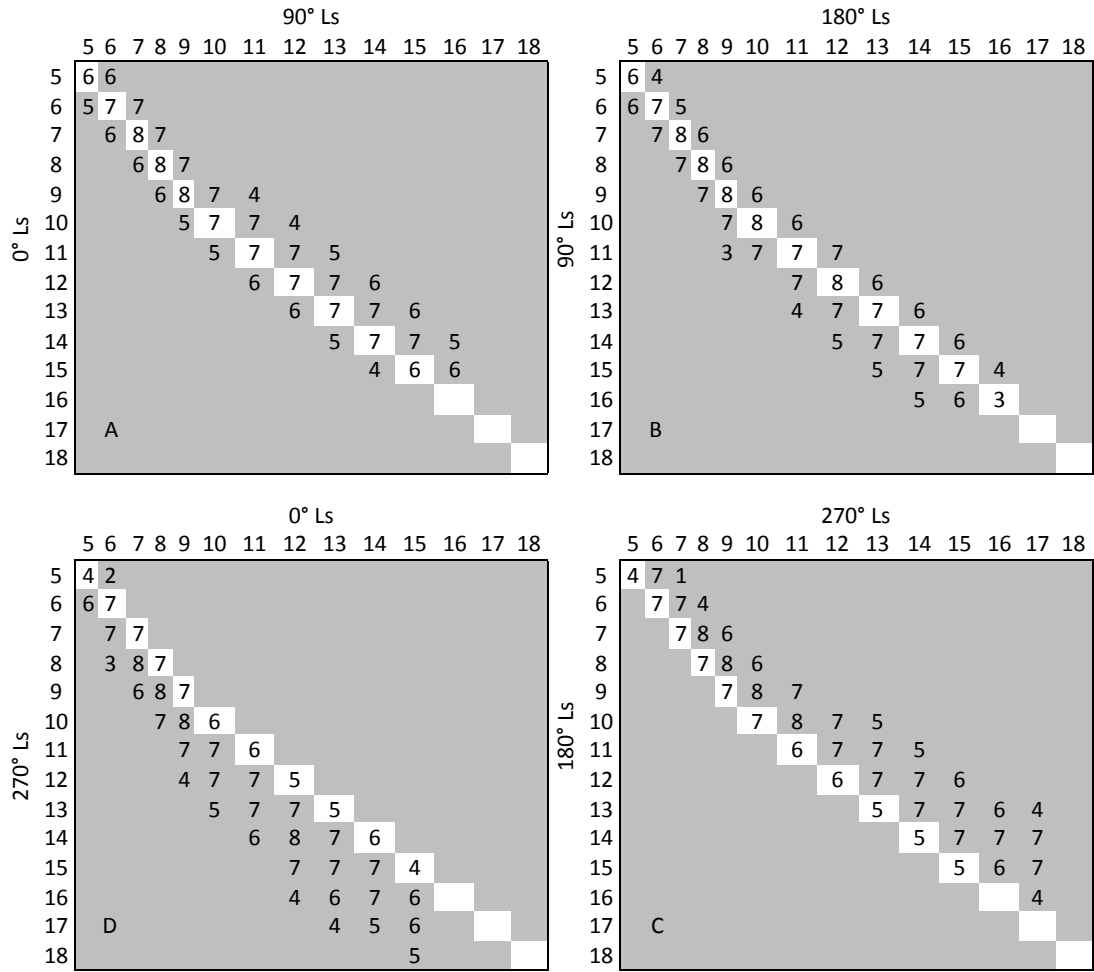
Ch. 2, Figure 8. Cell frequency stored in units of hundreds of thousands for legibility. Cells in green highlight slices in which the highest WEH classes have the most cells/pixels. At the same time fewer cells remain in WEH class 5 giving the impression that the values have shifted to the right.



Ch. 2, Figure 9. Cell/pixel frequency displayed as magnitude. The integer number of digits is reported for combinations of the 90° Ls (aphelion) and 270° Ls (perihelion) slices. Diagonal white line indicates cells that remain in the same WEH class from one slice to the next. Where the number of cells in each WEH class has shifted to the right of the white line, cells have moved from lower WEH classes in 90° to higher ones in 270° during the seasonal change from aphelion to perihelion. This trend is most evident above 10 wt. % WEH.



Ch. 2, Figure 10. The change matrix for the equinoxes (0° and 180° Ls). A relatively balanced change distribution is shown, with classes below 10 wt.% equally likely to drop to a lower WEH class as to move into a higher one. At higher WEH values, the number of classes a cell/pixel may shift increases and there is a preference for cells to move to higher classes. Note that there are no cells/pixels in the 16 wt.% class for 0° but cells from that slice's class 14 and 15 migrated to class 16 at 180° Ls.

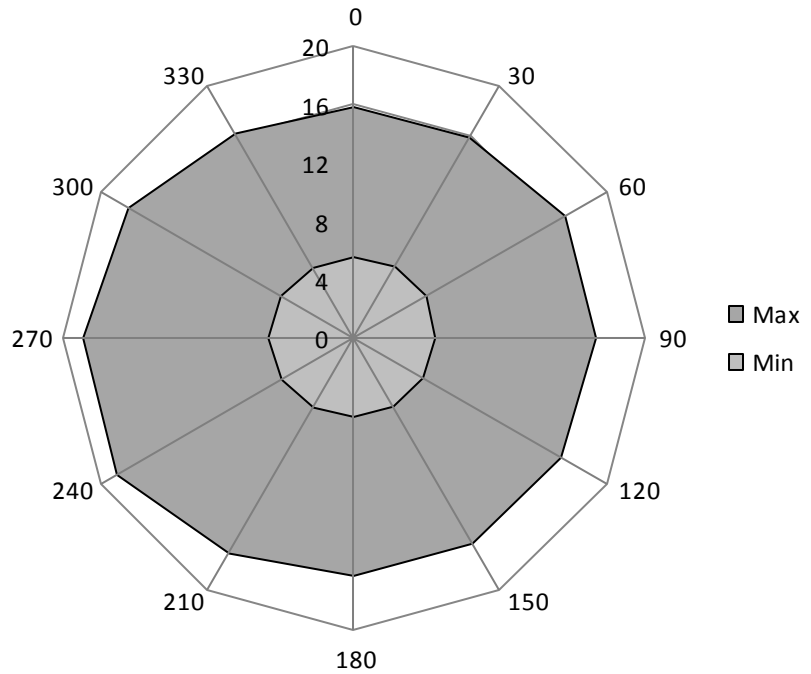


Ch. 2, Figure 11. Change matrices for the transitions between solstices (90°, 270°) and equinoxes (0°, 180°). The charts highlight shifts in the distribution of cells clockwise from one season to the next. It is apparent that 270° Ls has the most cells in the highest of WEH classes. Additionally, changes in all seasons are more spread out from WEH classes 9 upward. This indicates that the changes in hydrogen abundance are more pronounced within the higher classes, regardless of season.

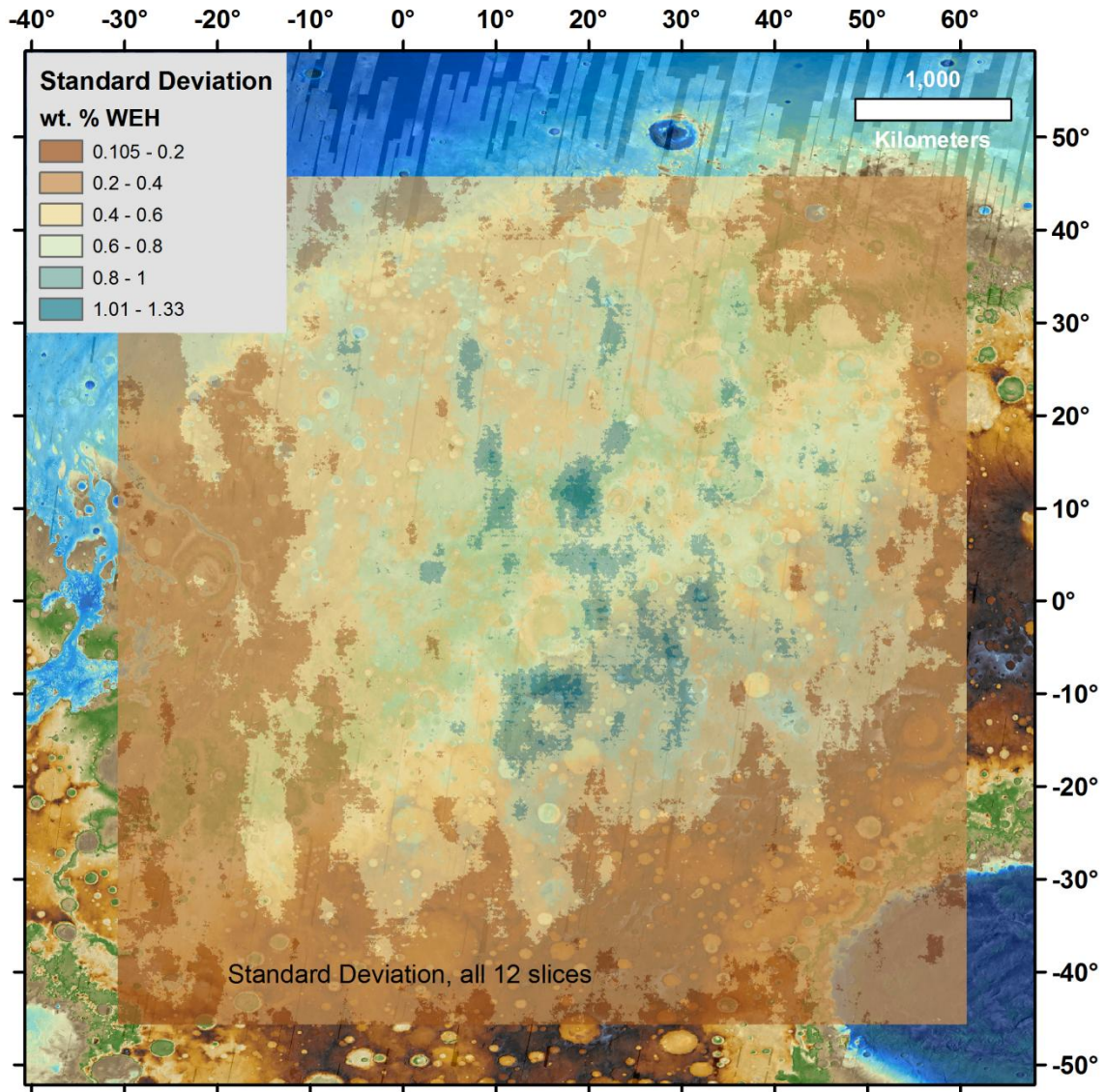
	5	6	7	8	9	10	11	12	13	14	15	16	17	18
90 to 270	-97%	-43%	-30%	-21%	-1%	148%	-42%	-36%	2%	92%	81%	2102%	ND	ND
0 to 180	94%	0%	-8%	1%	-11%	4%	-13%	1%	19%	9%	115%	ND		
0 to 90	-53%	-15%	-18%	-1%	-5%	5%	-12%	-6%	31%	19%	293%	ND		
90 to 180	309%	18%	12%	3%	-6%	0%	-2%	8%	-9%	-8%	-45%	-99%		
180 to 270	588%	120%	68%	221%	-108%	-2%	-17%	128%	-31%	-44%	-15%	ND	ND	ND
270 to 0	7250%	106%	73%	29%	12%	-8%	26%	46%	-25%	-58%	-90%	-100%	-100%	

Ch. 2, Figure 12. Percent change between temporal slices. Percentage of change given in each WEH class from the first slice in each row to the second, as calculated from the previous change detection matrices (Fig. 9-11). Gray shading indicates classes with gains >25%; blues indicate losses. "ND" indicates classes that initially contained no cells in the earlier slice, but cells moved into that class during the subsequent temporal slice.

Ls	Min	Max
0°	5.55	15.84
30°	5.66	15.87
60°	5.75	16.73
90°	5.58	16.61
120°	5.48	16.40
150°	5.42	16.27
180°	5.40	16.30
210°	5.50	17.05
240°	5.70	18.75
270°	5.86	18.55
300°	5.76	17.84
330°	5.56	16.19
Min	5.40	15.84
Mean	5.60	16.87
Max	5.86	18.75

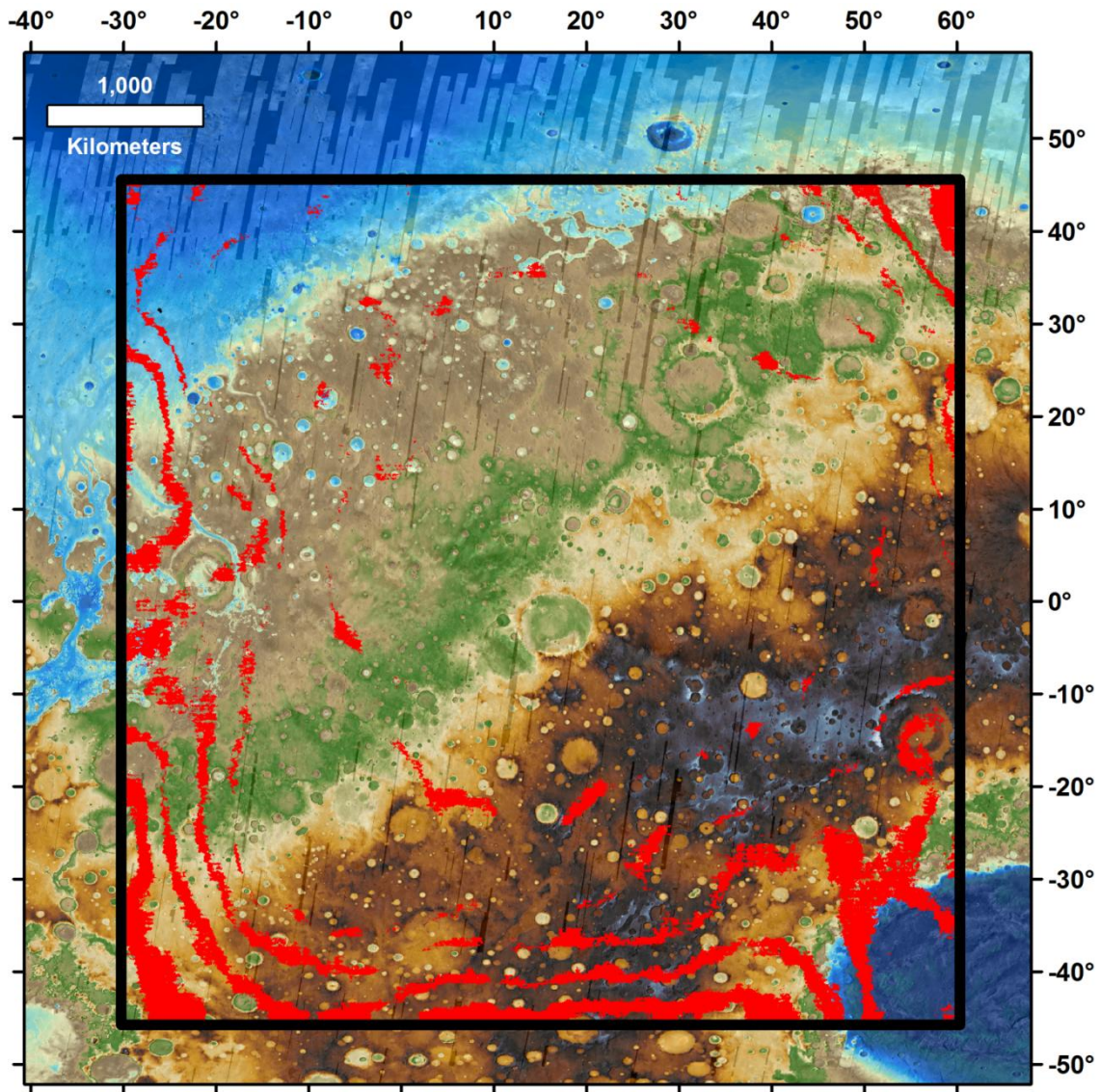


Ch. 2, Figure 13. Slice minimum and maximum values. Plotted on a radar chart, the minimum (interior) and maximum (exterior) WEH values for each temporal slice form a slightly flattened oval. The greatest WEH values correspond with perihelion, 251° Ls, just before the southern summer solstice. There is a smaller peak in hydrogen abundance near aphelion, 71° Ls, just before the northern summer solstice. While the minimum value stays within half of 1 wt.% WEH, the highest value on each slice changes seasonally in a rhythmic manner.

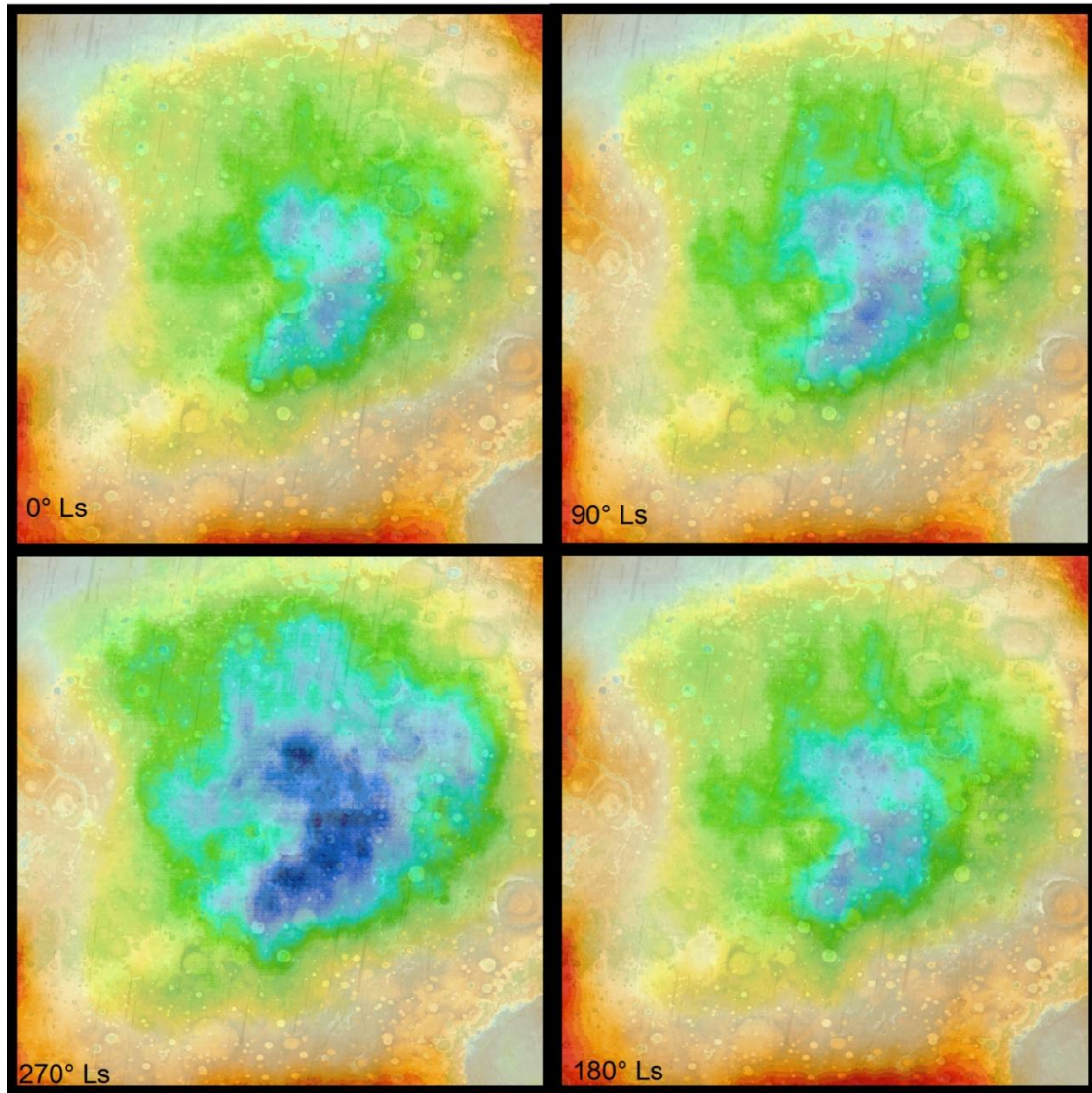


Ch. 2, Figure 14. Cell standard deviation based on the 12 slices. Note that areas with a standard deviation  $>0.8$  wt. % WEH (the largest variation) are concentrated in the center of the region (blue tones).

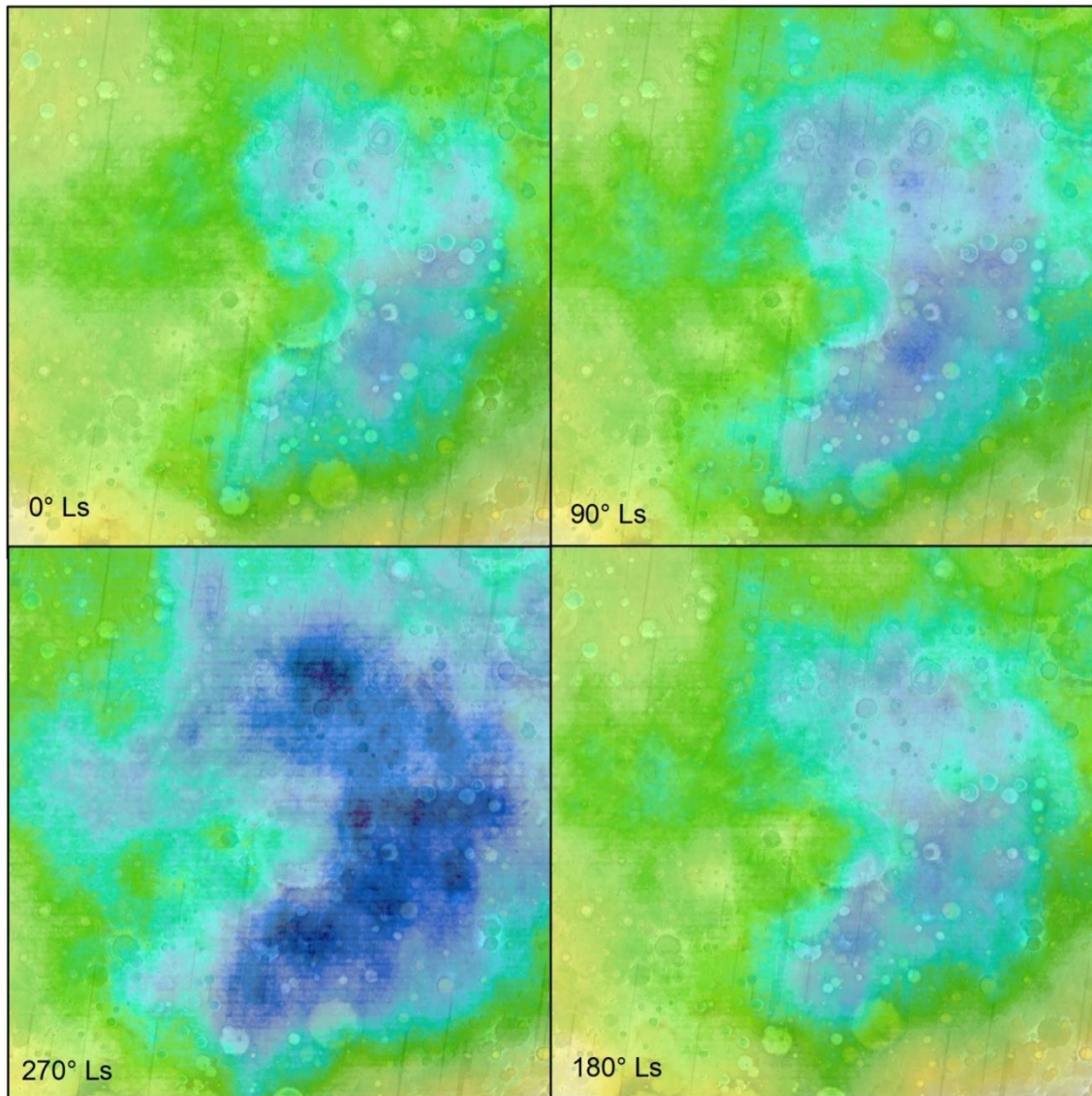




Ch. 2, Figure 15. Static regions of WEH. Areas in red remained in the same WEH class throughout the martian year. While this does indicate areas with less variability, there would be fewer, if any, cells highlighted if the continuous values had not been classified. Elevation scale given in Fig. 3.



Ch. 2, Figure 16. WEH maps of the full data extent for the equinoxes and solstices (clockwise in order.) See Fig. 3 for WEH legend. The equinoxes (northern spring,  $0^\circ$  Ls, and southern spring  $180^\circ$  Ls) show the least extensive WEH pattern. Northern summer ( $90^\circ$  Ls) expands along the highlands behind Schiaparelli, to the east past Tikhonravov, and north toward Chryse Planitia. The largest areal extent of high WEH values occurs in the southern summer ( $270^\circ$  Ls) when the greatest insolation strikes the top of the regional slope. As the air above the surface rises, cool air from downslope moves up hill. As these air parcels rise, they cool, reach the dewpoint and form clouds. Precipitation from clouds formed this way is likely responsible for the location and extent of the eastern equatorial hydrogen signal.



Ch. 2, Figure 17. A closer view of the most variable portion of the region of interest. Clockwise from the upper left: northern spring equinox, northern summer solstice (includes aphelion), southern spring equinox, southern summer solstice. Linear artifacts in 270° Ls stem from the smaller sample size of this time slice. Note the gap where the hydrogen signal is not completely encircling Schiaparelli crater (center). Even during 270° Ls this region remains the lowest WEH area aside from the outer boundary.

## Chapter 2 References

- Bernoulli, J., 1713. *Wahrscheinlichkeitsrechnung. Ars conjectandi*. Ostwalds Klassiker der exakten Wissenschaften, W. Engelmann, Leipzig, 1899.
- Feldman, W. C., Boynton, W.V., Tokar, R. L., Prettyman, T. H., Gasnault, O., and eight others, 2002. Global distribution of neutrons from Mars: Results from Mars Odyssey. *Science*, 297.5578, 75-78. doi: 10.1126/science.1073541
- Feldman, W., Bourke, M. C., Elphic, R. C., Maurice, S., Bandfield, J., and three others, 2008. Hydrogen content of sand dunes within Olympia Undae. *Icarus*, 196, 422-432.
- Jakosky, B. M., Farmer, C.B., 1982. The seasonal and global behavior of water vapor in the Mars atmosphere: Complete global results of the Viking atmospheric water detector experiment. *Journal of Geophysical Research: Solid Earth*, (1978–2012) 87.B4 2999-3019.
- Jakosky, B. M., 1983. The role of seasonal reservoirs in the Mars water cycle: II. Coupled models of the regolith, the polar caps, and atmospheric transport. *Icarus*, 55(1), 19-39.
- Kuzmin, R. O., Zabalueva, E. V., Mitrofanov, I. G., Litvak, M. L., Rodin, A. V., Boynton, W. V., Saunders, R. S., 2007. Seasonal redistribution of water in the surficial Martian regolith: Results from the Mars Odyssey high-energy neutron detector (HEND). *Solar System Research*, 41(2), 89-102.
- Montmessin, F., Forget, F., Rannou, P., Cabane, M., Haberle, R. M., 2004. Origin and role of water ice clouds in the Martian water cycle as inferred from a general circulation model. *Journal of Geophysical Research: Planets*, (1991–2012), 109(E10).
- Novak, R. E., Mumma, M. J., DiSanti, M. A., Russo, N. D., Magee-Sauer, K., 2002. Mapping of ozone and water in the atmosphere of Mars near the 1997 aphelion. *Icarus*, 158(1), 14-23.
- Prettyman, T. H., Feldman, W. C., Titus, T. N., 2009. Characterization of Mars' seasonal caps using neutron spectroscopy. *Journal of Geophysical Research*, 114.
- Richardson, M. I., Wilson, R. J., 2002. Investigation of the nature and stability of the Martian seasonal water cycle with a general circulation model. *Journal of Geophysical Research: Planets*, (1991–2012), 107(E5), 7-1.

- Sharman, R. D., Ryan, J. A., 1980. Mars atmosphere pressure periodicities from Viking observations. *Journal of the Atmospheric Sciences*, 37(9), 1994-2001.
- Teodoro, L. F. A., Eke, V. R., Elphic, R. C., Feldman, W. C., 2010. Pixon goes to Mars: Improved spatial resolution of Mars Odyssey epithermal neutron data. *Lunar and Planetary Science Conference 41*, 1533.
- Teodoro, L. A., Elphic, R. C., Eke, V. R., Feldman, W. C., Maurice, S., Pathare, A., 2011. Azimuthal Structure of the Sand Erg that Encircles the North Polar Water-Ice Cap. *American Geophysical Union Fall Meeting Abstracts*, (Vol. 1, p. 1705).
- Tokar, R. L., Feldman, W. C., Prettyman, T. H., Moore, K. R., Lawrence, D. J., and 5 others, 2002. Ice concentration and distribution near the south pole of Mars: Synthesis of odyssey and global surveyor analyses. *Geophysical Research Letters*, 29(19), 10-1.
- Weng, Q., 2002. Land use change analysis in the Xhujiang Delta of China using satellite remote sensing, GIS and stochastic modelling. *Journal of Environmental Management*, 64, 273-284 doi: 10.1006/jema.2001.0509
- Whiteway, J. A., Komguem, L., Dickinson, C., Cook, C., Illnicki, M., and nineteen others, 2009. Mars Water-Ice Clouds and Precipitation. *Science*, 325 (5936), 68-70. [DOI:10.1126/science.1172344]

## **Chapter 3: Spatial associations between martian equatorial hydrogen distribution, elevation, geologic units, valley networks, and surface materials**

### **Abstract**

In this study, I compare the spatial extent of the largest region of equatorial hydrogen enrichment, as calculated by proxy from epithermal neutron data from the Mars Odyssey Neutron Spectrometer and converted to values representative of the weight percent of water-equivalent hydrogen (WEH) within the upper meter of the martian regolith, with elevation data, geologic units, and other indications of surface materials and characteristics in an attempt to ascertain the constraints on, and likely genesis, of the deposit. I use quantitative and proximity analyses to establish controls on the placement, abundance, and concentration of hydrogen in the 2000 km region surrounding the Schiaparelli Basin. A strong positive trend exists between elevation and hydrogen concentration, with the north-facing slope of the highland topographic rise displaying a greater areal distribution and higher abundances than the south-facing slope. This pattern is consistent with orographic deposition of precipitation, analogous to terrestrial settings. In contrast, WEH values along the Ares Vallis outflow channel increase as elevation drops, indicating a possible erosional component of hydrogen abundance related to minerals being carried downhill under the influence of water or gravity. Regional geology, dominated by two Noachian plateau sequences, shows a stronger association between WEH and the dissected unit, Npld. This unit contains the greatest areal extent of pixels in excess of 14 weight percent water equivalent hydrogen and the descriptor in its unit name, "dissected", suggests the reworking of surface material, conceivably by liquid water moving under the influence of gravity.

## 1. Introduction

In 2002, the Mars Odyssey Neutron Spectrometer (MONS) revealed two unexpected hydrogen-enriched regions along the equator (Feldman et al., 2002). The larger of the two partially encircles the 450 km Schiaparelli Basin, just east of Meridiani Planum (Fig. 1). Schiaparelli is situated in the transition zone between the southern cratered highlands and smoother northern lowlands. The basin also marks a boundary between high and low albedo areas and a change in the thickness of the dust mantling the martian surface (Ruff & Christensen, 2002). Along with changes in age, altitude, and surface materials, there are signs of transitions from subaerial to subaqueous paleoenvironments. The highlands are dissected by both dendritic paleodrainage features that terminate above -1500 m elevation and wider outflow channels with distal ends at -3800 to -4200 m. The dendritic channels occasionally connect to 50 m high inverted channels (Fig. 2), either remnants of cemented sediment from deltas and streambeds that have outlived their banks or sinuous eskers (Burr, 2009) that formed beneath ice fields and piedmont glaciers. This evidence of channelized surface water flow, in conjunction with crater morphologies suggesting paleolakes (Cabrol & Grin, 2002), pingos (Sakimoto, 2005; Soare, et al., 2008), and spring mounds (Rossi et al., 2008), indicate a once robust hydrologic system where water flowed over the surface, through the subsurface, and possibly beneath layers of ice (Fig. 2). The hydrogen detected in this region has variously been attributed to vestiges of this more active system in the form of remnant ice (Boynton et al., 2002), subsurficial water (Harrison, 2005; Michalski, 2013) and brines (Knauth, 2005; Wang, 2006), and hydrated minerals (Mustard, 2008; Poulet, 2005). A case has also been made for an active but reduced hydrologic cycle involving orographic precipitation (Feldman et al., 2004b; Jakosky, 2005; Head et al., 2005; Whiteway, et al., 2009), groundwater sapping (Rodríguez, 2007), and diurnal (Bryson, 2008; Chevrier, 2008) adsorption by hydrateable minerals (Bish, 2003). As it is unlikely that

any single process can account for all of the hydrogen observed in the Schiaparelli region, this study seeks relationships between the epithermal neutron count rate from MONS and existing elevation and surficial data in an attempt to characterize the dominant spatial relationships and possible processes at work.

Based on the regional slope and the relatively gentle transition from northern lowlands to southern highlands, I hypothesize that the distribution of hydrogen enrichment is chiefly influenced by orographic precipitation, but limited by other observable processes or surface features. Constraints on the pattern include dust, which may occlude the hydrogen signal by preventing neutrons from reaching the satellite's detector, and the erosive action of drainages as they remove hydrogen-bearing layers. In addition, I suggest that identification of the geologic units most closely related to hydrogen abundance provides temporal constraints on enrichment and reworking of hydrogen-bearing regolith.

While the epithermal neutron data from MONS revealed hydrogen enrichment at the equator in 2002 (Boynton, 2002; Mitrofanov, 2002; Feldman, 2002), an unequivocal determination of the controlling factors has been problematic due to the uncertainties produced by the size (~550 km) of the MONS footprint (Prettyman, 2004). Previously, I introduced a method of increasing the spatial resolution of the output maps by resampling the epithermal neutron counts (see Ch. 1). This method uses the same calculations to compute the weight percent of water equivalent hydrogen (WEH) as is used in other studies (Feldman et al., 2004b), but replaces the 2° binning with a moving resampling window function to produce sub-kilometer spatial output. Using this process, the pixel size of the output neutron response (given in units of WEH for convenience) can be modified. User selection of the output raster pixel size allows for direct pixel-to-pixel comparisons with existing data sets, such as MOLA elevation data (Zuber et al., 1992). Of course, simply reducing the pixel size



does nothing to improve the intrinsic resolution of the MONS instrument (550 km). Thus I use care to interpret the pixel to pixel comparisons in this study only on regional scales comparable to the instrument footprint.

In this study, water-equivalent hydrogen classes are compared with data derived from other Mars studies, beginning with elevation classes from the Mars Orbiter Laser Altimeter (MOLA; Zuber et al., 1992). A geographic assessment, the location quotient (LQ, section 2.2), is used to determine whether the occurrence of each combination of elevation and WEH appears exactly as often as would be expected were the hydrogen disseminated equally, or if the combination is remarkably frequent or demonstrably rare.

First used as an economic analysis tool in the late 1800s, location quotients were designed to quantify industry frequency in comparison with other regions of a country. The advent of geographic information science widened the use of location quotients to include spatial depiction of crime (Andresen 2007), healthcare access (Phillips et al., 2000), and the digital divide (Gibson 2003). Geologic publications may utilize LQ as a measure of land use or economic resources, but the technique has also been applied to foram abundances (Jones & Cameron 1987) and the effect of coastal run-off on reef systems (McLaughlin, et al., 2002). This study is unique in the application of LQ to planetary resource abundance and geologic interactions.

## **2. Methods & Data**

Data used in this study include WEH values calculated (see Ch. 1) from epithermal neutron count rates from Odyssey's onboard neutron spectrometer (Feldman, et al., 2002), elevation data from the now inoperative laser altimeter (Smith et al., 2001) on the same spacecraft, geologic units

derived from crater counts and surficial morphology (Skinner et al., 2006), dust cover as modeled by thermal inertia (TES, Putzig & Mellon, 2007), albedo measurements (Christensen, et al., 2001), and a raster of valley network density based on vector data (Hynek et al., 2010). Preparation of the data depends on whether the data is a measurement on a continuum (continuous) or a set of categories or integer values (discrete). The WEH abundances and other continuous data sets must be divided into classes (discrete range categories within the data set); categorical (e.g., geologic units) and other discrete data may be used as is, divided further, or amalgamated. Vector data such as shapefiles must be converted to raster format, preferably with a cell size equal to another input raster or the desired output cell size. Alternately, density rasters may be created from vector layers. Trends and associations noted in the results of either of these processes are grouped and projected onto the regional map (Fig. 1) to aid in visualizing the spatial relationships between sets of data.

### **2.1 Combinatorial Or**

Geographic Information Systems (GIS) utilize *Combinatorial Or* operations to calculate the frequency of every combination occurring between two rasters and ascertain the spatial distribution of these combinations. This could be calculated by hand on a small enough area, but the GIS routine also creates both the frequency table and a map in the form of an output raster. Every cell in the output raster corresponds to the same cell location on the two input rasters. As noted previously, all layers must be divided into classes comprising discrete, user-defined ranges within the data set. The output cell is a record of the class value for each of the parent rasters and carries information on the class value of each in addition to a unique value representing the combination of the two classes.

The comparison of two layers of map data (e.g., dust cover and albedo; Table A) using *Combinatorial Or* produces a frequency table detailing the unique combinations that arise as well

as the raster defining the spatial arrangement of those groups. Along with a unique identifier for each specific combination and the number of times each combination is encountered, the table lists the class value for each of the two layers (Table A). Additional fields can be added to the table, such as a grouping of combinations, to allow for a more instructive characterization that retains the original spatial registration, enabling the map to display according to the new fields.

By exporting the table into a spreadsheet and sorting the table by classes for the desired x axis with the y axis as the secondary sort parameter, the totals for each combination can be arranged into a frequency matrix (Table B). The number of possible combinations is dictated by the number of classes within each raster set (here, albedo and dust classes). For example, if one raster set has seven classes and the other has 10, there are 70 unique combinations and the tallies can be organized within a 7x10 matrix. Occasionally, a pair of data sets will not contain every combination possible, resulting in empty matrix cells. *Combinatorial Or* matrices are useful visualization tools, describing the distribution of one dataset within the classes of the other. Any empty cells within the matrix clearly define the extent of interaction between the layers of interest.

In this analysis, I have created matrices that depict the combination of hydrogen abundance rasters with MOLA elevation data (Zuber et al., 1992), its derivatives (slope and aspect), geologic units (Skinner et al., 2006), valley network density (created from valley networks; Hynes, 2010), albedo (Christensen et al., 2001), and dust cover (Putzig & Mellon, 2007).

## **2.2 Location quotient**

*Combinatorial Or* frequency matrices provide the structure for a further quantitative statistical analysis: the location quotient (LQ). Location quotients are the ratio between two related ratios. In the first ratio, the numerator represents the frequency (number of pixels) where a class selected from the primary dataset overlaps with a specific class from a second set. This is divided by all

occurrences of the primary class (all of the pixels within that class). The second ratio's numerator is the pixel count of the second set's class. This in turn is divided by the total number of pixels in the mapped region. Originally designed as a means to compare the concentration of a resource within a small spatial unit to that of the encompassing base, here the LQ is used as a ratio describing the abundance of a given combination (e.g., specific classes of hydrogen abundance and elevation) to that of all the possible combinations of those two layers within the study area.

Row and column totals are calculated for each horizontal and vertical class in the frequency matrix. This is a direct measure of the number of pixels in each of those classes. The sum of the rows should match the sum of the columns, as this grand total is the number of pixels in the *Combinatorial Or* layer. The LQ matrix is created by copying the frequency matrix's structure. Each cell's tally is replaced with an equation that references the same cell (column and row) of the initial frequency matrix such that:

$$LQ = \frac{(\text{cell/row total})}{(\text{column total/grand total})}, \text{ Eq. 3-1, see Figure 3.}$$

Wherever the value of (cell/row total) approaches the value of (column total/grand total) the frequency of the selected combination within the class (row total) is proportional to the frequency of the columnar class (column total) within to the entire mapping area and the LQ value is very close to 1. One is the expected value when a resource is spread throughout the smaller unit (the row) with the same ratio as it is through the entire region (the total number of pixels). In the case of albedo and dust, if a cell's LQ equals one, the proportion of the frequency of the combination of pixels having that particular class of dust and that particular albedo class to the frequency of all the pixels that albedo class is exactly the proportion of the frequency of pixels in that dust class to the number of pixels in the *Combinatorial Or* map layer.

The farther the LQ value is from 1, the more notable the combination. LQ values greater than 1 indicate a more frequent than expected occurrence of that particular unique combination of dust and albedo. Similarly, LQ values less than 1 indicate that the combination is less common than expected; however, a low LQ value result may still be insightful. For example, if there isn't as much 16 weight percent hydrogen at -2000 km as expected, then looking for the spatial distribution of that unique combination on the map with respect to its geomorphic setting may indicate alternate controls on this combination.

To facilitate visual evaluation of the LQ data, each LQ matrix in the study was simplified by coding the cells into 3 generalized classes: High ( $LQ > 1.2$ , class 2), Low ( $LQ \leq 0.8$ , class 0), or Expected ( $0.8 < LQ < 1.2$ , class 1). This simplification facilitated viewing these as charts of the relationship between the two data sets. In the case of two sets of continuous data, the graph is a simple XY scatterplot. When the classes of one dataset represent discrete units, such as geologic units, the matrix can be viewed as a (somewhat discontinuous) bar graph. Should these units have no inherent rank, the bars may be reordered to better organize, emphasize, and evaluate the LQ data.

A matrix may also be duplicated multiple times to replace the LQ values with numeric values representing clusters or new classes (Fig. 4). To see the spatial distribution of these groupings, the LQ calculations and any classes from duplicate matrices can be appended to the original table and saved as a .dbf file (Table C). When the database is joined to the original raster layer in ArcMap, the new fields can be used as a display parameter by using the Symbology tab within the Properties dialog in ArcMap.

### ***2.3 Water Equivalent Hydrogen***

Mean epithermal neutron count rates, considered in past work (Ch. 1, 2; Feldman et al., 2002; Prettyman, 2004; Prettyman, 2006), are used again here. Additionally, I investigate median count

rates as an alternative measure of central tendency to mitigate the influence of data outliers. The use of both measures allows us to compare results at each sample location to look for outlier-induced variations. Statistical confidence is independent of the measure of central tendency employed, depending instead on the number of counts used to obtain either measure of central tendency (Ch. 1, section 3.2).

The epithermal neutron counts were calculated from MONS records collected between February 2002 and June 2012. Both mean and median were calculated using three resampling window sizes, 50, 75, and 100 km radius circles. All windows had at least 400 samples. With this number of samples, Maurice et al (2011) demonstrated that for the frost-free data set below 60 degree latitude on Mars, the hypothesis that the population per window, with a 99% probability, is that of a random population cannot be rejected. He represents each window of the data set by its mean value and a statistical error bar and stated that sample sizes above 400 have a Gaussian distribution. This allows the measure of central tendency to converge strongly (Fig. 5), providing a 99% probability that the calculated measure is within half a standard deviation of the actual value of that measure for the epithermal count rate at that location for the time period covered. This does not compensate for the instrument footprint size, however and features in the MONS signal smaller than 2-3° may be spurious.

Prior to being converted to WEH, the rasters produced by the 50, 75, and 100 km radius sampling windows were averaged, producing two weighted rasters, one for each measure of central tendency. The result was equivalent to passing a filter over the original total counts with a 3x weighted center (diameter 100 km) encircled by an inner 2x weighted torus (25 km wide) and an outer torus, also 25 km wide. This variation in weighting emphasizes data nearest the sampling node without excluding regional influences. For both measures of central tendency, the map

output was set at 463 m per pixel to complement the pixel size of elevation data from the Mars Orbiter Laser Altimeter (MOLA, Zuber et al., 1992). Hydrogen abundance values were divided into equal interval classes (for use in *Combinatorial Or* and LQ matrices) representing one-fourth of one weight percent of Water Equivalent Hydrogen (i.e., 0.25 wt.% WEH). The raster of mean values ranges from classes 6 to 46 (6.5 to 16.75 wt.% WEH). The range of the median WEH raster extended from class 6 to class 47 (6.5 to 17 wt.% WEH).

## **2.4 Classes for Remaining Datasets**

In addition to the hydrogen abundance layers, the study includes data that describe the elevation, geologic setting, and surface materials. Also included are geomorphic features apparently incised by flowing water. Each of the following data sets were selected for the purpose of determining potential controls on the hydrogen signal as detected in the upper meter of the martian regolith.

### **2.4.1 Elevation and derivatives**

Elevation data from MOLA (Zuber et al., 1992) was divided into 250 m divisions. Class 1 includes values <-5000 m, whereas at the upper elevation range, class 36 represents those values >3500 m. Slope and aspect (slope direction) layers were derived from the MOLA data. Slope was divided into 15 user-defined classes, with the first three in increments of 1%, the next eight having increments of 2%, and the final four classes extending from 19 to 25%, 25 to 30%, 30 to 50%, and >50% slope. Nine aspect classes were created: four each for the cardinal (N, S, E, W) and ordinal (NE, SE, NW, SW) directions with an additional class for flat areas.

### **2.4.2 Surficial geology**

Our knowledge of martian strata is limited, although expanding. Global geologic units (Skinner et al., 2006) on Mars currently represent changes in surface expression, with only scattered locations mapped from ground observations. Relative ages have been approximated by crater-counting

techniques and crosscutting relationships, allowing differentiation between Noachian and Hesperian plateau sequences. Each geologic unit was treated as an individual class for use in the *Combinatorial Or* process and initially ranked by the order of occurrence in the original database. An argument could be made to sort the units chronologically, but without an explicit stratigraphic record there is no inherent ranking between the disparate units within each epoch.

### **2.4.3 Dust Cover Index**

Surface dust values (Ruff & Christensen, 2002; Bandfield, 2002) from Thermal Emission Spectrometer (TES onboard Mars Global Surveyor) data range from 0 to 2.11 in a dust cover index (DCI). DCI is based on an average emissivity (the relative ability of a surface to emit energy by radiation) from the 1350 to 1400  $\text{cm}^{-1}$  frequency (Ruff & Christensen note that an emissivity  $>1.0$  is not physically possible, suggesting values above 1 indicate a contribution from the denominator in the ratio used during processing). Only 3400 cells/pixels (2.9% of total) have DCI values above one; these were grouped together into the highest class. Over a third of the pixels contain DCI values between 0 and 0.0225, and were grouped into the lowest class. For the purposes of comparison with WEH, the remaining cells are split into 5 DCI classes with class widths of 0.2.

### **2.4.4 Albedo**

TES-derived bolometric albedo values (Christensen et al., 2001) in the mapped area range from 0.061 to 0.32 Lambert units, where fresh snow has an albedo of  $\sim 0.90$  L and fresh asphalt 0.04 L. These values were divided into ten classes. Class 1 covers the darkest values (0.061 – 0.13 L) and class 10 has the brightest range (0.29 – 0.32 L). The remaining eight classes each have a range of 0.02 L from 0.13 – 0.29 L.



### **2.4.5 Valley Networks**

Fluvial valley vector data (Hynek et al., 2010) were converted into density rasters before classification to show where the valleys were concentrated. The density analysis was performed with a 50,000 km<sup>2</sup> window with 463 m output (cell size on the map). The resulting values represent units of valley length per unit of area, without any weighting for valley width. Six classes were generated, with class 1 having zero to 0.001 km/km<sup>2</sup> (that is, zero to 1 m of valley network per km<sup>2</sup>). Class 2 has 1 to 10 m/km<sup>2</sup>, class 3 has 10 to 25 m/km<sup>2</sup>, class 4 has 25 to 50 m/km<sup>2</sup>, and class 5 has 50 to 100 m of drainages/km<sup>2</sup>. The final class contains 100 to just over 200 m/km<sup>2</sup>. The vectors used to define the valleys are simple lines, so this highest class reflects a substantially incised topography.

## **3. Spatial Analysis Results**

### ***3.1 Mean and Median Epithermal Neutron Counts***

When comparing graphs of mean versus median counts for each WEH class, it is apparent that: (1) mean values are shifted toward the lower classes; and (2) for the most part, the respective histograms are merely offset (Fig. 6). However, from 11.5 to 14 wt. % WEH, there are two peaks in the mean values and three in the median. These effects are probably the result of the non-linear conversion employed between the neutron count rates and the WEH units. As the mean and the median values are more or less the same, either may be used to calculate neutron count statistics and WEH values.

### ***3.2 MOLA with WEH***

The LQ matrix for elevation (MOLA) and hydrogen abundance (WEH) provides a visual representation of the dominant combinations of classes in the two data sets. When projected on to

the regional map, the locations of these combinations indicate the spatial relationships between combinations that are more frequent than expected and those that are less common.

### 3.2.1 Distinct Trends

The daughter matrix for elevation with hydrogen abundance displays two distinct, continuous bands of higher than expected LQ values (blue bands in Fig. 7). The trends of these bands indicate a positive relationship exists between hydrogen concentration and elevation, with higher WEH values at higher elevations. The dominant trend begins with low elevation (~5 km) and low WEH (~8 wt. %) and continues to elevations of ~2.5 km with WEH abundances of ~17 wt. %. The secondary trend begins at the aeroid (0 km) with WEH concentrations of 6.5 wt. % and terminates at the highest points in the map area (3.5 km and above) with WEH values around 11.5 wt. %.

These areas of more frequent-than-expected combinations can be further differentiated by creating classes based on clusters within the two trends (e.g., the dominant trend become class 3 with a decimal value denoting hydrogen abundance – 3.1, 3.2, 3.3, 3.4) (Fig. 8). Joining these classes to the existing LQ data provides a method of visual discrimination between the separate trends while indicating increasing concentrations of hydrogen within the trend (e.g., the WEH classes are grouped into four broader divisions, as the dominant trend crosses these groups the decimal place changes from 3.1 to 3.2, 3.3, and the highest hydrogen concentration within the trend, 3.4). Figure 8 displays the dominant trend in dark blues (class 3 and its subdivisions) and the secondary trend in shades of cyan (class 5 and its subdivisions), describing the spatial relationship between the two. For both trends, the darkest shades of color indicate the highest WEH concentrations, which coincide with the highest elevations.

### 3.2.2 Map projection of MOLA with WEH

When the LQ classes from the matrix in Figure 7 are used as a display parameter and overlain on the base map (Fig. 9), the clusters of low, expected, and high LQ are arranged concentrically.

Somewhat continuous rings of lower than expected frequency, in white, surround a central area of more frequent than anticipated values, shown in blue. The lower values are disrupted by patches and swaths where the LQ values are close to one (yellow).

Switching the display parameter to the classes defined in Figure 8 reveals the spatial relationships between the trends in the high LQ combinations (Fig. 10). The dominant trend, class 3, in shades of dark blue, covers the most area, highlighting the north-northwest-facing slope of the topographic rise between the northern lowlands and the cratered highlands. The highest concentrations start around -1000 m and culminate before 2000 m. Above this elevation are class 7.4 (high LQ, but no longer positively associated) and bands of low and expected LQ where the concentration weakens as elevation increases to the southeast. The secondary trend is located geographically on the southeast slope of the central topographic rise, which dips toward Hellas Basin.

### 3.2.3 Minor Negative Trend

One area of negatively trending high LQ combinations can be found in the lower left corner of the matrix (class 7.1, Fig. 8). When projected onto the map, the values correspond to Aram Chaos and portions of Ares Vallis and the adjacent plains (Fig. 11). This is the one area where the high LQ combinations of elevation and WEH exhibit a strong negative trend. At the lowest elevation, on the floor of Chryse Planitia, classes -3750 to -4000 m, WEH ranges from 8 to 8.75 wt. %, while elevations from -2750 to -2000 m, in and along the Ares Vallis channel, vary from 7 to 7.5 wt. %. Ares Vallis once served as an outflow channel for Aram Chaos, the easternmost chaos feature feeding into Chryse Planitia.

### 3.2.4 Irregular Patches of High LQ

Discontinuous areas of high LQ combinations (class 9, Fig. 8) are also present and are spatially distributed throughout the mapping area (purple shades, Fig. 10). The largest concentration of these combinations occur between the two positive trends (class 9.5), but small clusters and individual combinations can be found throughout the matrix. On the map, most are located east and west of the dominant trend's slope, with fewer cells in the highlands between the two trends, and a small amount near Hellas Basin's rim. Spatially, most of these areas are patches and swaths that either blanket a locality or highlight the rims of craters, but not the interiors. There are a dozen exceptions where craters in one class appear to have pierced through another class, but this is an artificial distinction as the WEH values are similar for both classes; the only difference between these craters and their surroundings is their elevation class. Of these, the cluster with the largest aerial extent (greatest number of pixels) fills an eroded, unnamed crater in the southwest corner of the mapping area and extends over 400 km to its northwest, around to the west, and off to the southeast.

### 3.2.5 Examination of Areas with Low LQ Values

Examining the spatial location of areas of low LQ provides additional insight into the distribution of hydrogen with respect to elevation. After differentiating the lower than expected combinations into classes on the basis of their location on the LQ matrix (Fig. 8) and dividing these classes by hydrogen abundance, the results were spatially projected onto the regional map.

The low LQ combinations beneath the dominant trend on the matrix (orange hues) have lower elevations than adjacent high LQ areas with the same wt. % WEH. With only a few exceptions, these low LQ areas are related to craters within the region of the dominant trend on the north west-facing slope. The exceptions may be eroded crater basins. The two largest of these may have been

over 200 km in diameter, but now appear as clusters of joined depressions south of Maggini and southwest of Pasteur (Fig. 12a). Very few of these low-LQ craters are south of the equator. The exceptions are considerably smaller: a ~50 km crater near Airy crater, several ~30 km impact craters between Schiaparelli and Wislicenus crater, and several <20 km depressions north and east of Endeavour crater. However these features are probably spurious because their areas are far below the intrinsic resolution of the MONS instrument.

The low LQ combinations between the two positive trends in the matrix (class 15, light through dark browns, Fig. 8) are also located between the two trends when projected on the map (Fig. 10). Spatially, this class separates the two positive trends across topographic highs and wraps to the north and northwest of the dominant high LQ class (blue, Fig. 10) on the northwest-facing slope. The highest WEH concentrations within class 15 (>12 wt. %) blanket the highlands. Unlike the orange classes, these darkest browns are higher in elevation for similar WEH classes and rarely fill a crater without blanketing the adjacent plain. The highest WEH (>16.5 wt.%) on the map has a low LQ component, class 13.2, found in the area around Pollack crater and the west slope of the highest relief between Dawes and Pollack craters (Fig. 12b, brown).

Class 17, shown in dark red on the matrix (Fig. 8) and the corresponding map (Fig. 10) consists of the low-LQ combinations above the secondary positive trend in the matrix (cyan). These represent combinations of high elevation and low to very low (<11.5 wt. %) WEH. This class is spatially associated with the secondary trend and concentrated on the highlands around LeVerrier crater (Fig. 12c).

On the LQ matrix (Fig. 8), class 13 occurs at each end of the dominant positive trend. At the low WEH-low elevation end, between the dominant trend proper and those combinations associated with Aram Chaos, class 13.1 is made of low LQ combinations that map to the bottom of the Ares

Vallis channel at its narrowest point (Fig. 9) as well as along the rim of Hellas Basin (Fig. 10d, golden tan adjacent to the blue band). The low-LQ combinations at the high WEH end of the dominant trend (class 13.2, Fig. 8) spatially relate to the areas of the map where high elevation and high WEH coincide: adjacent to Pollack crater (Fig. 10b, golden next to the dark brown) and in the highlands directly south of Schiaparelli Basin.

### ***3.3 Geologic Units with WEH***

Construction of the WEH with geologic units (Skinner et al., 2006) LQ matrix clearly shows that some units are not associated with high hydrogen abundance (>10 wt.%, Fig. 13). While the continuous data from the MOLA and WEH combinations results in an almost filled LQ matrix (Fig. 7), half the matrix cells are empty for the combinations of geologic units and WEH. Constrained by the abundance of WEH associated with each discrete geologic unit, only 565 unique combinations exist within the over 105 million pixels in the map area. Of these, only 210 of the combinations represent WEH values above 12 wt. % ( $39.3 \times 10^6$  pixels). On the low end of the WEH values, 232 of the combinations display WEH values of 10 wt. % or less. The geologic units were ranked, with units sorted by the highest WEH class combination. Where two units shared the same highest class (e.g., Nlpr and cs), the unit with the greatest number of high LQ combinations was assigned the higher rank.

Of the 14 geologic units that have any cells above 13 wt.% (Fig. 13, units v and above), ten have high LQ combinations where the WEH class is above 13 wt. % (Npl1, Hplm, and HNu do not). Of the ten, six are plateau sequences (Npld, Nplr, Hpl3, Npl2, Nplh, and Nple) and three are impact crater material (cs, cb, s). There are only eight plateau sequences in the mapped area. The only one without a high LQ combination above 12% wt. % is the Npl1, the cratered unit of the six Noachian

plateau sequences (Fig. 14, red). This unit has the largest aerial extent of all of those in the study area and has a strong relationship with WEH values below 9.5 wt. % (Fig. 15, row 1). Of the 7 high WEH plateau sequences, five are Noachian and two are Hesperian. The Noachian dissected plateau sequence, Npld (Fig. 14, dark blue), has the second largest aerial extent (Fig. 15, row 2) and is rare below 9.5 wt. % WEH (Fig. 13). Npld is the most strongly associated with high WEH of all the units, possibly indicating the valleys dissecting the unit may have formed in the presence of liquid water.

### ***3.4 Dust with WEH***

The LQ matrix for dust cover and hydrogen abundance has two distinct clusters of more-common-than-expected class combinations (Fig. 16, blue). At the lowest WEH values (6.5 to 9.5 wt. %) thicker dust cover (see 2.4.3) is infrequent (Fig. 16, white), with the majority of combinations containing little to no dust (0 to 0.2 DCI). At 9.5 wt.% WEH, the dustiest combinations abruptly become more frequent. A shallow negative trend of increasing WEH with decreasing dust extends to the highest WEH classes (up to 17 wt.%). The dust-free class remains infrequent, indicating high hydrogen abundance is associated with dust cover to some degree.

The LQ classes for dust with hydrogen abundance have the low LQ combinations divided into three groups: 0.1, for thicker dust at low WEH values; 0.2, for the combinations of little to no dust with WEH >11.5 wt. % WEH; and 0.3 for those combinations of thick dust and >13 wt. % WEH. When projected onto the regional map (Fig. 17), class 0.3 covers the greatest aerial extent and has the clearest signal of the three. The signal is strongest to the west of Schiaparelli (Fig. 1) and continues south and east of the crater. The sharp, NW-SE trending, linear boundary across the map corresponds to a change in albedo with class 0.3 predominantly associated with the bright area (see Fig. 4 for the relationship between dust cover and albedo). Class 0.1 is apparent around the edges of the mapping area, but is clustered in the scoured region near Aram Chaos and Ares Vallis as well

as along the boundary with Chryse Planitia (Figs. 1 & 11.) Class 0.2 is infrequent, but appears within the blues and violets of class 2). Class 1 (Fig. 17, yellow) represents all combinations that occur just as frequently as expected and is most common as a dividing unit between the low WEH/low dust high LQ class (2.1, dark green) and the high LQ classes with greater hydrogen abundance (classes 2.21-2.28). In the dust with WEH matrix (Fig. 16), class 2.28 represents those combinations of high hydrogen abundance and a minimal, although quantifiable, amount of dust. In the map (Fig. 17, violet) the class is most contiguous to the north and east of Schiaparelli basin.

### **3.5 Albedo with WEH**

A strong positive association exists between albedo and hydrogen abundance (Fig. 18). WEH values <10 wt. % were infrequent to non-existent for the 4 brightest classes (>0.23 L; Christensen et al., 2001). Where the WEH exceeds 13 wt. %, albedo levels above 0.25 L dominate. Of particular note, there is one area of high (15.5-15.75 wt. %) hydrogen abundance within the darkest (0.061- 0.13 L) albedo class. When projected onto the base map, this corresponds to the area adjacent to Pollack crater and extends over 400 km to the west (Fig. 19, red). A similar area, where the darkest albedo is combined with moderately high (12.5 – 13.25 wt. %) WEH, covers Endeavour crater, where the MER rover, Opportunity, is exploring (light orange).

Classes for the low LQ combinations are decimal values based on the WEH value (e.g., class 0.1 is any low LQ combination where WEH <9 wt. %, Fig. 19, darkest gray). Combinations that are as frequent as expected are yellow, whereas high LQ combination class names describe both the WEH and albedo class values (e.g., class 6.8 has 15 to 16 wt.% WEH and is in albedo class 8).

### **3.6 MOLA Derivatives with WEH**

Elevation data derivatives such as slope and aspect provide additional insight into the interplay between topography and other datasets. The two measurements are intertwined with slope being



the ratio of change in elevation over horizontal distance and aspect being the direction that each slope faces. The size of the study area introduces some difficulty in using these derivatives on the same scale as the hydrogen data (i.e., although WEH and both aspect and slope have spatial resolutions of 463 m per pixel, the cratered surface creates constantly changing values for the MOLA derivatives); however, regional generalizations are still possible.

### **3.6.1 Slope**

Due to the intense cratering, slopes of every degree are common all across the study area (Fig. 20a). It is not a trivial matter to improve the varying nature of the slopes through geospatial processing, nor would the processed data be as meaningful. The simplest way to visualize slope, therefore, is by creating topographic profiles to view regional trends with respect to hydrogen enriched areas. A dozen profiles were created in the areas of highest WEH abundances, but none showed any relationship between WEH and steepness of slope. The profiles did, however, reinforce the observation that WEH increased up both the Chryse- and Hellas-facing sides of the topographic rise, tapering off before the highest elevations (regardless of slope).

### **3.6.2 Aspect**

Again, the predominance of impact structures interferes with the usefulness of aspect data for this study. Each crater's circular bowl contains a slope of each aspect while the slope of the outer rim contains complementary aspects (Fig. 20b). Utilizing focal statistics to record the predominant aspect in every cluster of pixels only consolidates the aspect information to a small degree. At best, one can look at the regional slope and show that there are two predominant aspects: a north-northwest slope facing the lowlands and its complementary south-southeast face sloping down toward Hellas Basin. Of these two faces, the lowland-facing slope has the highest connection to hydrogen enrichment.

### **3.7 Valley Networks**

Valley networks (Hynek et al., 2010) generally form dendritic channels at higher elevations, with some exceeding 800 km in length, and possessing well-developed tributaries extending as far as 180 km to either side (Fig. 21). At lower elevations along the dichotomy boundary, channels are spaced farther apart and exhibit short tributaries, commonly arranged at angles close to 90° from the primary valley, and typically suggestive of tectonic control on drainage. Mawrth Vallis (Fig. 1) is the best-developed and most continuous of these at ~700 km in length.

Exceptions to the generalizations on valley patterns with respect to elevation include channels on the flanks of Huygens (Fig. 1), a younger, well-preserved multi-ringed basin, and the outflow channel, Ares Vallis (Figs. 1, 11). On the exterior of Huygens' crater, radial valleys are short and dendritic, although steep. These channels often terminate centripetally into adjacent craters. Outflow channels are generally longer (>1500 km) and broader; they have visible sources (chaos features, chasms, and grabens) and they are often sinuous, frequently exhibiting braiding at their distal ends.

Valley density is highest at elevations from -1700 m to 2000 m on the northwest slope of the topographic rise (Fig. 1). There is a broad (~1000 km) band in the lower elevations to the north of Endeavour where valley density is low or null, before the transition to the drainages along the edge of the dichotomy boundary where the northern lowlands (blue) meet the southern highlands (tan).

#### **3.7.1 WEH with Valley Density**

The LQ values of WEH with valley density are similar regardless of whether the median or mean WEH is used. Here (Fig. 22), valley density is paired with median weighted WEH. The most striking observation is that combinations with WEH values <9.75 wt. % are dominated by lower than

expected LQ values at higher valley densities (see section 2.4.6), while combinations with values >14.25 wt. % WEH are more frequent than expected for the same densities.

Figure 23a shows the LQ values with the same symbology as the LQ matrix (Fig. 22; class 0, white; class 1, yellow; and class 2, blue). Note that the class 1 combinations, where the LQ values indicate the frequency is as expected if the densities and abundances were equally frequent throughout the map, occupies the greater part of the mapping area and is nearly uninterrupted across the wide plain where there are fewer channels. High LQ combinations are further differentiated by WEH value (e.g., in Fig. 22, 14-15 wt.% for class 6, 15- 16 wt.% for class 7). Figure 23b uses these new classes to examine the spatial relationships between high LQ classes. The low density, low WEH combinations (class 2), correspond to the south and west edges of the mapping area (Fig. 23b, green). LQ classes 5 – 9 are concentrated in the center of the study area (blue through violet), are successively higher in WEH, and vary in their associated valley density.

### **3.7.2 Valley density with MOLA**

Combining valley density with MOLA data provides a method of visually quantifying the occurrence and extent of these putative fluvial systems with respect to elevation (Fig. 24). A cursory examination of the matrix reveals key differences in the LQ values above and below -1500 m elevation. Below this level, valley densities greater than 10 m/km<sup>2</sup> are rare to non-existent. However, above -1000 m, this same group occurs more frequently than expected and, with the exception of 1250 to 2500 m, the densest classes dominate.

Observing the spatial relationship between the two sets of data (Fig. 21) confirms the matrix results. At the highest elevations (>2500 m), areas with little to no drainages are rare (Figs. 21, 24). This trend changes from 1250 - 2500 m, with valley network density slightly lower in the highlands at the bottom of the map. Along the aeroid (martian sea level, Figs. 1, 21, light tan to green), from 0

to 750 m, numerous valleys terminate along a southwest-northeast trending line, resulting in fewer than expected combinations between these elevations and the 0 to 1 m/km<sup>2</sup> valley density class.

#### **4. Discussion**

If a strong positive association exists between two data sets, it is reasonable to expect some influence or control either by one set on the other or by an outside process on both. Similarly, if certain geologic units are strongly related to high (or low) WEH concentration, either the process that created the unit or the materials prevalent at that location are implicated in the control of hydrogen distribution. It is unrealistic to expect there to only be one factor controlling the distribution of hydrogen, although one process may dominate. When evaluating multiple potential influences, the isolation of secondary controls across the entire mapping area is not feasible; however, it should be possible to find localized zones where typically secondary factors take precedence.

In addition to examining the data from the LQ matrices, scrutiny of the dissimilarities between the study area and the rest of equatorial Mars is essential to understanding the processes and interactions at work in the region. Aside from a less spatially-extensive antipodal area, the region centered on Schiaparelli basin is the predominant site of hydrogen enrichment at low latitudes. The most prominent differences between this highland region and the rest of equatorial Mars include a broad transition from the northern lowlands and a >5000 km southwest to northeast topographic high. The transition is unique in that the dichotomy boundary that separates the northern lowlands from the cratered highlands tends to be an abrupt change in elevation elsewhere. Rather than a 3 km rise over a 250 km run, the rise is spread out over 2500 km. This moderate transition culminates

another 2000 km, rising >3 km more to the top of the topographic rise, creating a gently-sloping, broad slope.

#### **4.1 Geomorphic Control**

Physical relief exerts considerable control on the active processes in a region, creating a feedback loop where the changes set in motion by existing topography can alter the original landscape. One plausible control on the distribution of hydrogen in eastern equatorial Mars is the northwest-facing slope mentioned previously.

Terrestrial equatorial settings experience a range of climates where terrain is mountainous. Cloud cover is common in these locales and the mechanics of adiabatic cooling produces frequent precipitation on the windward slope. Equatorial glacier formation is also possible with the right combination of moist air masses and change in elevation (Kaser, 1999; Fastook et al., 2008).

Precipitation, especially on sloped terrain, creates drainage patterns that develop into established channels and watersheds. The formation of these channels involves cutting through the existing topography and transporting the excised material down-slope under the influence of gravity.

##### **4.1.1 Orographic Control**

As noted, at most equatorial regions areas across Mars the dichotomy boundary manifests as a cliff rather than a gradual slope. This slope acts as a ramp to direct parcels of air upward from the lowlands. Orographic lifting creates clouds through adiabatic cooling. The thin atmosphere on Mars is dry compared to terrestrial standards, but easily saturated due to the low carrying capacity.

Lowered atmospheric pressure allows air masses to expand and cool as they are forced upslope by air currents. When cooling reaches the dewpoint, clouds begin to coalesce as liquid and frozen aerosols merge, gaining mass. Precipitation may be active, as snow or rain, or passive as dew or a

fog that adsorbs onto rocks and diffuses into the regolith (Jakosky, 1983). Each of these methods allows moisture to be exchanged from the atmosphere to the planetary surface.

With the exception of the area between Endeavour and Wislizenus, west of Schiaparelli (Fig. 1), as elevation increases on the north-facing regional slope, hydrogen abundance increases in a manner congruent with orographic control (Fig. 10, dark blue). The LQ matrix for WEH and MOLA (Figs. 7, 8) indicates a positive trend composed of unusually frequent combinations of elevation and hydrogen abundance. Furthermore, projecting the data onto the map shows this trend to be coincident to the face of the slope where orographic precipitation would be expected.

While rain is not currently observed on Mars, the Phoenix lander observed snowfall similar to the arctic precipitation known as diamond dust (Smith, 2009). Observations of clouds and low-lying fog are common, opening up the possibility of frost and rime (freezing fog) as modern hydrogen (in the form of  $H_2O$ ) deposition mechanisms, especially on a diurnal cycle as the thin troposphere becomes saturated each night when the temperatures dip. Similar processes in Mars' past likely brought rain and snow to the cratered highlands (Head et al., 2005) and should be considered as a probable origin for at least a portion of the hydrogen signal.

Winds moving from the poles to the equator carry moisture in proportion to the air volume (Feldman et al., 2005). The north polar region currently boasts the most robust icecap, favoring orographic deposition on the north-facing slope of the topographic rise as winds move southward from the polar region. The Hellas-facing (i.e., southward facing) slope shows less hydrogen enrichment, but the LQ matrix (Figs. 7, 8), shows a definite positive trend of higher frequency than expected elevation and hydrogen abundance combinations. When projected onto the map (Fig. 10, cyan), the location of these pixels corresponds to the Hellas-facing slope of the topographic rise.

Hellas Basin does not seem to act as a sink for the hydrogen, nor does it appear to direct as much airflow equatorward. The attributes of the Hellas-facing hydrogen deposit, lower hydrogen abundance than the opposite face of the rise with moderate (<11.5 wt. % WEH) hydrogen abundances at the crest of the rise, decreasing with elevation into a hydrogen-poor basin, are congruent with the rainshadow effect seen on the leeward side of terrestrial mountain ranges. As moisture-depleted parcels of air descend a slope, they heat up above the dew point, no longer depositing precipitation. The drying air mass can also drive evaporation in the terrains it crosses. The limit of orographic precipitation appears to be bracketed by the increase in elevation on the windward side of the topographic rise and the decrease in elevation on the leeward side.

#### **4.1.2 Valley Networks**

The windward side of the topographic rise is incised by valley networks in a manner congruent with extended precipitation. Four distinct modes of fluvial behavior are apparent. There are three areas without apparent valley dissection that form the first mode. The second mode includes outflow channels and the straighter, lower stream order channels with mouths along the dichotomy boundary, emptying into Chryse Planitia (Fig. 11). Dendritic channels comprise two modes based on stream order and channel length.

The first mode, covers four areas where no fluvial behaviors were noted: Chryse Planitia, (Figs. 1, 11, 21a), Hellas basin and portions of the Hellas facing slope, as well as a large, relatively flat region from -1500 to -1250 m on the windward side of the topographic rise (Fig. 24, MOLA elevation class 16, also notable for a change LQ class distribution). The lack of valley networks within Chryse and Hellas can be attributable to their lower elevation and, in the case of Hellas, a possible rainshadow influence. The large, flat region extends from Meridiani to Cassini (Figs. 1, 22a) forming a transitional plain between the longest dendritic streams and the short valleys emptying into Chryse.

There are indications (Fig. 2a, c) of transitions between subaerial and subaqueous topography. Due to the extreme cratering in the region and the incidence of eroded, filled, and otherwise altered large (>200m) basins (Fig. 12a), it is not unreasonable to suspect that paleolakes once dotted the region, becoming the discharge point for the dendritic streams upslope and the source for the circum-Chryse headwaters. The Meridiani region has well-documented (Squyres, 2006) deposits characteristic of standing water (Christensen and Ruff, 2004) and it is possible that similar deposits are located throughout this stretch of possible impoundment, but are currently masked by the heavy dust load in the area.

The circum-Chryse channels' morphologies indicate a fast-moving fluid, with the lack of many higher order channels suggestive of many of these channels having had a singular point source (e.g., a breached paleolake) with minimal contribution from the surrounding terrain. Again, dust in the region could be shrouding some smaller feeder branches, as there is no indication of current hydrologic activity in this region. The circum-Chryse valleys might also be spring fed channels, with the source fluids moving below the surface, through impact-fractured breccia and along fault lines.

The upper 58% of elevation classes are dominated by the two most densely dissected modes (Fig. 24). Dendritic channels cover the upper reaches of the topographic rise (Fig. 21). Mode 3, at the highest elevations, has lower stream orders (Strahler numbers of 3 or less) and moderate (>250 km) channel lengths. Mode 4, at slightly lower elevations on the windward side (roughly -1250 to 1250 m), is limited to the more developed dendritic valleys. This densest mode of valley network classes is strongly linked to the highest WEH classes (Fig. 22, 23b blue shades), but also associated with the high LQ combinations outside of the two main trends (Figs. 8, 9, purple shades) where the elevation is roughly the same as the upper WEH classes of the main trend, but the hydrogen abundance



matches the middle elevations of that trend. Note that this particular area drains into a chaos region, which in turn drains into Ares Vallis, possibly accounting for the lowered WEH values.

The modes of the valley networks appear to indicate an increased need for drainage (i.e., a greater source of fluid) at the higher elevations, with more developed systems (Mode 4) between the highest, younger systems (Mode 3) and an area of possible ponding (Mode 1). This ponded area appears to be drained directly into Chryse Planitia by simpler, faster channels (Mode 2). The hydrogen signal is most associated with the Mode 4 channels associated with the Mode 1 impounded area, while Mode 4 channels that appear to connect directly to Mode 2 outflow networks have a lower level of hydrogen for their elevation. While elevation controls the drainages and the hydrogen, the lowered hydrogen abundance in the vicinity of Mode 4 channels that connect directly into outflow features, despite being at the same altitude along the topographic rise as the high WEH Mode 4 drainages suggests that there is an aspect of control by the drainage on WEH. Whether the connection outflow features drained the valley system more rapidly, limiting the time available for hydrogen to bond with minerals in the regolith, or deposits of minerals were stripped from the area during a period of rapid downcutting, some process reduced the hydrogen abundance.

#### **4.1.3 Erosion**

Stream valleys develop by the movement of fluid on a gradient from highest to lowest elevation. Downcutting, caused by the incision of the stream into bedrock or regolith as it attempts to create a flatter gradient, erodes the surface through hydraulic action, abrasion, and the dissolution of chemical bonds. The sediments created from these erosive processes are then transported along the bottom as bedload, as a suspended load of clays, silts, and fine sands, or in solution.

The transportation of these sediments ends when stream velocity slows, creating bar and placer deposits, deltas, floodplains, and alluvial fans. Minerals that have been dissolved may precipitate out as evaporite deposits when streams end in ponded areas that subsequently evaporate.

Additionally, fluids moving through the subsurface may deposit minerals in veins as the fractures create more surface area for chemical interactions.

In all of these cases, material that had been higher on the slope is moved to a lower elevation. The LQ matrix for MOLA and WEH (Fig. 8, LQ class 7.1) indicates that there is at least one region where the hydrogen abundance has increased with decreasing elevation. The pixels in this class are located in and around Ares Vallis (Figs. 10, 11b, LQ class 7.1, light green). There is an indication that hydrogen levels in this area, although low compared with the other trends, are being enriched. The implication is that regardless of how the hydrogen is manifested in these low-lying regions, the source material has been transported and consolidated in this region on a detectable scale. This could be related to the lowered WEH in the Mode 4 stream that connects to Ares Vallis (Figs. 8, 9, purple shades) or it could be a consequence of the outflow system's enormous scale of erosion and deposition. Either way, the increase in WEH at the lower extents of Ares Vallis indicates that there may be a fluvial sediment component to the hydrogen signal.

#### ***4.2 Geologic Interpretation***

As noted, currently recognized geologic units are based on surface features and geomorphology while our knowledge of martian stratigraphy continues to expand. The LQ matrix for WEH with geologic units (Fig. 13) indicates that the majority of units associated with higher hydrogen abundances are plateau sequences from the Noachian and Hesperian periods. When these units are map projected, they cover the bulk of the study area (Fig. 14). The two most areally extensive units, Npl1 and Npld, are the cratered and dissected units, respectively, of the Noachian plateau

sequence. The two are very dissimilar in terms of hydrogen abundance, with Npld having the greater WEH abundance. A case can be made that the characteristics used to name the units reflect the processes that make their WEH profiles different (Fig. 15, top 2 rows). The term *dissected* relates to valley networks, which were previously noted to be associated with higher hydrogen abundances, perhaps explaining the high WEH link with unit Npld. *Cratered*, on the other hand, implies reworking of the surface by impact events, the distribution of which are unrelated to the spatial distribution of geologic target materials that could potentially affect WEH abundances by way of their mineral compositions. It could be that the apron debris from these impacts is masking both the valley networks and the hydrogen.

The age of these units, determined by crater count to be Noachian, places a wide temporal constraint upon the hydrogen abundance. If the cratered unit is masking the signal, then the hydrogen deposition predates the impacts. Note that crater counting does not indicate that the craters on a unit formed during that period in time; rather it indicates that the terrain is ancient enough to record the stretch of impactor history that followed. For this reason we can only say that the hydrogen deposition likely started at the time the topographic ridge was uplifted and continued during the period when the valley networks were incised and the ponding occurred.

Estimates on the cessation of hydrogen deposition would depend on the discovery of temporally well-constrained cross-cutting events. For example, there are indications that the fluvial channels were still active when the impact in Figure 2a occurred (to the right of the red arrow). The debris apron appears to have obscured the original valley leading into the paleolake (red arrow); however, a few areas appear to have deepened (black arrow, darker shades of blue) where ponding may have occurred before the waters breached an obstruction and began down-cutting again, in a different direction.

### **4.3 Surface materials**

Both Dust and Albedo datasets indicate variability in surface materials. The two have a strong negative relationship with each other such that dust-free areas are predominately low albedo (dark) terrains. The opposite is also true, with brighter areas having a strong tendency toward heavier dust loads (Fig. 3).

#### **4.3.1 Dust**

Most areas devoid of measurable dust are relatively depleted (<9.5 wt.% WEH) in hydrogen (Fig. 16, LQ class 2.1; Fig. 17, green), but the thickest dust cover relates to only moderate (~10 to 13 wt. %) WEH and the trend then increases in hydrogen abundance as the amount of dust diminishes. While the lack of dust corresponds to low WEH, there is no evidence that the dust is controlling the extent of the hydrogen. There is no indication that a component of the dust has a significant hydrogen or hydroxyl component or that the dust adsorbs moisture. If either were the case the WEH would be expected to increase with increasing dust.

The negative relationship between dust and moderate to high WEH may reveal more about where dust occurs than how it relates to hydrogen abundance. As discussed previously (Ch. 3, 4.1.2), the moderate WEH values closely relate to paleolakes that lie between the dendritic valleys and the circum-Chryse channels. As the network of lakebeds and floodplains dried out, the desiccated fines would have become airborne and redeposited as silty loess beds topped with aeolian dust deposits, accounting for the thick dust cover index at this elevation. As elevation increased away from the source, the heavier loess deposits would taper off in favor of the also-thinning dust layer. In this scenario, the coincident location of the dust and the beginning of the primary positive WEH with MOLA trend (Fig. 8, classes 3.2, 3.3) is attributable to elevation, gravity, and aeolian processes.

### 4.3.2 Albedo

The relationship between albedo and WEH is not as clear cut as previous combinations, but there is a positive association between bright areas and high hydrogen abundances. For the most part, areas with low WEH (Fig 18, <9 wt.%) tend to have low albedo values (<0.19 L). Figure 19 depicts these low albedo areas (class 2.0, <11.75 wt. % WEH) as light green. The trend continues as moderate WEH (10-13 wt. %) with middle albedo values (0.19–0.27 L, Fig. 18, class 3.0; Fig.19, dark green) extend from the edge of the dichotomy boundary with Chryse Planitia on the northwest to the top of the regional topographic rise between Dawes and Huygens in the southeast.

The dusty areas around Tikhonravov, Cassini, and unnamed large basins between Maggini and Pasteur (Fig. 19, teal, classes 4.8, 4.9, 5), signify hydrogen abundances between 13 and 15 wt. % WEH that correspond to the brightest albedo levels (0.25 - 0.32). The highest WEH classes (>15 wt. % WEH, Fig. 18, LQ classes 6.8-7.9; Fig. 19, blues) are also within the brightest albedo levels. This last group is adjacent to the low LQ values (Fig. 18, LQ classes 0.4 and 0.5; Fig. 19, lightest grays) in the dark albedo surrounding Schiaparelli (Fig. 1). Within this area are the exceptions to the positive trend between bright albedo and high hydrogen abundance.

These exceptions include two LQ classes in the darkest albedo class (4.1 and 6.1) as well as two with similar WEH levels to the teal classes, but with moderate albedo levels (4.4 and 4.5). Class 6.1 (Fig. 19, red), located west of Pollack crater corresponds to dark areas that appear to be exposed around the base of a localized area of high relief.

A gap in the WEH signal (Ch. 1, Fig. 9, Western Gap) between Endeavour and Wislicenus (Fig. 1), corresponds to one of the most densely incised area of valley networks (Fig. 21b, 0-10°Lat, 0-10° Lon). North and south of this region, the moderate albedo classes (4.4, 4.5) appear in the bright

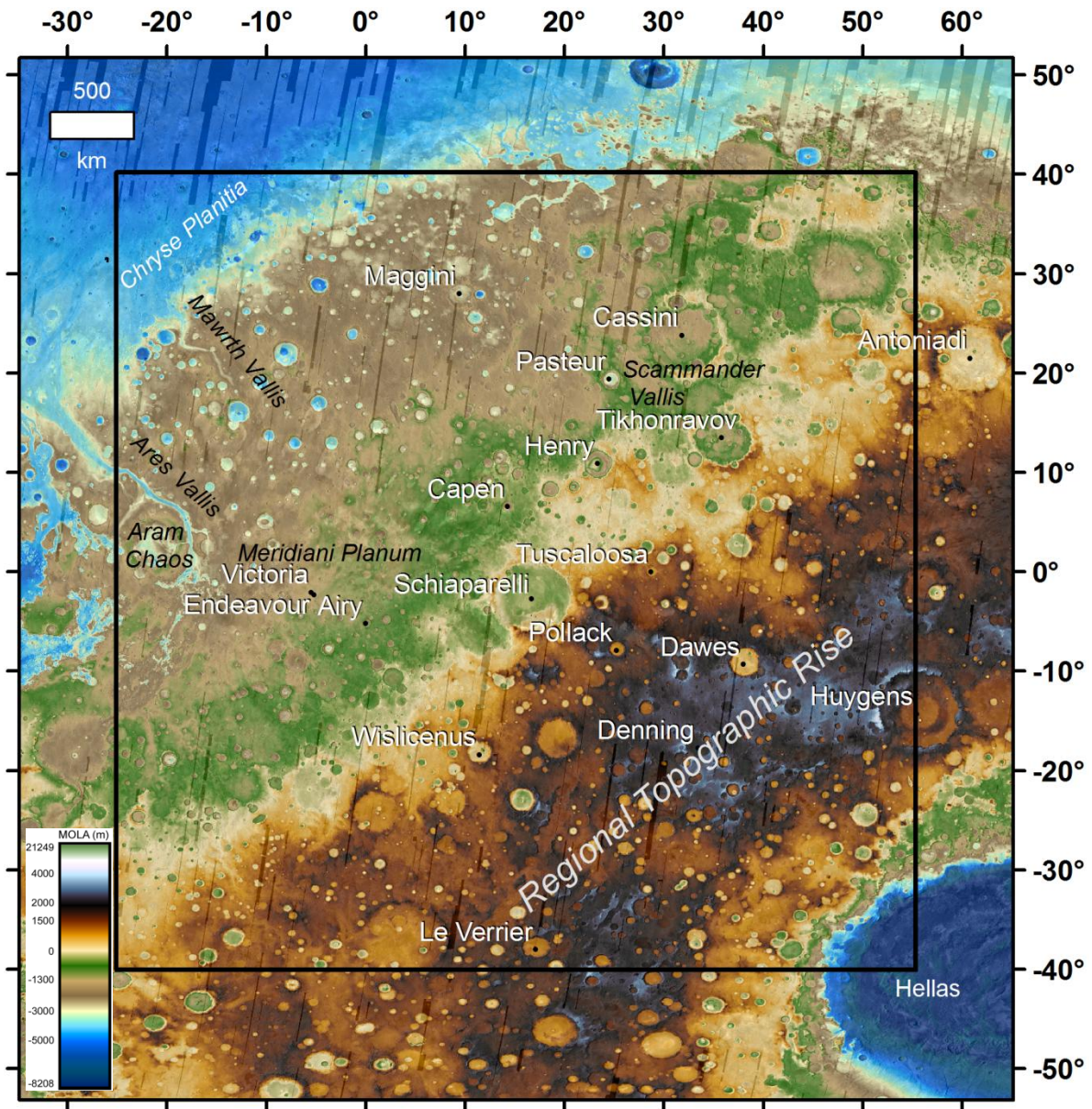
areas adjacent to darker locals. Within the gap, the darker class (4.1) covers a topographic low adjacent to a rise of nearly a kilometer in less than 200 km. Hydrogen levels are only slightly lower in the darker class, mostly due to a smaller range of values (12.5– 13.25 wt. % as opposed to 13 – 14 and 14.5 – 14.75 wt. % WEH). Once again, as with dust cover, the control on hydrogen does not appear to be albedo as much as elevation.

## **5. Conclusions**

Regionally, the dichotomy boundary appears to control the northern extent of the hydrogen signal and the top of the topographic rise forms the southern boundary. The source of hydrogen, attributed to orographic deposition, is primarily controlled by geomorphology. The gradual increase in elevation from the northern lowlands to the cratered highlands permitted the formation of clouds and deposition of precipitation in the highlands, which then led to the development of dendritic valley networks, providing a means for the distribution of hydrogen back down the slope under gravity. Such well-developed drainages indicate that the process of deposition and fluvial transport, once developed, continued over a long period of time. Indeed the deposition of hydrogen in the form of precipitation likely continues into the present on a much smaller scale. Clouds, fog, and frost, all visibly active on the planet today, move moisture from the atmosphere to the surface, often in a diurnal cycle. In addition to hydrogen bound to evaporite minerals in the regolith, water ice deposits and brines are likely present less than a meter beneath the surface, within the detection range of the neutron spectrometer. The hydrogen signal, then, can be thought of as the indication of the extent of past, and conceivably current, water and water ice deposition. Another geomorphic control, erosion, can be seen where drainages have cut into older terrain, depositing reworked material at lower elevations. These low-lying areas may also be the site of evaporitic sulfate deposits where flood plains and depressions concentrated pools of salty water

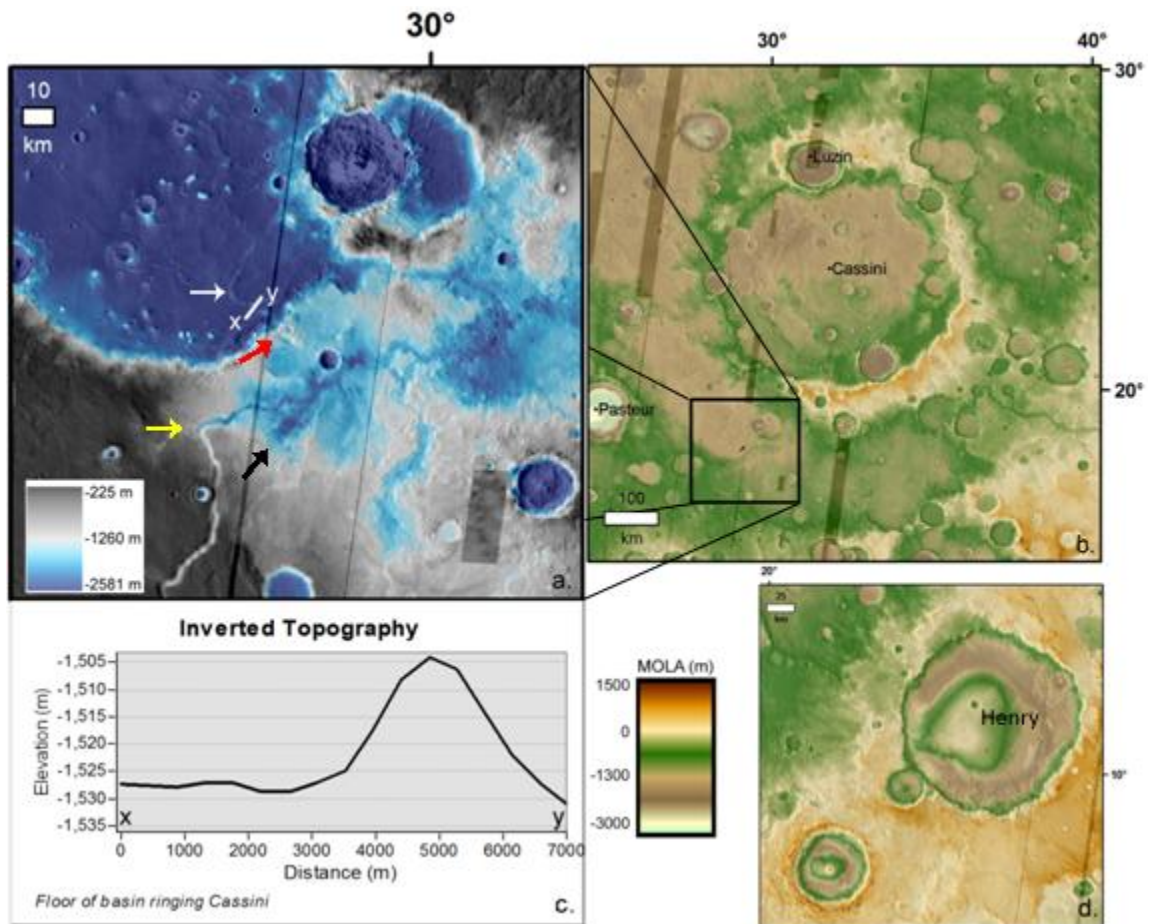
into layers of hydrous minerals. Of the remaining data examined, none proved to have significant control on the areal extent of the hydrogen signal. Rather than exerting control, geologic units describe the surface features which relate to the relative abundance of hydrogen. Neither dust cover nor albedo appears to control the distribution of hydrogen, but both of these are controlled by the same geomorphology of elevation, fluvial networks, and erosion.

## Chapter 3 Figures



Ch. 3, Figure 1. MOLA topography centered on Schiaparelli basin. Black square indicates the aerial extent of the data in the study. A broad NE-SW trending topographic rise separates Arabia Terra from Hellas Basin and the rest of the cratered highlands. The aeroid, martian "sea level" follows the green to light tan elevation transition.





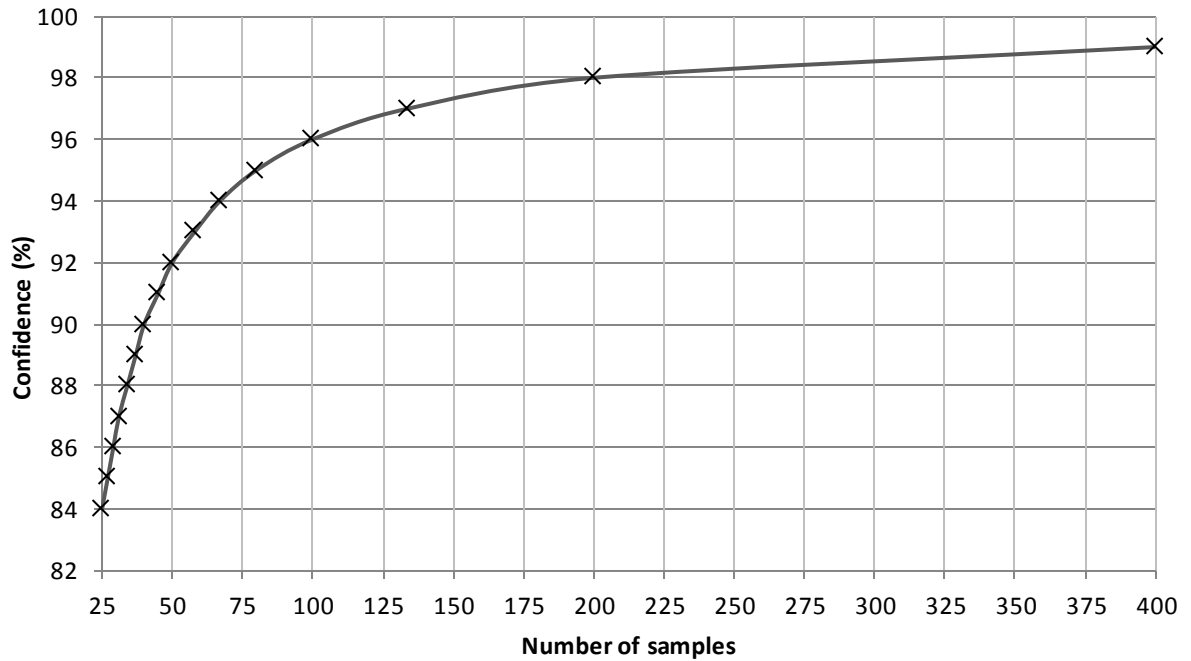
Ch. 3, Figure 2. Geomorphology suggestive of active hydrology. Inset (a) from a paleolake ringing Cassini basin (b) displays an inverted channel (a, white arrow; c, profile) preserved where Scammander Vallis (yellow arrow) once emptied into a basin encircling Cassini crater. Well-developed channels connecting to basins with subdued geomorphology point to transitions between subaerial and subaqueous processes. Red arrow shows the original valley before the nearby impact's debris apron filled the channel, causing the waters to pond (black arrow) before downcutting a new channel. Southeast of Cassini, Henry crater is one of several with central morphologies reminiscent of spring mounds or pingos. Both are features that occur where pressurized subsurface water deforms the surface material.

		None			Dust			Thickest
		1	2	3	4	5	6	7
Dark	1	2.046	1.034	0.770	0.170	0.044	0.015	0.010
	2	1.973	1.188	0.828	0.208	0.044	0.016	0.022
	3	1.754	1.702	1.061	0.247	0.044	0.017	0.009
	4	1.478	1.947	1.376	0.397	0.111	0.054	0.003
	5	1.030	1.598	1.451	0.927	0.613	0.454	0.280
	6	0.379	1.046	1.579	1.608	1.375	1.111	0.759
	7	0.205	0.753	1.313	1.881	1.673	1.504	1.313
Bright	8	0.106	0.460	1.062	2.035	1.755	1.826	2.216
	9	0.075	0.280	0.615	1.621	2.386	2.655	2.850
	10	0.107	0.407	0.612	1.594	2.630	2.709	1.871

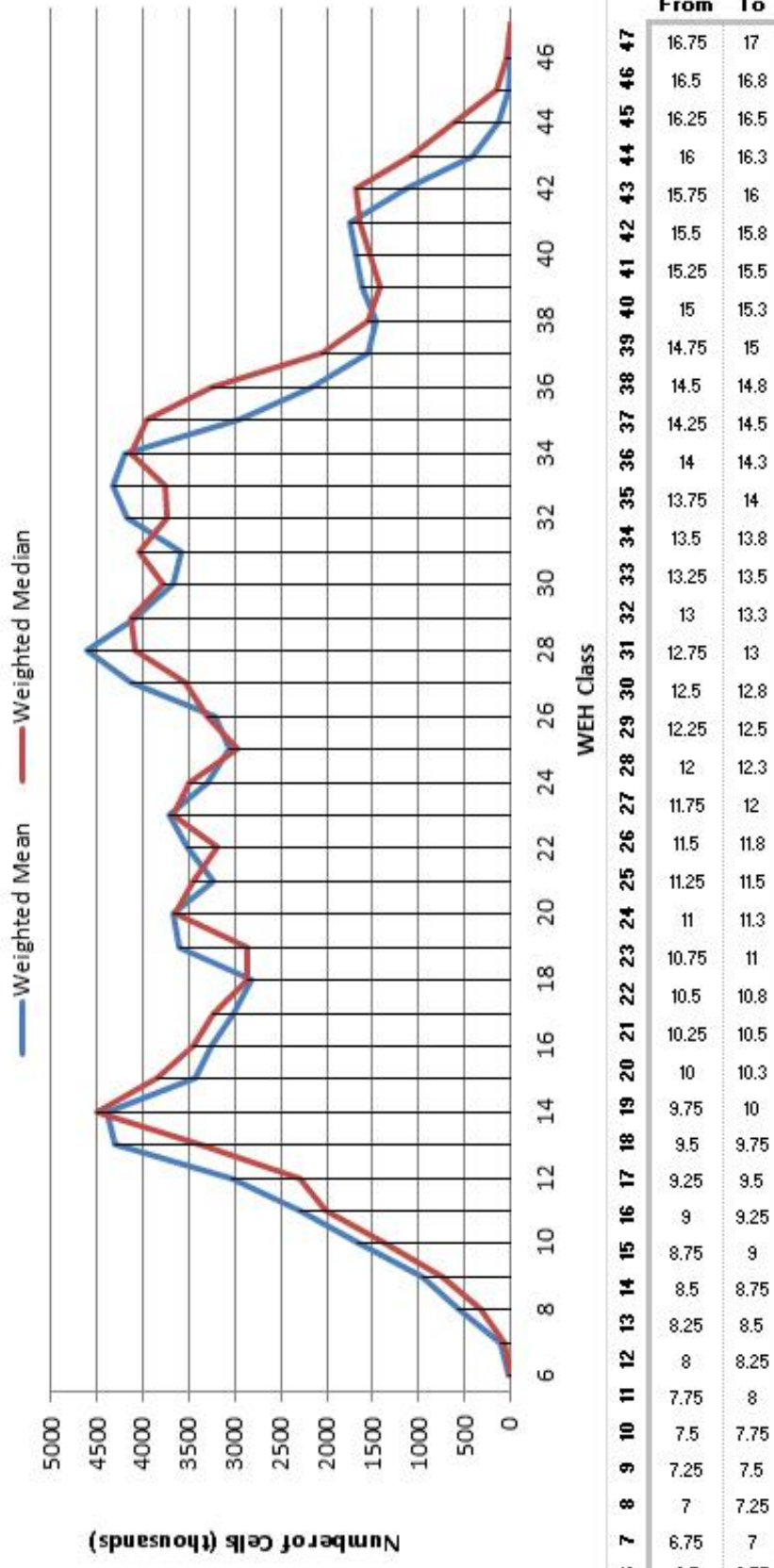
Ch. 3, Figure 3. Location quotient (LQ) matrix from dust and albedo class combinations. Using Eq. 1, values from Table A have been replaced with location quotients describing how common each combination of dust and albedo classes is in the mapping area. Values closest to one (light gray) are as abundant as expected. Higher values are remarkably frequent (dark gray), while lower values (white cells) are demonstrably rare.

		None			Dust			Thickest
		1	2	3	4	5	6	7
Dark	1	2.1	1.0	0.0	0.0	0.0	0.0	0.0
	2	2.2	1.0	1.0	0.0	0.0	0.0	0.0
	3	2.3	3.3	1.0	0.0	0.0	0.0	0.0
	4	2.4	3.4	4.4	0.0	0.0	0.0	0.0
	5	1.1	3.5	4.5	1.0	0.0	0.0	0.0
	6	0.1	1.1	4.6	5.6	6.6	1.0	0.0
	7	0.1	0.1	4.7	5.7	6.7	7.7	8.7
Bright	8	0.1	0.1	1.1	5.8	6.8	7.8	8.8
	9	0.1	0.1	0.1	5.9	6.9	7.9	8.9
	10	0.1	0.1	0.1	5.99	6.99	7.99	8.99

Ch. 3, Figure 4. LQ values grouped into LQ classes. Classification can be as simple (0, 1, 2 for rare, expected, frequent) or as complex as needed. Here the LQ values for rare combinations have been replaced with 0.0 for cells above the trend and 0.1 for those below. The expected values (1.0, 1.1) follow the same convention. The frequent value classification combines a whole number that changes with the dust class with a decimal value based on the albedo class. These classification groupings allow the spatial relationship between each combination or group of similar combinations to be singled out when the data is displayed on the map.



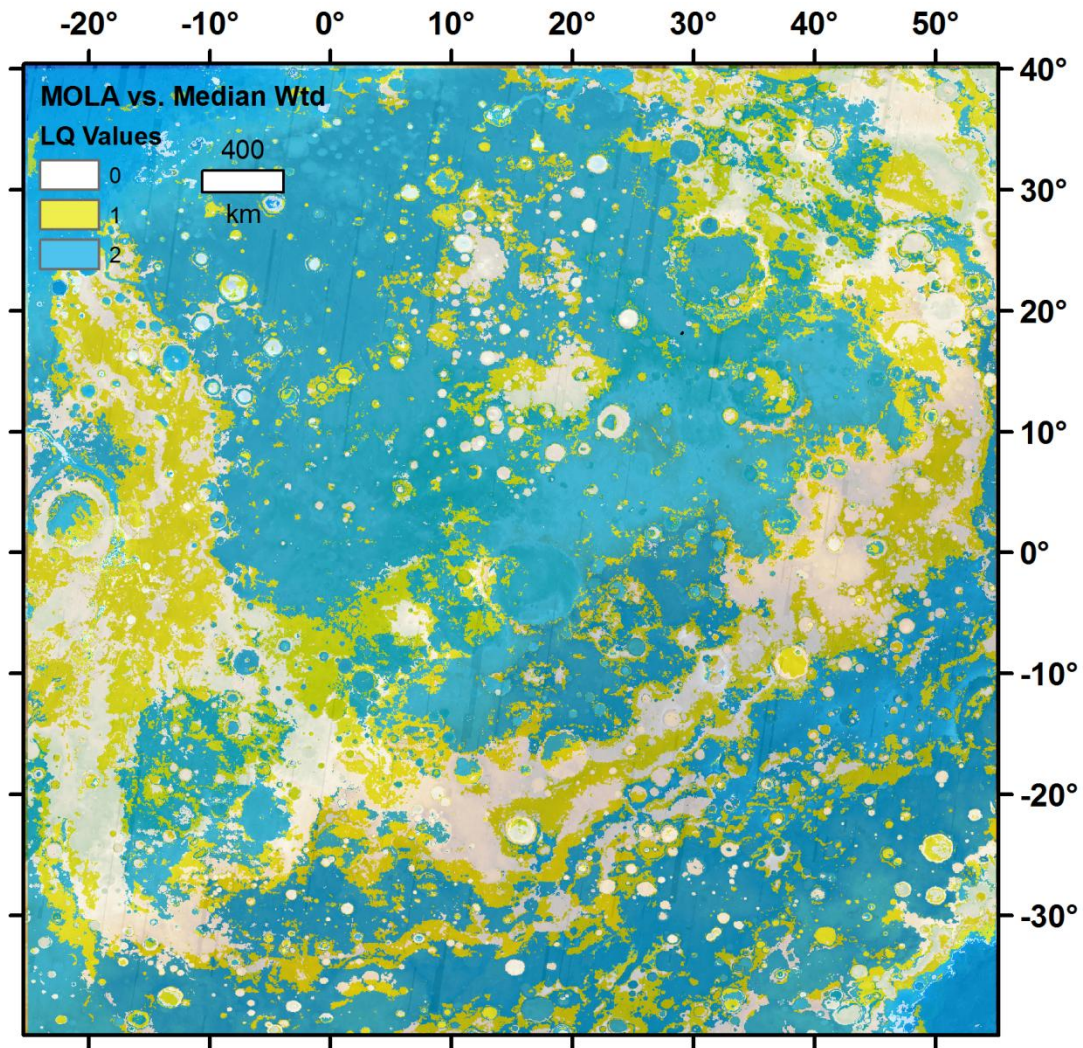
Ch. 3, Figure 5. Confidence levels with respect to sample size. Sampling windows of MONS data in the equatorial areas of Mars are known to follow a random Gaussian distribution (Maurice et al., 2011). Therefore, according to the Weak Law of Large Numbers (Bernoulli, 1713), as sample size increases, the likelihood increases that the mean of the sample approaches the mean of the entire population ( $\sim\infty$ ). A sample size of 400 results in 99% confidence that the sample mean is within half a standard deviation of the population mean.



Ch. 3, Figure 6. Comparison of WEH Class frequency between weighted mean and weighted median. The two measures of central tendency are only slightly offset from one another. Only from classes 27 to 35 (11.75 to 14 Wt.% water equivalent hydrogen) is there a change in the number of peaks, but differences are minor. The WEH wt.% class definitions are defined below the graph.

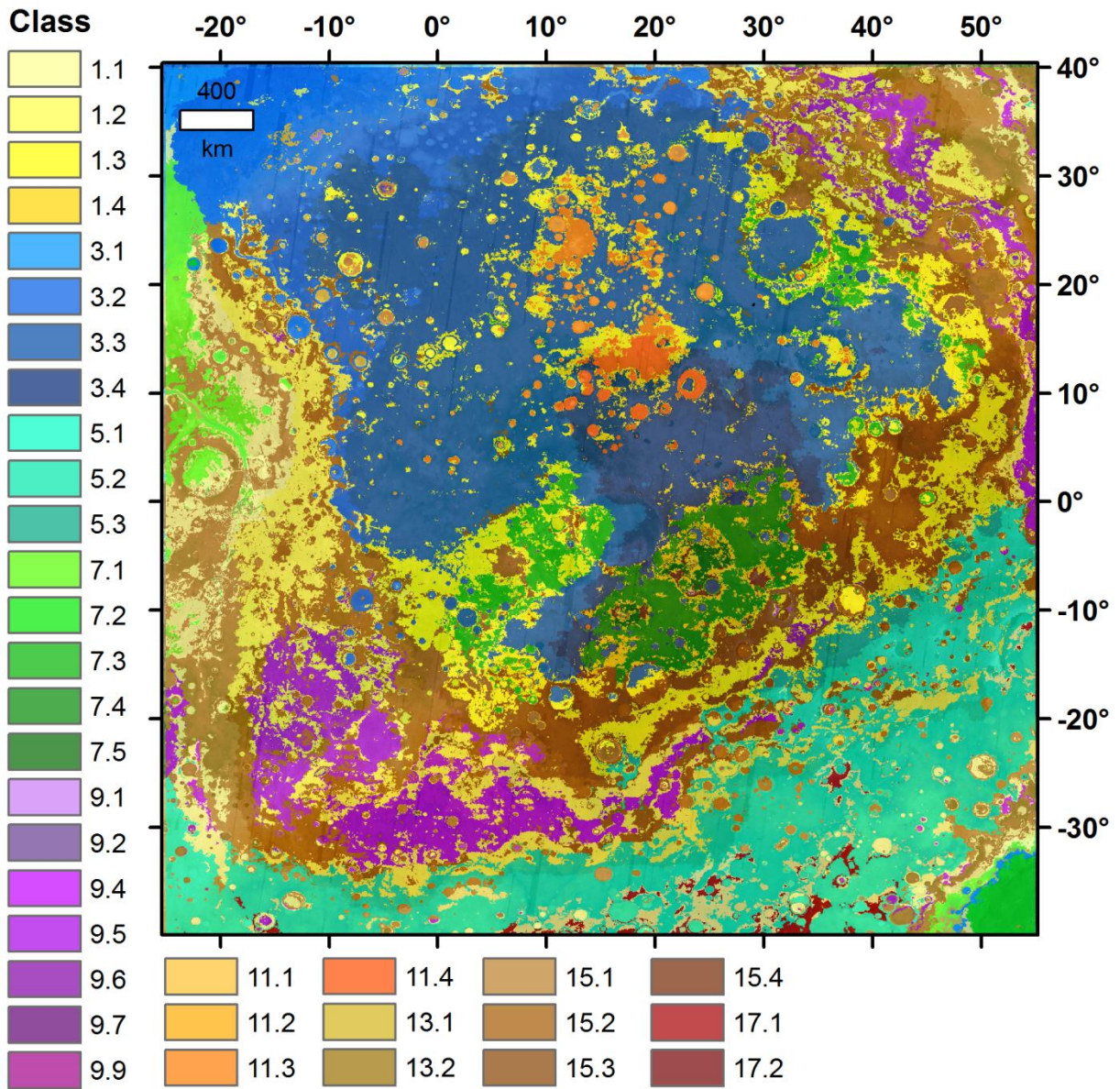






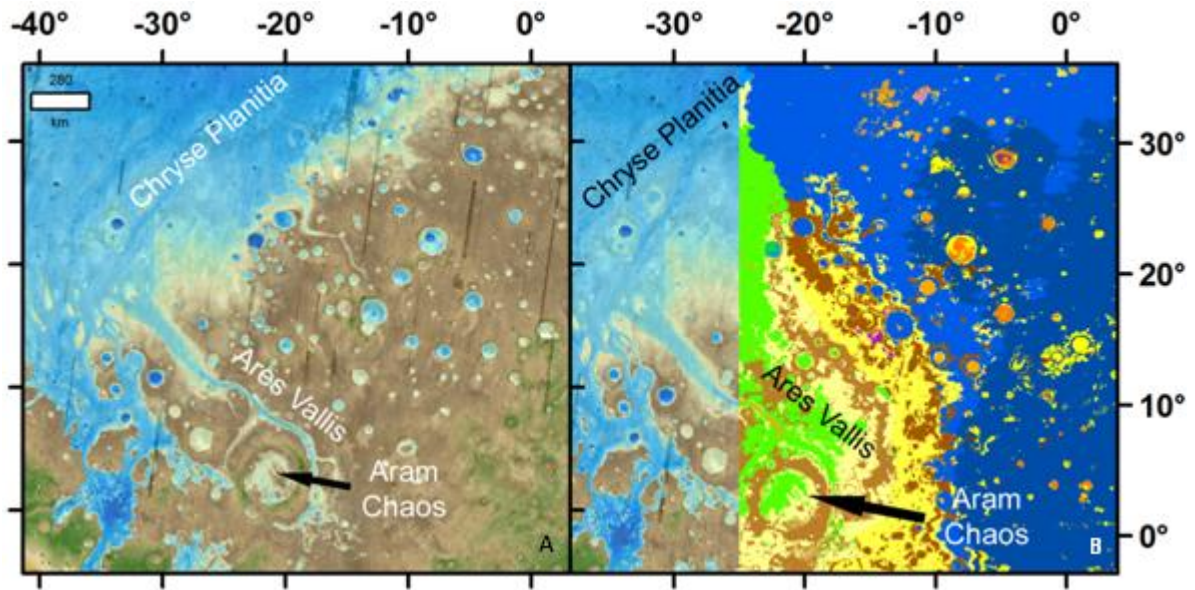
Ch. 3, Figure 9. LQ values for water equivalent hydrogen with elevation superimposed over the original basemap (Fig. 1). As in Fig. 7, blue indicates regions where the combination of WEH and elevation occurred more frequently than expected (Class 2). White areas are the locations of infrequent combinations (Class 0). Combinations that occurred as frequently as expected are shown in yellow (Class 1). Note that, aside from craters, features smaller than 2-3° may be spurious.

### MOLA vs Median Wtd

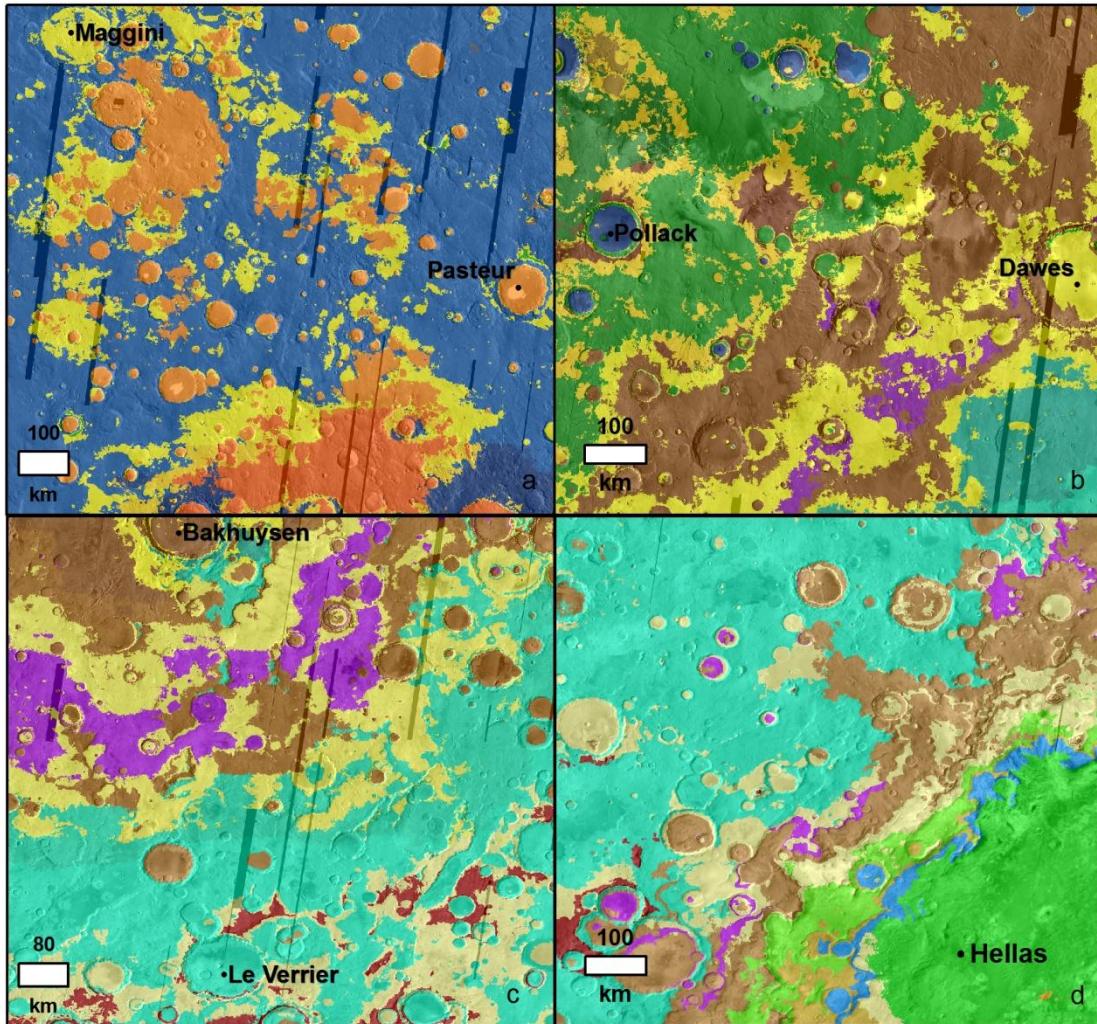


Ch. 3, Figure 10. LQ classes from Fig. 8 spatially projected onto the regional map. This symbology reveals the extent of each major trend (blue and cyan) as well as the direction of increasing hydrogen abundance. Green areas (7.1 through 7.5) depict high LQ combinations that do not display the positive trend between WEH and elevation. Note that class 7.1 (bright green, top left) indicates a negative association between WEH and elevation. Note that, aside from craters, features smaller than 2-3° may be spurious.

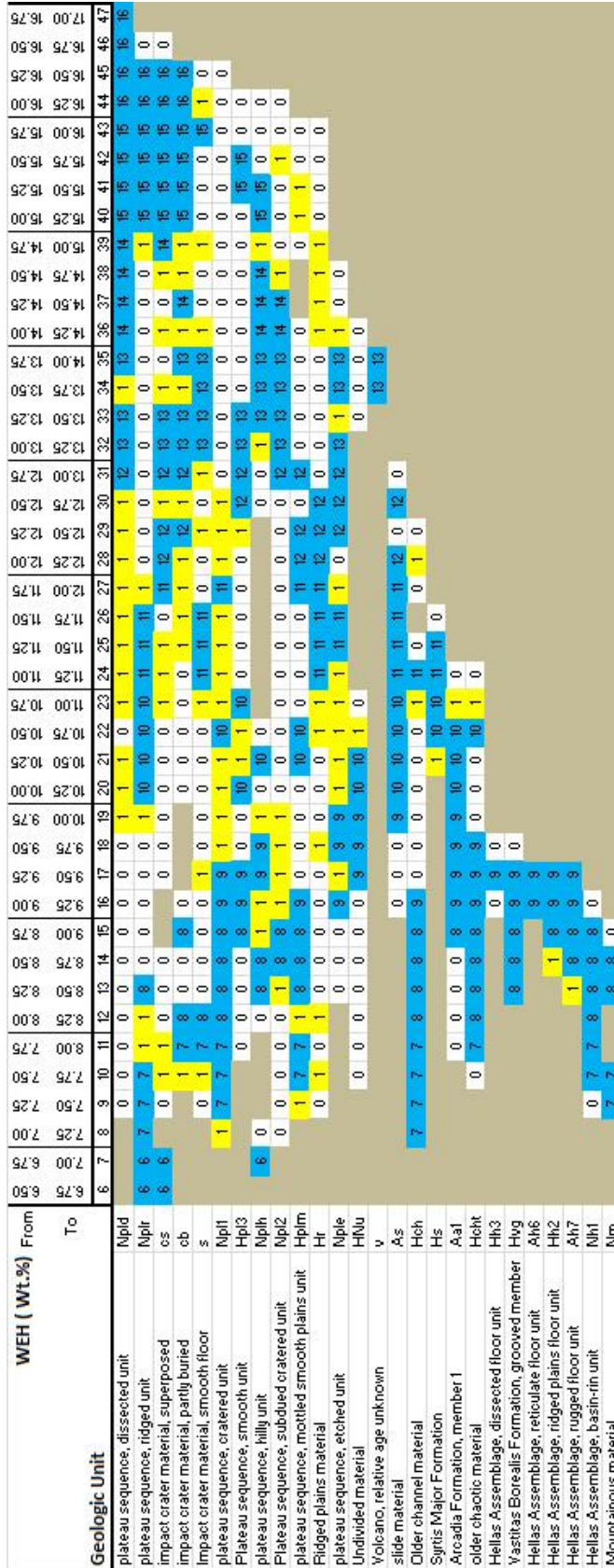




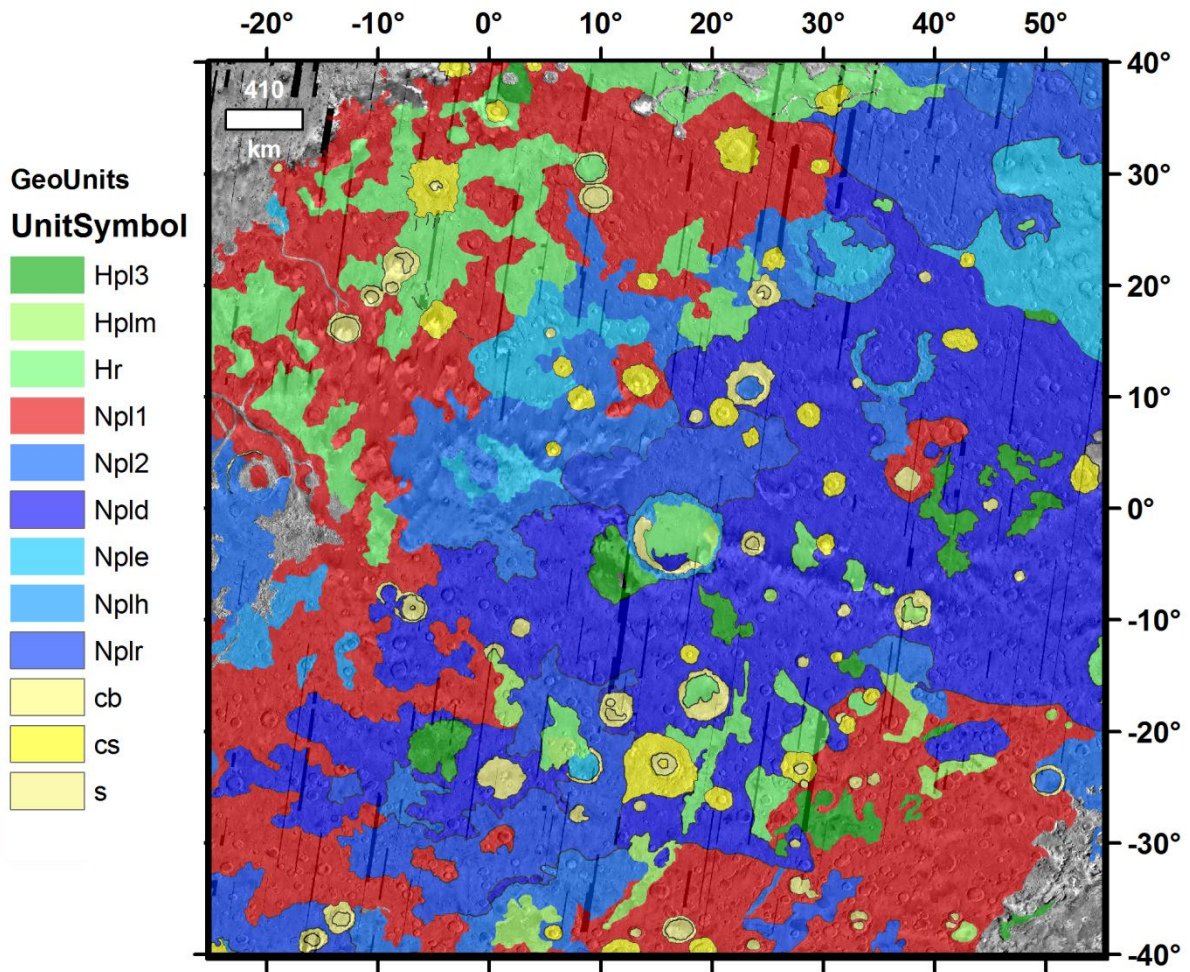
Ch. 3, Figure 11. Map of Ares Vallis region (A) with LQ class overlay (B). Green indicates class 7.1, a group of high LQ MOLA-WEH combinations with a negative trend. Here the higher elevations are highly eroded and contain lower hydrogen abundances than the lower elevations on the floor of Chryse Planitia. This is the only negatively associated cluster of high LQ values. Elevation legend, figure1; LQ class legend Fig. 11. Note that, aside from craters, features smaller than 2-3° may be spurious.





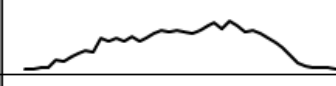

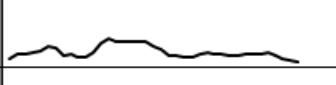



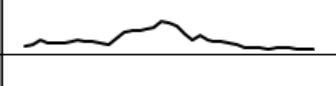

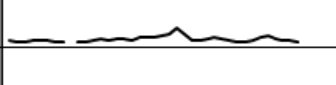

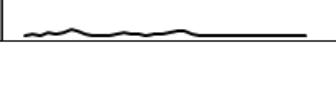
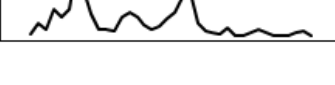
Ch. 3, Figure 12a-d. Four localities with lower than expected LQ combinations (see Fig. 1 for crater locations). The brown and orange areas correspond to classes 11-17 in Figs. 8 and 10. (a) Just south of Maggini lies the eroded remains of a  $>200$  km crater basin, whose interior has the same hydrogen abundance as the surrounding terrain, but the floor is  $>250$  m lower in elevation. (b) The highest WEH in the region (brown) lies between Pollack and Dawes craters. LQ class 15 tends to blanket highlands and crater rims. Also, directly north of Pollack, class 13.2 (golden tan) represents the highest WEH of all low LQ combinations. (c) The dark red around Le Verrier crater is found at elevations higher than the surrounding high LQ combinations representing the same WEH (cyan). (d) The darker brown (class 15.1) and golden tan (class 13.1) are higher in elevation than Hellas basin (green), but lower than the southeast slope of the topographic rise (cyan). Note that, aside from craters, features smaller than  $2-3^\circ$  may be spurious.



Ch. 3, Figure 13. The LQ matrix for WEH with geologic units manifests as a series of bars. The relationship between hydrogen abundance and specific units is clear as many units are only associated with specific WEH classes. Tan areas indicate no combinations for the two data sets, class 0 signifies low LQ, and class 1 are combinations that occur as frequently as expected. The high LQ cells classes (6-16) are numbered with the integer value of their WEH wt. % (i.e., 6 to 16 wt. % WEH) and are only associated with specific WEH classes.



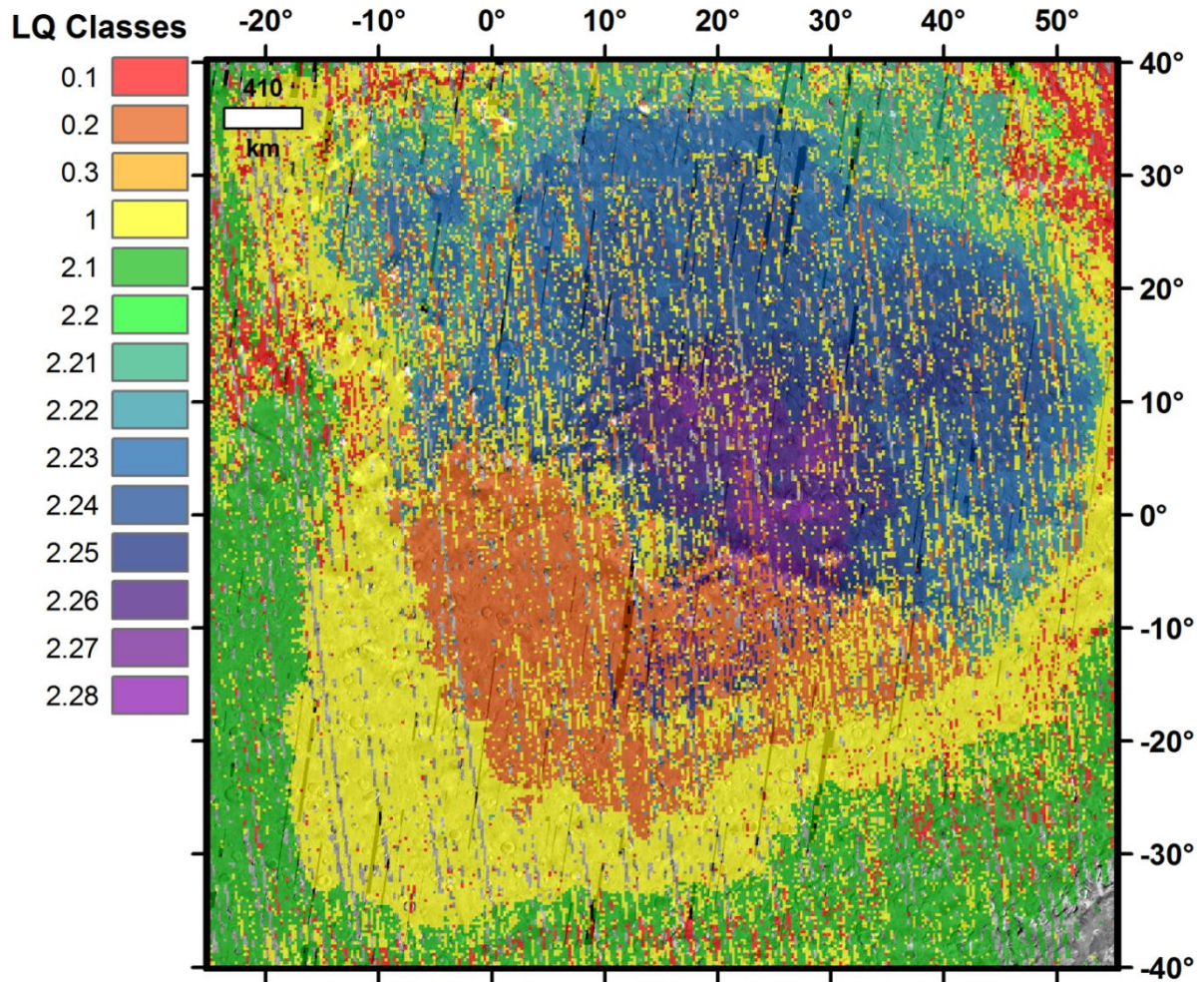
Ch. 3, Figure 14. Study area with selected geologic units from Skinner et al. (2006). The eight plateau deposits (plus Hr, the Hesperian ridged plains unit) and three impact crater units (yellow) nearly cover the map region. These are the only units with pixels in the >14.25 wt. % WEH range. Noachian plateau sequence Npl1 (described as the cratered unit) is the only plateau unit with a strong relationship to low WEH and infrequent high WEH pixels. All of its high LQ combinations occur below 12 wt.% WEH and all but two of these have <9.5 wt. % WEH. Geologic unit names on Fig. 13. Note that, aside from craters, features smaller than 2-3° may be spurious.

Unit	Relative Pixel Counts	Pixel Counts - Mode Emphasized	Total Pixels	Pixels > 12 Wt% WEH	Pixels > 14 Wt% WEH
Npl1			2.76E+07	5.14E+06	3.55E+05
Npld			2.70E+07	1.61E+07	7.07E+06
Nplr			1.03E+07	2.78E+06	1.35E+06
Npl2			9.93E+06	5.29E+06	1.01E+06
Hr			9.33E+06	2.84E+06	3.66E+05
cs			2.78E+06	1.47E+06	4.65E+05
Hplm			1.38E+06	3.67E+05	6.10E+04

Ch. 3, Figure 15. Top seven most frequent geologic units in the mapping area. Each histogram shows the number of pixels as WEH increases from 6.5 wt. % on the left to 17 wt. % on the right. The first column of histograms is normalized to Npl1. The second column of histograms is not normalized so that the mode(s) of each unit are emphasized. As pixel count is a way to quantify areal extent, Npl1 covers the largest percentage of the study area, but is only the sixth largest in respect to pixels with WEH values >14 wt. %. The top two rows, both Noachian plateau sequences, have nearly opposite WEH expression (Npl1 skewed to the lowest hydrogen abundances and Npld skewed to the highest values), while row 4 is bimodal. The break in unit cs, row 6, indicates that there are no pixels of that unit that correspond to that range of WEH values (8.75 – 9.25 wt. %).

From	To	Dust	6	7	8	9	10	11	12	13	14	15	16	17	18	19	20	21	22	23	24	25	26	27	28	29	30	31	32	33	34	35	36	37	38	39	40	41	42	43	44	45	46	47				
0	0.0225	1	2.1	2.1	2.1	2.1	2.1	2.1	2.1	2.1	2.1	2.1	2.1	2.1	2.1	1	1	1	1	1	1	1	1	0.2	0.2	0.2	0.2	0.2	0.2	0.2	0.2	0.2	0.2	0.2	0.2	0.2	0.2	0.2	0.2	0.2	0.2	0.2	0.2	0.2				
0.0225	0.2	2	1	1	2.1	2.1	1	1	1	1	1	1	1	1	1	1	1	1	1	1	1	1	1	1	1	0.2	0.2	0.2	0.2	0.2	0.2	0.2	0.2	0.2	0.2	0.2	0.2	0.2	0.2	0.2	0.2	0.2	0.2	0.2	0.2	0.2	0.2	
0.2	0.4	3	1	1	1	1	1	1	1	1	1	1	1	1	1	1	1	1	1	1	1	1	1	1	1	1	1	1	1	1	1	1	1	1	1	1	1	1	1	1	1	1	1	1	1	1	1	1
0.4	0.6	4	0.1	0.1	0.1	0.1	0.1	0.1	0.1	0.1	0.1	0.1	0.1	0.1	0.1	0.1	0.1	0.1	0.1	0.1	0.1	0.1	0.1	0.1	0.1	0.1	0.1	0.1	0.1	0.1	0.1	0.1	0.1	0.1	0.1	0.1	0.1	0.1	0.1	0.1	0.1	0.1	0.1	0.1	0.1	0.1	0.1	0.1
0.6	0.8	5	0.1	0.1	0.1	0.1	0.1	0.1	0.1	0.1	0.1	0.1	0.1	0.1	0.1	0.1	0.1	0.1	0.1	0.1	0.1	0.1	0.1	0.1	0.1	0.1	0.1	0.1	0.1	0.1	0.1	0.1	0.1	0.1	0.1	0.1	0.1	0.1	0.1	0.1	0.1	0.1	0.1	0.1	0.1	0.1	0.1	0.1
0.8	1	6	0.1	0.1	0.1	0.1	0.1	0.1	0.1	0.1	0.1	0.1	0.1	0.1	0.1	0.1	0.1	0.1	0.1	0.1	0.1	0.1	0.1	0.1	0.1	0.1	0.1	0.1	0.1	0.1	0.1	0.1	0.1	0.1	0.1	0.1	0.1	0.1	0.1	0.1	0.1	0.1	0.1	0.1	0.1	0.1	0.1	0.1
1	2.115	7	0.1	0.1	0.1	0.1	0.1	0.1	0.1	0.1	0.1	0.1	0.1	0.1	0.1	0.1	0.1	0.1	0.1	0.1	0.1	0.1	0.1	0.1	0.1	0.1	0.1	0.1	0.1	0.1	0.1	0.1	0.1	0.1	0.1	0.1	0.1	0.1	0.1	0.1	0.1	0.1	0.1	0.1	0.1	0.1	0.1	0.1

Ch. 3, Figure 16. LQ values converted to classes for Dust Cover Index (section 2.4.3) with WEHLQ. Colors indicate whether each combination of WEH and dust thickness occurred as frequently as expected (yellow), more frequently than expected (blue), or less frequently than expected (white). The matrix shows two clusters of high LQ values: the combination of little to no dust (DCI 1 and 2) with the lower WEH values (classes 6-17) grouped as class 2.1 and the negative trend between dust thickness and high hydrogen abundances (DCI 2-7 with WEH classes 19-47). LQ classes in this negative trend (increasing hydrogen abundance with decreasing dust cover) have been differentiated with decimal increments.

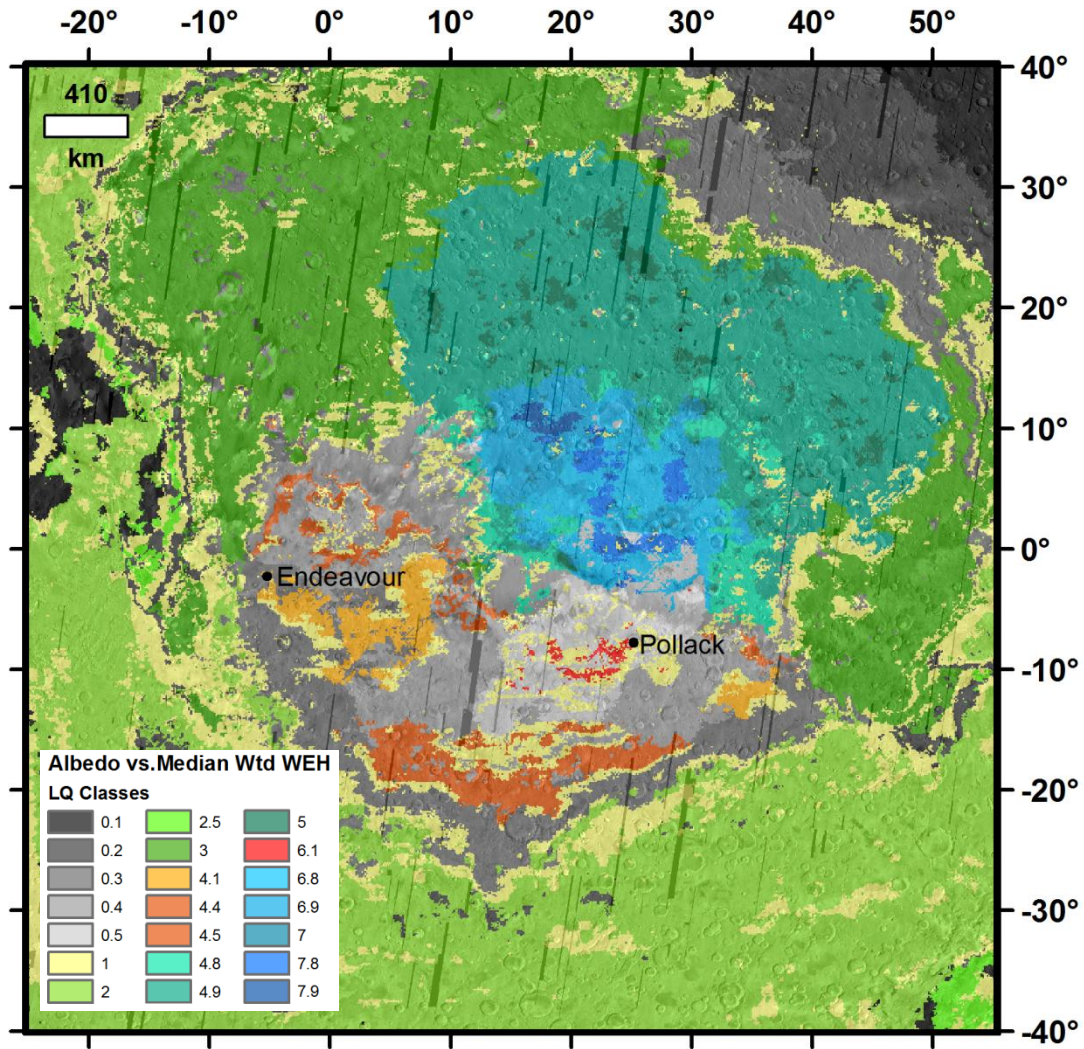


Ch. 3, Figure 17. Map of LQ classes from dust cover index and WEH combinations (Fig. 16). Class labels <1 represent lower than expected frequency combinations (red and oranges). Yellow indicates LQ values that are as expected for that combination. Green pixels highlight the location of the high LQ values where dust-free areas corresponded to low WEH values. Blue through violet pixels indicate increasing hydrogen content in the negative trend (Fig. 16). Note that, aside from craters, features smaller than 2-3° may be spurious.

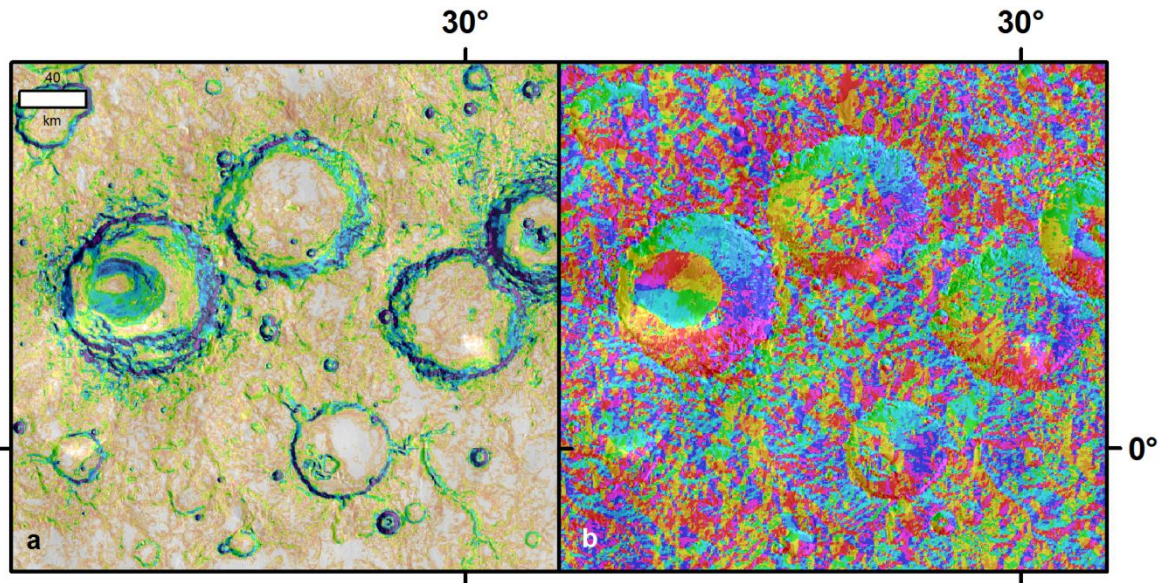
Albedo (Lambert Units)	6.50	7.00	7.25	7.50	7.75	8.00	8.25	8.50	8.75	9.00	9.25	9.50	9.75	10.00	10.25	10.50	10.75	11.00	11.25	11.50	11.75	12.00	12.25	12.50	12.75	13.00	13.25	13.50	14.00	14.25	14.50	14.75	15.00	15.25	15.50	15.75	16.00	16.25	16.50	16.75	17.00														
Dark to Light	6	7	8	9	10	11	12	13	14	15	16	17	18	19	20	21	22	23	24	25	26	27	28	29	30	31	32	33	34	35	36	37	38	39	40	41	42	43	44	45	46	47													
0.061 - 0.13	1	1.0	1.0	1.0	1.0	1.0	1.0	2.0	2.0	2.0	2.0	2.0	2.0	2.0	2.0	2.0	2.0	2.0	2.0	2.0	2.0	2.0	2.0	2.0	2.0	2.0	2.0	2.0	2.0	2.0	2.0	2.0	2.0	2.0	2.0	2.0	2.0	2.0	2.0	2.0	2.0	2.0	2.0	2.0	2.0	2.0	2.0	2.0							
0.13 - 0.15	2	0.1	1.0	1.0	2.0	2.0	1.0	2.0	2.0	2.0	2.0	2.0	2.0	2.0	2.0	2.0	2.0	2.0	2.0	2.0	2.0	2.0	2.0	2.0	2.0	2.0	2.0	2.0	2.0	2.0	2.0	2.0	2.0	2.0	2.0	2.0	2.0	2.0	2.0	2.0	2.0	2.0	2.0	2.0	2.0	2.0	2.0	2.0	2.0						
0.15 - 0.17	3	2.0	2.0	2.0	2.0	2.0	2.0	2.0	2.0	2.0	2.0	2.0	2.0	2.0	2.0	2.0	2.0	2.0	2.0	2.0	2.0	2.0	2.0	2.0	2.0	2.0	2.0	2.0	2.0	2.0	2.0	2.0	2.0	2.0	2.0	2.0	2.0	2.0	2.0	2.0	2.0	2.0	2.0	2.0	2.0	2.0	2.0	2.0	2.0	2.0	2.0				
0.17 - 0.19	4	0.1	0.1	2.0	2.0	2.0	2.0	2.0	2.0	1.0	0.2	0.2	0.2	0.2	0.2	0.2	0.2	1.0	1.0	0.3	0.3	0.3	0.3	0.3	0.3	0.3	0.3	0.3	0.3	0.3	0.3	0.3	0.3	0.3	0.3	0.3	0.3	0.3	0.3	0.3	0.3	0.3	0.3	0.3	0.3	0.3	0.3	0.3	0.3	0.3	0.3	0.3			
0.19 - 0.21	5	0.1	2.5	0.1	1.0	0.1	0.1	2.5	2.5	1.0	1.0	3.0	3.0	1.0	3.0	3.0	1.0	3.0	1.0	1.0	3.0	3.0	3.0	3.0	3.0	3.0	3.0	3.0	3.0	3.0	3.0	3.0	3.0	3.0	3.0	3.0	3.0	3.0	3.0	3.0	3.0	3.0	3.0	3.0	3.0	3.0	3.0	3.0	3.0	3.0	3.0	3.0			
0.21 - 0.23	6	0.1	1.0	0.1	0.1	0.1	0.1	0.1	0.1	1.0	2.5	1.0	0.2	1.0	3.0	3.0	1.0	3.0	3.0	3.0	3.0	3.0	3.0	3.0	3.0	3.0	3.0	3.0	3.0	3.0	3.0	3.0	3.0	3.0	3.0	3.0	3.0	3.0	3.0	3.0	3.0	3.0	3.0	3.0	3.0	3.0	3.0	3.0	3.0	3.0	3.0	3.0	3.0		
0.23 - 0.25	7	0.1	1.0	0.1	0.1	0.1	0.1	0.1	0.1	0.1	0.2	0.2	0.2	0.2	0.2	0.2	1.0	3.0	3.0	3.0	3.0	3.0	3.0	3.0	3.0	3.0	3.0	3.0	3.0	3.0	3.0	3.0	3.0	3.0	3.0	3.0	3.0	3.0	3.0	3.0	3.0	3.0	3.0	3.0	3.0	3.0	3.0	3.0	3.0	3.0	3.0	3.0	3.0	3.0	
0.25 - 0.27	8	0.1	0.1	0.1	0.1	0.1	0.1	0.1	0.1	0.1	0.2	0.2	0.2	0.2	0.2	0.2	1.0	1.0	1.0	1.0	1.0	1.0	1.0	1.0	1.0	1.0	1.0	1.0	1.0	1.0	1.0	1.0	1.0	1.0	1.0	1.0	1.0	1.0	1.0	1.0	1.0	1.0	1.0	1.0	1.0	1.0	1.0	1.0	1.0	1.0	1.0	1.0	1.0	1.0	1.0
0.27 - 0.29	9	0.1	0.1	0.1	0.1	0.1	0.1	0.1	0.1	0.1	0.2	0.2	0.2	0.2	0.2	0.2	0.2	0.2	0.2	0.2	0.2	0.2	0.2	0.2	0.2	0.2	0.2	0.2	0.2	0.2	0.2	0.2	0.2	0.2	0.2	0.2	0.2	0.2	0.2	0.2	0.2	0.2	0.2	0.2	0.2	0.2	0.2	0.2	0.2	0.2	0.2	0.2	0.2	0.2	
0.29 - 0.32	10	0.1	0.1	0.1	0.1	0.1	0.1	0.1	0.1	0.1	0.2	0.2	0.2	0.2	0.2	0.2	0.2	0.2	0.2	0.2	0.2	0.2	0.2	0.2	0.2	0.2	0.2	0.2	0.2	0.2	0.2	0.2	0.2	0.2	0.2	0.2	0.2	0.2	0.2	0.2	0.2	0.2	0.2	0.2	0.2	0.2	0.2	0.2	0.2	0.2	0.2	0.2	0.2	0.2	0.2

Ch. 3, Figure 18. LQ matrix for albedo with WEH. The negative trend of high LQ cells (blue) shows a strong association between dark albedo/low WEH (LQ class 2.0) and bright albedo and high hydrogen abundance. While the trend has some lower-than expected cells breaking up the trend in albedo class 4 (white, 0.19 - 0.21 Lambert, as described in 2.4.4), very few high WEH/low albedo combinations are above the main trend. As in previous matrices, yellow indicates combinations of WEH and albedo that are as frequent as expected. LQ classes are clustered, with the higher WEH classes having decimal classes signifying the albedo class (so that WEH class 32 has LQ classes 4.1, 4.4, 4.9, and 5.0 for albedo classes 1, 4, 9, and 10, respectively.)

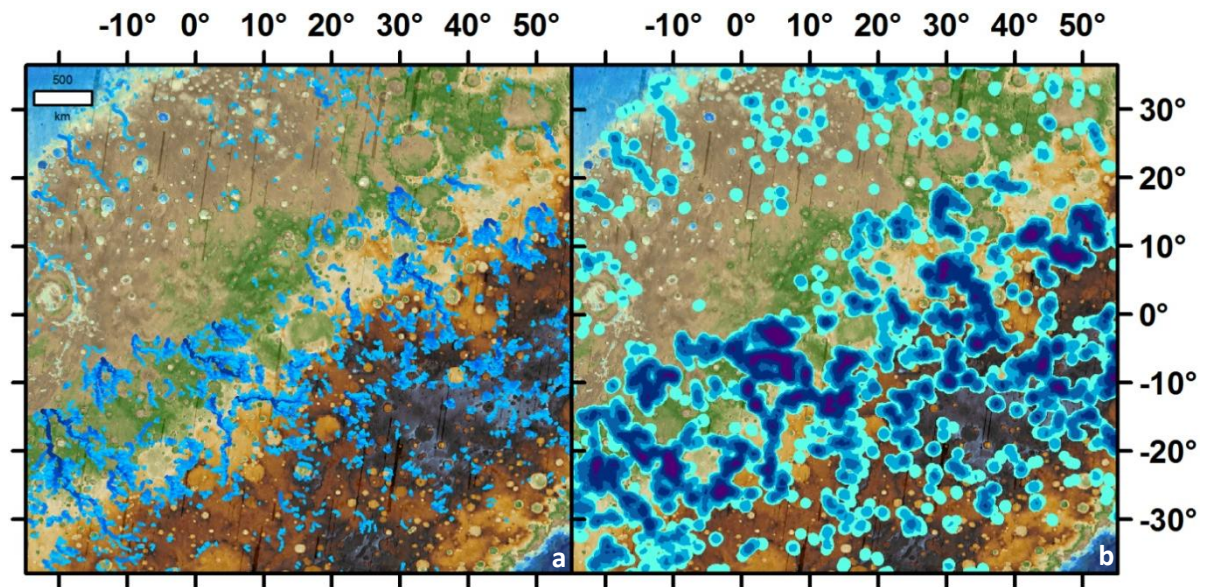




Ch. 3, Figure 19. Map of LQ classes from albedo and WEH matrix (Fig.18). As a rule, dark albedo areas are associated with low hydrogen abundances (classes 2-3). Exceptions to this include the orange areas (classes 4.1 – 4.5), which correspond to low albedo/moderate WEH regions, and the red area west of Pollack (class 6.1), the lone low albedo/high WEH locality. Note that, aside from craters, features smaller than 2-3° may be spurious.



Ch. 3, Figure 20. Slope (a) and aspect (b) data, both derivatives of elevation, provided general information for this study. While having the same 463 m/pixel spatial resolution as the other data sets, the variability of both slope and aspect make them better suited to kilometer-scale studies. These data sets were not combined with the MONS data.



Ch. 3, Figure 21. Basemap (Fig. 1) overlain by (a) valley network and (b) valley density layers. Dendritic valleys are widespread in the southern highlands (a) and end abruptly, with a low flat plain isolating them from the more linear channels along the northern edge of the study area. Darker blues indicate channels with multiple tributaries. Density layer (b) indicates areas with intensive dissection by valleys. Violet indicates the highest concentration of channels. See Fig. 1 for elevation legend.



MOLA Elevation			Valley Density					
From	To	Class	1	2	3	4	5	6
4601	3500	36	0.7	0.7	0.7	2.7	2.7	0.7
3500	3250	35	0.7	1.7	2.7	2.7	2.7	1.7
3250	3000	34	0.7	1.7	2.7	2.7	2.7	2.7
3000	2750	33	0.7	1.7	2.7	2.7	2.7	2.7
2750	2500	32	0.7	1.7	2.7	2.7	1.7	1.7
2500	2250	31	1.6	1.6	2.6	1.6	0.6	0.6
2250	2000	30	1.6	2.6	2.6	2.6	2.6	0.6
2000	1750	29	1.6	1.6	2.6	2.6	2.6	0.6
1750	1500	28	1.6	1.6	2.6	1.6	1.6	0.6
1500	1250	27	1.6	1.6	2.6	1.6	0.6	0.6
1250	1000	26	1.5	2.5	2.5	2.5	1.5	2.5
1000	750	25	1.5	1.5	1.5	2.5	2.5	2.5
750	500	24	0.4	1.4	1.4	2.4	2.4	2.4
500	250	23	0.4	1.4	2.4	2.4	2.4	2.4
250	0	22	0.4	1.4	2.4	2.4	2.4	2.4
0	-250	21	1.3	1.3	2.3	2.3	2.3	2.3
-250	-500	20	1.3	1.3	1.3	2.3	2.3	2.3
-500	-750	19	1.3	1.3	1.3	1.3	2.3	2.3
-750	-1000	18	1.3	1.3	1.3	1.3	2.3	2.3
-1000	-1250	17	1.2	1.2	1.2	2.2	2.2	0.2
-1250	-1500	16	1.2	0.2	0.2	1.2	1.2	0.2
-1500	-1750	15	2.1	1.1	0.1	0.1	0.1	0.1
-1750	-2000	14	2.1	1.1	0.1	0.1	0.1	0.1
-2000	-2250	13	2.1	1.1	0.1	0.1	0.1	0.1
-2250	-2500	12	1.1	1.1	1.1	0.1	0.1	0.1
-2500	-2750	11	1.1	1.1	1.1	0.1	0.1	
-2750	-3000	10	1.1	1.1	1.1	0.1	0.1	
-3000	-3250	9	1.1	1.1	1.1	0.1	0.1	
-3250	-3500	8	1.1	2.1	1.1	0.1		
-3500	-3750	7	2.1	1.1	0.1	0.1		
-3750	-4000	6	2.1	0.1	0.1	0.1		
-4000	-4250	5	2.1	0.1	0.1	0.1		
-4250	-4500	4	2.1	0.1	0.1			
-4500	-4750	3	2.1	0.1	0.1			
-4750	-5000	2	2.1	0.1	1.1			
-5000	-7687	1	2.1	0.1	0.1			

Ch. 3, Figure 24. The MOLA with valley density LQ matrix highlights areas where combinations of row and column are (blue) more frequent, (white) less frequent, or (yellow) as frequent as would be expected if all of the combinations were equally present in the region of interest. There is a strong (though non-linear) relationship between elevation and valley density. High density valley networks are frequently associated with elevations above -1200 m while lower elevations tend to have few or no valley channels within 250 m.

### Chapter 3 Tables

Ch. 3, Table A. Combinatorial Or output table for classes of albedo and dust. A Value term (assigned to each new combination of rasters by order of appearance during processing) is followed by the count of cells in that combination, and columns for each raster's classes. The first 25 of 70 possible combinations for these two classes are shown here.

VALUE	COUNT	Albedo Class	Dust Class
1	14681	2	1
2	4460	1	1
3	150	1	4
4	627	2	4
5	68	3	5
6	8714	3	1
7	1628	3	2
8	367	4	4
9	2771	2	3
10	1414	4	3
11	498	3	4
12	2372	3	3
13	1006	6	1
14	697	7	7
15	269	6	7
16	79	4	5
17	1101	5	1
18	402	5	4
19	698	5	3
20	204	5	5
21	1137	6	5
22	547	6	6
23	1886	6	3
24	1110	7	6
25	2352	7	3

Ch. 3, Table B. A frequency matrix organizes the counts by combination. Trends can be quickly identified: frequencies are lowest in the thick dust/dark albedo and no dust/bright albedo corners. Class values are defined in section 2.4.

Albedo	None			Dust		Thickest	
	1	2	3	4	5	6	7
Dark 1	4460	434	755	150	30	6	3
2	14681	1702	2771	627	102	22	22
3	8714	1628	2372	498	68	16	6
4	3375	856	1414	367	79	23	1
5	1101	329	698	402	204	90	40
6	1006	535	1886	1731	1137	547	269
7	814	577	2352	3035	2074	1110	697
8	329	276	1488	2568	1701	1054	920
9	506	364	1864	4427	5008	3317	2562
Bright 10	67	49	172	404	512	314	156

Ch. 3, Table C. LQ and LQ Classes appended to the original Combinatorial Or output table. Two columns are added to Table A, permitting the visualization of the spatial distribution of the data by combination, LQ value, or LQ Class (Figures 3 and 4) (the first 10 of 70 potential rows are shown here).

VALUE	COUNT	Albedo Class	Dust Class	LQ	LQ Class
1	14681	2	1	1.97	2.2
2	4460	1	1	2.05	2.1
3	150	1	4	0.17	0.0
4	627	2	4	0.21	0.0
5	68	3	5	0.04	0.0
6	8714	3	1	1.75	2.3
7	1628	3	2	1.70	3.3
8	367	4	4	0.40	0.0
9	2771	2	3	0.83	1.0
10	1414	4	3	1.38	4.4

### Chapter 3 References

- Andresen, M. A., 2007. Location quotients, ambient populations, and the spatial analysis of crime in Vancouver, Canada. *Environment and Planning A*, 39(10) 2423– 2444
- Bandfield, J. L., 2002. Global mineral distributions on Mars. *Journal of Geophysical Research: Planets*, (1991–2012), 107(E6), 9-1.
- Bernoulli, J. 1713. *Wahrscheinlichkeitsrechnung. Ars conjectandi*. Ostwalds Klassiker der exakten Wissenschaften, W. Engelmann, Leipzig, 1899.
- Bish, D. L., William Carey, J., Vaniman, D. T., Chipera, S. J., 2003. Stability of hydrous minerals on the martian surface. *Icarus*, 164, 96-103.
- Boynton, W. V., Feldman, W. C., Squyres, S. W., Prettyman, T. H., Brückner, J., and twenty others, 2002. Distribution of hydrogen in the near surface of Mars: evidence for subsurface ice deposits. *Science*, 297, 81-5.
- Bryson, K., Chevrier, V., Sears, D., Ulrich, R., 2008. Stability of ice on Mars and the water vapor diurnal cycle: Experimental study of the sublimation of ice through a fine-grained basaltic regolith. *Icarus*, 196, 446-458.
- Burr, D. M., Enga, M.-T., Williams, R. M. E., Zimbelman, J. R., Howard, A. D., Brennan, T. A., 2009. Pervasive aqueous paleoflow features in the Aeolis/Zephyria Plana region, Mars. *Icarus*, 200, 52-76.
- Cabrol, N. A., Grin, E. A., 2002. Overview on the formation of paleolakes and ponds on Mars. *Global and Planetary Change*, 35(3), 199-219.
- Chevrier, V., Ostrowski, D., Sears, D., 2008. Experimental study of the sublimation of ice through an unconsolidated clay layer: Implications for the stability of ice on Mars and the possible diurnal variations in atmospheric water. *Icarus*, 196, 459-476.
- Christensen, P. R., Ruff, S. W., 2004. Formation of the hematite-bearing unit in Meridiani Planum: Evidence for deposition in standing water. *Journal of Geophysical Research* 109, E08003. doi:10.1029/2003JE002233

- Christensen, P. R., Bandfield, J. L., Hamilton, V. E., Ruff, S. W., Kieffer, H. H., and twenty-one others, 2001a. Mars Global Surveyor Thermal Emission Spectrometer experiment: Investigation description and surface science results. *Journal of Geophysical Research*, 106, 23,823–23,872. doi:10.1029/2000JE001370
- Christensen, P. R., Morris, R. V., Lane, M. D., Bandfield, J. L., Malin, M. C., 2001b. Global mapping of Martian hematite mineral deposits: Remnants of water-driven processes on early Mars. *Journal of Geophysical Research*, 106, 23,873–23,886. doi:10.1029/2000JE001415
- Fastook, J. L., Head, J. W., Marchant, D. R., Forget, F. 2008. Tropical mountain glaciers on Mars: Altitude-dependence of ice accumulation, accumulation conditions, formation times, glacier dynamic, and implication for planetary spin-axis/orbital history. *Icarus*, 198, 305-317.
- Feldman, W. C., Boynton, W. V., Tokar, R. L., Prettyman, T. H., Gasnault, O., and eight others, 2002. Global distribution of neutrons from Mars: Results from Mars Odyssey. *Science*, 297.5578, 75-78. doi: 10.1126/science.1073541
- Feldman, W. C., Prettyman, T. H., Maurice, S., Plaut, J. J., Bish, D. L., and ten others, 2004a. Global distribution of near-surface hydrogen on Mars. *Journal of Geophysical Research*, 109.E9, E09006. doi: 10.1029/2003JE002160.
- Feldman, W. C., Head, J. W., Maurice, S., Prettyman, T. H., Elphic, R. C., and four others, 2004b. Recharge mechanism of near-equatorial hydrogen on Mars: Atmospheric redistribution or sub-surface aquifer. *Geophysical Research Letters*, 31(18).
- Feldman, W. C., Prettyman, T. H., Maurice, S., Nelli, S., Elphic, R., and six others, 2005. Topographic control of hydrogen deposits at low latitudes to midlatitudes of Mars. *Journal of Geophysical Research: Planets*, 110, E11009, doi:10.1029/2005JE002452.
- Gibson C., 2003. Digital divides in New South Wales: a research note on socio-spatial inequality using 2001 Census data on computer and Internet technology. *Australian Geographer* 34(2) 239-257. DOI: 10.1080/00049180301734.
- Harrison, K. P., 2005. Groundwater-controlled valley networks and the decline of surface runoff on early Mars. *Journal of Geophysical Research*, 110.



- Head, J. W., Neukum, G., Jaumann, R., Hiesinger, H., Hauber, E., and nine others, 2005. Tropical to mid-latitude snow and ice accumulation, flow and glaciation on Mars. *Nature*, 434: 346-350.
- Hynek, B. M., Hoke, M. R. T., Beach, M., 2010. Updated Global Map of Martian Valley Networks and Implications for Climate and Hydrologic Processes. *Journal of Geophysical Research*, 115, E09008, doi:10.1029/2009JE003548.
- Jakosky, B., Mellon, M., Varnes, E., Feldman, W., Boynton, W., Haberle, R., 2005. Mars low-latitude neutron distribution: Possible remnant near-surface water ice and a mechanism for its recent emplacement. *Icarus*, 175, 58-67.
- Jones, J., Cameron, B., 1987. Surface distribution of Foraminifera in a New England salt marsh: Plum Island, Massachusetts. *Atlantic Geology* [Online], 23.3, Web. 9 May, 2012.
- Knauth, L. P., Burt, D. M., Wohletz, K. H., 2005. Impact origin of sediments at the Opportunity landing site on Mars. *Nature*, 438, 1123-8.
- McLaughlin, C. J., Smith, C. A., Buddemeier, R. W., Bartley, J. D., Maxwell, B. A., 2003. Rivers, runoff, and reefs. *Global and Planetary Change*, 39(1), 191-199.
- Michalski, J. R., Cuadros, J., Niles, P. B., Parnell, J., Deanne Rogers, A., Wright, S. P., 2013. Groundwater activity on Mars and implications for a deep biosphere. *Nature Geoscience*, 6, 133-138.
- Mitrofanov, I., Anfimov, D., Kozyrev, A., Litvak, M., Sanin, A., and seven others, 2002. Maps of subsurface hydrogen from the high energy neutron detector, Mars Odyssey. *Science*, 297, 78-81.
- Mustard, J. F., Murchie, S. L., Pelkey, S. M., Ehlmann, B. L., Milliken, R. E., and thirty-one others, 2008. Hydrated silicate minerals on Mars observed by the Mars Reconnaissance Orbiter CRISM instrument. *Nature*, 454, 305-9.
- Phillips, R. L., Kinman, E. L., Schnitzer, P. G., Lindbloom, E. J., Ewigman, B., 2000. Using geographic information systems to understand health care access. *Archives of Family Medicine*, 9(10), 971-978.
- Poulet, F., Bibring, J. P., Mustard, J. R., Gendrin, A., Mngold, M., and four others, 2005. Phyllosilicates on Mars and implications for early martian climate. *Nature*, 438, 623-7.

- Prettyman, T. H., 2004. Composition and structure of the Martian surface at high southern latitudes from neutronspectroscopy. *Journal of Geophysical Research*, 109.
- Prettyman, T. H., 2006. Remote Chemical Sensing Using Nuclear Spectroscopy. *Encyclopedia of the Solar System*, ed. T. Spohn, et al. San Diego: Academic Press, 775-86
- Putzig, N., Mellon, M., 2007. Apparent thermal inertia and the surface heterogeneity of Mars. *Icarus*, 191, 68-94.
- Rodríguez, J. A. P., Tanaka, K. L., Kargel, J. S., Dohm, J. M., Kuzmin, R., and five others, 2007. Formation and disruption of aquifers in southwestern Chryse Planitia, Mars. *Icarus*, 191, 545-567.
- Rossi, A. P., Neukum, G., Pondrelli, M., Van Gasselt, S., Xegers, T., and three others, 2008. Large-scale spring deposits on Mars? *Journal of Geophysical Research*, 113.
- Ruff, S. W., Christensen, P. R., 2002. Bright and dark regions on Mars: Particle size and mineralogical characteristics based on Thermal Emission Spectrometer data. *Journal of Geophysical Research: Planets*, (1991–2012), 107(E12), 2-1.
- Sakimoto, S. E. H., 2005. Central mounds in Martian impact craters: assessment as possible perennial permafrost mounds (pingos). *Lunar and Planetary Science Conference 36*, 2099.
- Seneta, Eugene. 2013. A Tricentenary history of the Law of Large Numbers. *Bernoulli* 19, no. 4, 1088--1121. doi:10.3150/12-BEJSP12. <http://projecteuclid.org/euclid.bj/1377612845>.
- Skinner, J.A., Jr., T.M. Hare, K.L. Tanaka, 2006. Digital Renovation of the Atlas of Mars 1:15,000,000-Scale Global Geologic Series Maps. *Lunar and Planetary Science Conference 37*, 2331.
- Smith, D. E., Zuber, M.T., Frey, H.V., Garvin, J.B., Head, J.W., and nine teen others, 2001. Mars Orbiter Laser Altimeter: Experiment summary after the first year of global mapping of Mars. *Journal of Geophysical Research*, 106, 23,689–23,722, doi:10.1029/2000JE001364.
- Soare, R. J., Osinski, G. R., Costard, F., 2008. Recent, late Amazonian pingos, ice-rich landscapes and periglacial ponding in Utopia and western Elysium Planitia, Mars. *Lunar and Planetary Science Conference 39*, 1315.

- Squyres, S.W., Knoll, A. H., Arvidson, R. E., Clark, B. C., Grotzinger, J. P., and thirteen others, 2006. Two years at Meridiani Planum: Results from the Opportunity Rover. *Science*, Vol 313, no. 5792, 1403-1407. doi: 10.1126/science.1130890
- Whiteway, J. A., Komguem, L., Dickinson, C., Cook, C., Illnicki, M., and nineteen others, 2009. Mars Water-Ice Clouds and Precipitation. *Science*, 325 (5936), 68-70. [DOI:10.1126/science.1172344]
- Wang, A., Haskin, L. A., Squyres, S. W., Joliff, B. L., Crumpler, L., and eight others, 2006. Sulfate deposition in subsurface regolith in Gusev crater, Mars. *Journal of Geophysical Research*, 111.
- Wu, H., Skripov, A. V., Udovic, T. J., Rush, J. J., Derakhshan, S., Kleinke, H., 2010. Hydrogen in Ti<sub>3</sub>Sb and Ti<sub>2</sub>Sb: Neutron vibrational spectroscopy and neutron diffraction studies. *Journal of Alloys and Compounds*, 496, 1-6.
- Zuber, M.T., Smith, D.E., Solomon, S.C., Muhleman, D.O., Head, J.W., and three others, 1992. The Mars Observer Laser Altimeter investigation. *Journal of Geophysical Research*, 97, 7781-7798.